THESIS FOR THE DEGREE OF DOCTOR OF PHILOSOPHY

Relaxation and Resonance in Brownian Motion-Coupled Resonators

CHRISTIN RHÉN

Department of Physics
CHALMERS UNIVERSITY OF TECHNOLOGY
Göteborg, Sweden 2017

Relaxation and Resonance in Brownian Motion-Coupled Resonators

CHRISTIN RHÉN

ISBN 978–91–7597–592–4
© CHRISTIN RHÉN, 2017.

Doktorsavhandlingar vid Chalmers tekniska högskola
Ny serie nr 4273
ISSN 0346–718X

Department of Physics
Chalmers University of Technology
SE-412 96 Göteborg, Sweden
Telephone +46 (0)31–7721000

Typeset in LaTeX. Figures created using Matlab and Corel Painter Essentials.

Chalmers reproservice
Göteborg, Sweden 2017

Relaxation and Resonance in Brownian Motion-Coupled Resonators

CHRISTIN RHÉN
Department of Physics
Chalmers University of Technology

ABSTRACT

In physics, there exists a number of paradigm systems – exactly solvable models that can represent a wide variety of physical realizations. My research is concerned with two of these paradigm systems: the harmonic oscillator and Brownian motion. In this thesis, I investigate the dynamics of coupled oscillator-diffusion systems, in different contexts.

A general Hamiltonian model illustrates the rich dynamics of a particle-like degree of freedom coupled to two degenerate oscillators. The interplay of the three creates unpredictable particle behaviour, switching between trapped, regular oscillations, and untrapped, possibly chaotic motion. The trapping-retrapping dynamics of the particle corresponds to switching between high and low dissipation of oscillator energy, resulting in an unusual, stepwise relaxation.

Motivated by the rapid strides made in recent years in the field of nanomechanical sensing, in particular mass sensing, I consider particles loosely adsorbed on a one- or twodimensional carbon nanomechanical resonator. The particles are allowed to diffuse across the surface of the resonator, and fluctuations in their positions induce dissipation of vibrational resonator energy. I show that depending on vibration amplitude, the motion of the resonator-particle system separates into different regimes. In each I describe the particle motion and characterize the resonator relaxation towards equilibrium.

An immediately experimentally attainable diffusion-resonator system is a superconducting LC-resonator inductively coupled to a superconducting quantum interference device (SQUID). The superconducting phase of the SQUID takes the role of a Brownian variable. I find that the resonant response of the circuit is multistable, an effect that becomes more pronounced the weaker the noise is; the severity of the circuit's nonlinearity can be tuned by the level of noise in the system.

With superconducting circuit quantum electrodynamics being routinely done in the lab, experimental verification of my results concerning the LC-resonator coupled to a SQUID should be possible. For the nanomechanical particle-resonator system, experimental interest in room-temperature applications, and in adsorbate-induced anomalous dynamics is growing. My work in this area functions as a record of possible diffusion-induced ringdown effects.

KEYWORDS: nonequilibrium dynamics, nonlinear dynamics, noise, relaxation, resonance, Brownian motion, resonator, dispersive coupling, nanomechanics, superconducting circuits.

Relaxering och resonans i Brownsk rörelse-kopplade resonatorer

CHRISTIN RHÉN
Institutionen för fysik
Chalmers tekniska högskola

SAMMANFATTNING

I fysiken finns ett antal paradigmsystem - modeller som är exakt lösbara och som kan representera ett stort antal fysiska system. Min forskning handlar om två av dessa paradigmsystem: den harmoniska oscillatorn och Brownsk rörelse. I denna avhandling undersöker jag, i olika sammanhang, dynamiken i system där oscillatorer kopplas till diffuserande variabler.

En allmän Hamiltoniansk modell illustrerar den komplexa dynamik som uppstår i ett system bestående av en partikellik frihetsgrad kopplad till två degenererade oscillatorer. Samspelet mellan dessa tre resulterar i ett oförutsägbart partikelbeteende, som skiftar mellan regelbundna oscillationer nära ett potentialminimum och oregelbunden, möjligtvis kaotisk, rörelse över hela partikelns domän. Växlingen mellan fångad och fri partikelrörelse orsakar växlingar mellan hög och låg dissipation av oscillatorenergi; den totala oscillatorenergin relaxerar på ett ovanligt, trappstegsliknande sätt.

Känsligheten i nanomekaniska sensorer, speciellt massensorer, har utvecklats dramatiskt sedan sekelskiftet. Motiverad av dessa framsteg studerar jag partiklar löst adsorberade på en nanomekanisk resonator gjord av kolnanorör eller grafen. Partiklarna kan diffusera över resonatorns yta, och fluktuationer i partikelpositionerna orsakar dissipation av resonatorns vibrationsenergi. Jag visar att resonator-partikelsystemet beter sig på två olika sätt beroende på om vibrationsamplituden är hög eller låg. I båda dessa regimer beskriver jag partikelrörelsen och systemets relaxering mot termisk jämvikt.

Ett resonator-diffusionssystem som redan idag kan konstrueras i laboratorium är en supraledande LC-resonator induktivt kopplad till en supraledande kvantinterferensenhet (SQUID). SQUIDens supraledande fas beter sig här som en Brownsk variabel. När denna krets drivs nära resonans blir den multistabil, och ju lägre brusnivån är, desto skarpare blir denna effect. Hur stark kretsens ickelinjäritet är kan alltså justeras genom att ändra systemets brusnivå.

Experiment inom supraledande kvantelektrodynamik görs idag rutinmässigt, så mina resultat i LC-kretsen kopplad till en SQUID bör vara rättframma att verifiera. Gällande det nanomekaniska systemet finns ett växande intresse att utföra experiment i rumstemperatur, och av att studera ovanlig resonatordynamik orsakad av adsorbat. Här fungerar mitt arbete som ett referensverk över möjliga diffusionsinducerade effekter.

NYCKELORD: ickejämviktsdynamik, ickelinjär dynamik, brus, relaxering, resonans, Brownsk rörelse, resonator, dispersiv koppling, nanomekanik, supraledande kretsar.

LIST OF PUBLICATIONS

This thesis consists of an introductory text and the following papers:

I **Diffusion-induced dissipation and mode coupling in nanomechanical resonators**
Christin Edblom and Andreas Isacsson
Physical Review B **90**, 155425 (2014)

II **Particle number scaling for diffusion-induced dissipation in graphene and carbon nanotube nanomechanical resonators**
Christin Rhén and Andreas Isacsson
Physical Review B **93**, 125414 (2016)

III **Noise-tunable nonlinearity in a dispersively coupled diffusion-resonator system using superconducting circuits**
Christin Rhén and Andreas Isacsson
Scientific Reports **7**, 41313 (2017)

IV **Stepwise relaxation and stochastic precession in degenerate oscillators dispersively coupled to particles**
Christin Rhén and Andreas Isacsson
arXiv:1706.02992 (2017)
Submitted to Physical Review B

Specification of my contribution to the publications:

I I performed all the numerical calculations, and contributed to the analytical calculations as well as in writing the paper.

II I came up with the idea for the study and did the majority of the numerical calculations. I contributed to the analytical calculations and in writing the paper.

III I suggested considering alternative diffusion-resonator systems, though not the superconducting one that was ultimately studied. I performed all the numerical calculations, and contributed to the analytical calculations and in writing the paper.

IV I performed the majority of the numerical calculations, and contributed to writing the paper.

Contents

List of figures

1 Introduction

In this thesis, I describe my work on systems consisting of a linear resonator coupled to a Brownian degree of freedom. It is well known that an otherwise linear oscillator can attain novel and nonlinear features through interaction with another dynamical system. By choosing this auxiliary system to be Brownian, my work connects two of the most broadly used paradigm systems of physics. Accordingly, the novel dynamics described in this work could appear in a wide range of applications. Perhaps the first such will be in the field of nanomechanics, where the interest in studying nanomechanical resonators outside of cryogenic conditions is rapidly growing.

My research was originally motivated by the desire to develop new nanomechanical mass sensors that would function also at room temperature. Then, thermal noise would be unavoidable, and the measured mass would no longer be stationary but instead diffuse across the resonator. In papers I and II, I show that diffusing particles loosely adsorbed on the surface of carbon nanotube and graphene resonators induce a coupling between the resonator vibrational modes, as well as introduce new channels of dissipation. The time dependence of this diffusion-induced dissipation changes depending on the behaviour of the particles, but it is never an exponential decay. Graphene resonators are further investigated in paper IV, where the effect of degenerate membrane modes on the induced mode coupling and the atypical ringdown is studied. The most important lesson from these papers is that even if a resonator used in a device is perfectly linear, if adsorbed particles are present, the resonator ringdown dynamics will be quite complicated. While the significance in mass sensing systems is clear, my work can also become relevant if resonator-based devices are used in ambient conditions, exposed to air molecules and thermal fluctuations.

Nanomechanical resonators are versatile systems with rich dynamics, but the state of the art of their fabrication is not quite capable of creating devices where the diffusion of adsorbates on a resonator is high and resonator sizes and frequencies are controlled to the degree required to experimentally reproduce the results of papers I and II. However, the large variety of physical realizations of resonators and Brownian systems allows for the construction of analogous systems. In paper III,

I consider one such analogous system. Here, a superconducting LC-resonator is coupled to a Brownian degree of freedom realized as the superconducting phase of a superconducting quantum interference device. This analogous circuit is capable of recreating the anomalous ringdown of the nanomechanical resonator-particle system, and its driven response is highly interesting in its own right. The level of noise can tune the resonator frequency shift from linear to highly nonlinear and back, resulting in a complex, multistable frequency response curve. The proposed system should be straight-forward to realize in the lab.

Finally, in paper IV, a very general Hamiltonian description of multimode resonators dispersively coupled to Brownian degrees of freedom is developed, that can be adapted to fit a range of resonators, Brownian systems, and couplings between the two. I consider a version of the Hamiltonian model with a minimal set of degrees of freedom. Even in this simplified case, the oscillator energy relaxes in an anomalous, stepwise manner; the behaviour of both the oscillator modes and the Brownian particle is studied in depth.

1.1 Thesis overview

My research concerns nonlinear systems that are far from thermal equilibrium and subject to noise. Accordingly, I build upon several rather disparate areas of physics and mathematics. The following four chapters of this thesis, where the necessary background and theoretical tools are explained, can thus seem somewhat detached from one another. However, in the penultimate chapter 6, I summarize my own research; I hope that all the threads will there be neatly tied together.

Leading up to that, in chapter 2, I briefly recapture the relevant theory of linear and nonlinear oscillators. Some examples of physical pendulum systems are introduced. Chapter 3 discusses how nanomechanical resonators are modelled and the role they play in sensing applications. A brief overview of the field of nanomechanical sensing is made, with particular attention to recent advances enabled by the emergence of low-dimensional carbon materials. In chapter 4, I describe the physics needed to understand the superconducting analogous system, and in chapter 5, I touch upon the messy reality of nonequilibrium and fluctuating phenomena. After discussing my own work in chapter 6, I suggest some future lines of inquiry in chapter 7. Some tangential topics, as well as some more in-depth calculations, are covered in appendices. The thesis concludes with a popular science summary in Swedish.

2 Oscillator dynamics

Ever since a swinging chandelier caught the attention of Galileo Galilei, as the story goes [1], oscillating systems of various kinds have featured prominently in physics. There are two key reasons for this. First, the harmonic (or linear) oscillator is one of few models that can be solved exactly. Second, many potentials are approximately harmonic near their equilibrium, meaning that a broad range of problems can be treated as variations of the harmonic oscillator. Consequently, alongside its cousin, the anharmonic (nonlinear) oscillator, after more than four centuries, the harmonic oscillator remains at the forefront of physics research.

In this chapter*, I briefly discuss the mathematical description of linear and nonlinear oscillators, and consider some special cases that are of particular relevance to my work.

2.1 The harmonic oscillator

The simplest type of oscillator is a heavy, compact bob on a very light rod: a mathematical pendulum. If set swinging in Earth's gravitational field, the time-dependent angular displacement from the equilibrium position of the mathematical pendulum, $q(t)$ in figure 2.1, obeys the equation of motion

$$\ddot{q} + \frac{g}{L} \sin q = 0. \tag{2.1}$$

*This chapter was partly inspired by reference [1], the only case study-centered physics textbook I have encountered.

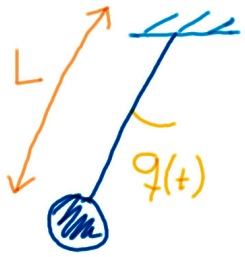

Figure 2.1: A mathematical pendulum with length L, whose angular deflection from equilibrium is $q(t)$.

Here, L is the length of the pendulum and g the gravitational acceleration. Defining the frequency $\omega = \sqrt{g/L}$ and considering small amplitudes, equation (2.1) becomes

$$\ddot{q} + \omega^2 q = 0. \tag{2.2}$$

This equation describes simple harmonic motion, and its solutions are trigonometric functions of ωt.

Driven and damped harmonic oscillators are often considered, in which case the displacement obeys

$$\ddot{q} + \gamma\dot{q} + \omega^2 q = F(t). \tag{2.3}$$

Here, γ is a damping rate and $F(t)$ is the driving force*. The response of an oscillatory system to a known drive can contain a wealth of information, and is often used in applications; see section 5.4.

A common case is when the driving force is periodic, $F(t) = F_0 \cos(\Omega t)$. Then, the solution to equation (2.3) is the sum of an exponentially damped solution that depends on initial conditions, and

$$q_{\text{res.}}(t) = \frac{F_0 \cos(\omega t - \vartheta)}{\sqrt{(\omega^2 - \Omega^2)^2 + \gamma^2\Omega^2}}, \quad \text{where} \quad \tan\vartheta = \frac{\gamma\Omega}{\omega^2 - \Omega^2}. \tag{2.4}$$

Due to its inverse dependence on $\omega^2 - \Omega^2$, the steady-state oscillation amplitude $F_0[(\omega^2 - \Omega^2)^2 + \gamma^2\Omega^2]^{-1/2}$ will become very large when the drive frequency Ω is close to the natural oscillation frequency ω of the pendulum. This *resonant response* is shown in figure 2.2 (a) for some different values of γ. As the damping

*Technically, all equations of motion in this chapter have been divided by the oscillator moment of inertia. It is nonetheless convenient to call $F(t)$ a force, despite it having dimensions of angular acceleration.

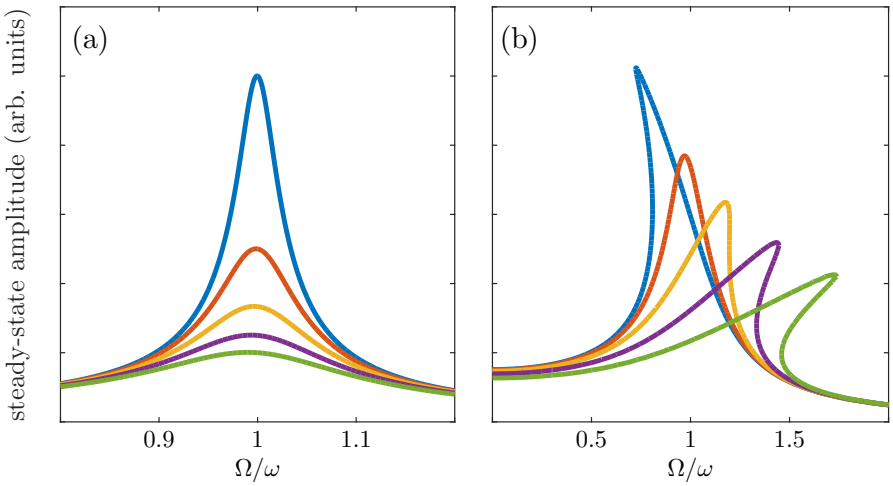

Figure 2.2: (a) Lorentzian response of a harmonic oscillator to a periodic drive for different γ. The peak maximum height is F_0/γ, and the full width at half maximum is 2γ. (b) Typical response of a Duffing oscillator to a periodic drive, for different α. Softened oscillators have $\alpha < 0$ and the curve points towards the left (blue and red lines), while the opposite is true for hardened oscillators (yellow, purple, and green lines).

decreases, the region of large amplitude response becomes very tall and narrow: a fact made use of in nanomechanical sensors, discussed in section 3.2. In nanomechanics, oscillators are often described by their *quality factor* (Q-factor); $Q = \omega/\gamma$.

Though widely applicable, the outlined theory of simple harmonic motion is an idealized model that does have shortcomings. One such is that many physical oscillating systems can support several harmonics, or *modes*. That is, more than one copy of equation (2.2) can describe the oscillator, each with a different value of ω:

$$\ddot{q}_n + \omega_n^2 q_n = 0, \;\; n = 0, 1, 2, \ldots, \tag{2.5}$$

and

$$q_n(t) = A_n \exp\left(i\omega_n t + i\varphi_n\right) \tag{2.6}$$

where the A_n (φ_n) are the amplitudes (phases) of each mode*. The harmonics correspond to different spatial profiles of the motion. While it would be very surprising to see a pendulum oscillate in anything other than its lowest harmonic [see figure 2.3 (a)], the higher modes cannot be disregarded in most vibrating solids. For example, as one plays a guitar, each vibrating string typically sounds both at its lowest harmonic and several higher ones [figure 2.3 (b)].

*The lowest harmonic – the *fundamental mode* – is customarily labelled as the zeroth one.

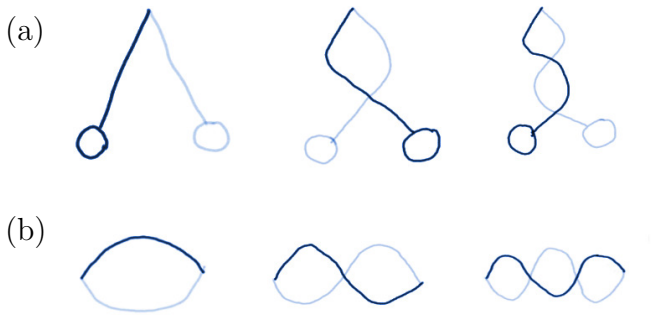

Figure 2.3: (a) Rarely-seen harmonics of a mathematical pendulum. (b) Harmonics of a vibrating string.

2.2 Anharmonic oscillators

While the simple harmonic oscillator outlined above is a useful model, it is a fact of the physicist's life that most of the world is not linear* (see also section 5.2). A nonlinear system – *anharmonic* in the case of oscillators – is characterized by that its response to external forces is more complicated than simple proportionality. This is mathematically reflected in that the equation of motion becomes nonlinear; the coordinate $q(t)$ and its derivatives can appear in other configurations than multiplied with a constant. Indeed, the general equation (2.1) is a nonlinear equation. In this section, a few relevant examples of anharmonic oscillators are discussed.

Perhaps the most obvious case of an anharmonic oscillator is obtained if more terms are kept in the expansion† of the $\sin q$ in equation (2.1). Including also the cubic term gives the Duffing equation

$$\ddot{q} + \gamma\dot{q} + \omega^2 q + \alpha q^3 = F(t), \tag{2.7}$$

here with linear damping and a driving force. Characteristic for the Duffing equation is its non-Lorentzian response to an harmonic drive; see figure 2.2 (b). As the frequency response curve bends into a "shark fin", the system becomes bistable. Then, the state of the system at a given drive frequency depends on how it arrived there. Experimentally, a signature of bistability is the existence of a hysteresis loop, sketched in figure 2.4.

Oscillatory systems can also become nonlinear due to external "complications"

*Stanislaw Ulam famously claimed that "using a term like 'nonlinear science' is like referring to the bulk of zoology as the study of non-elephant animals" (quoted in reference [2]).

†This is an intuitive way of thinking about the Duffing equation, but does not, in practice, imply that there is a fixed relation between the parameters ω and α.

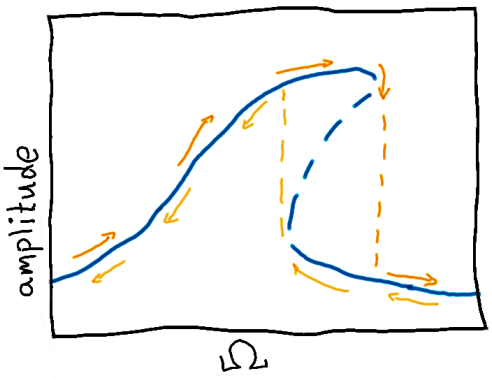

Figure 2.4: Bistable region of the response curve for a Duffing oscillator. The dashed part of the blue response curve is unstable; here, the pendulum will jump to the upper or lower branch depending on the path taken. The arrows pointing right (left) indicate which of the bistable branches that is measured as the drive frequency is swept up (down).

in their setup. One famous example is the Kapitza pendulum shown in figure 2.5 (a): a rigid pendulum whose pivot point is periodically driven in the vertical direction. The equation of motion for the Kapitza pendulum is

$$\ddot{q} + \omega^2 \sin q = -\frac{a}{L}\,\Omega^2 \cos \Omega t \;\; \sin q, \tag{2.8}$$

where a (Ω) is the amplitude (frequency) of the oscillation of the support. Intriguingly, when $a \ll L$ and $\Omega \gg \omega$, the downward equilibrium point $q = 0$, $\dot{q} = 0$ becomes unstable, while the upright equilibrium point $q = \pi$, $\dot{q} = 0$ becomes stable. For this reason, the Kapitza pendulum is an excellent classroom demonstration of the counterintuitive behaviour that nonlinear systems can exhibit; as the drive frequency is increased, the pendulum will rise and stabilize in an upright position*.

For small oscillation amplitudes q, equation (2.8) reduces to the Mathieu equation

$$\ddot{q} + \left(\omega^2 + \frac{a}{L}\,\Omega^2 \cos \Omega t\right) q = 0, \tag{2.9}$$

where the support drive acts as a periodic modulation of the constant natural frequency. Comparing equations (2.2) and (2.9), it is clear that the Mathieu equation can be viewed as an oscillator with a time-varying frequency.

An oscillator with time-dependent parameters is called *parametric*. Such oscillators can exhibit parametric resonance; if $\Omega \approx 2\omega$ (or, more generally, an integer

*A video of this phenomenon can be found at reference [3].

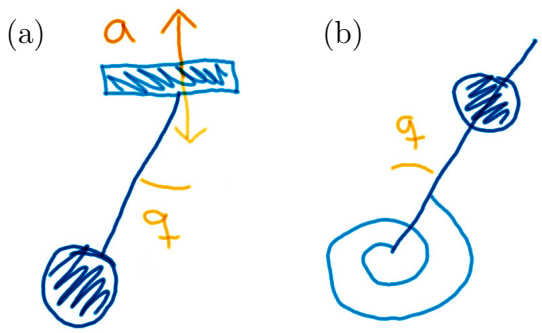

Figure 2.5: (a) A Kapitza pendulum; a rigid pendulum whose support point is harmonically driven with amplitude a and frequency Ω. (b) A Holweck-Lejay pendulum. The mass is free to move along the inverted rod, which is supported by a spiral spring.

multiple), any small perturbation away from $q = 0$ will grow to large amplitude. This is different from regular resonance in that for a parametric oscillator the amplitude has to be non-zero before it can resonantly increase, whereas the amplitude of the regular forced oscillator (2.3) will grow also from rest. Hence, parametric oscillators can act, for instance, as amplifiers.

A final example of an anharmonic oscillator is the Holweck-Lejay pendulum pictured in figure 2.5 (b). Described by

$$\ddot{q} + \gamma\dot{q} + \omega^2 q = F_0 \sin q, \tag{2.10}$$

the period of this inverted pendulum is very sensitive to changes in the downward, gravitational force, to which F_0 is proportional. Historically, the Holweck-Lejay pendulum was used in large-scale mappings of Earth's gravity in France and China [4].

Linear models are, in a sense, universal; the lessons learned from a bob on a string can be applied also to an LC-circuit; the behaviour of a pendulum with one frequency is (after some rescaling of variables) the same as the behaviour of another pendulum. In contrast, nonlinear models are more like unhappy families*; each one complicated in a unique way. However, a few qualitative features of nonlinear systems do tend to appear in many incarnations.

One such feature has been discussed in connection with the Duffing oscillator; bi- and multistability can only occur in nonlinear systems. A related feature is that, for a given value of the Duffing parameter α (with sufficiently large magnitude), there must be a certain drive frequency where the oscillator changes from

* "All happy families resemble each other; each unhappy family is unhappy in its own way" [5].

monostable to bistable. This is an example of a a *bifurcation*: a point where the dynamics of a system changes in a qualitative manner. Another example of a bifurcation occurs in the simple pendulum (2.1); if $|\dot{q}(0)| > 2\omega$, the pendulum will spin in large circles instead of oscillating back and forth [6].

Finally, nonlinearity is a necessary condition for a (finite-dimensional) system to exhibit *chaos*. Chaotic systems are more precisely described as highly sensitive to initial conditions, and are mathematically classified as such by measuring how fast nearby trajectories in phase space diverge. Determining this divergence rate is a nontrivial process, and there is generally no straightforward way to say whether a given system trajectory is chaotic or not. However, there exists signatures of chaotic motion that can at least give an indication. For example, if the time evolution of an oscillatory system is not periodic, the system either exhibits chaotic dynamics or is subject to noise (see section 5.2).

The great variety and complexity of nonlinear systems means that there is a near-endless supply of intriguing phenomena that I will not discuss in this thesis. However, even the brief account given here hints at, perhaps, the greatest practical difference between linear and nonlinear systems. A linear system can be studied in a fairly small parameter space, and its behaviour can be broadly generalized both to other parameter values and other linear systems. In contrast, a nonlinear system is not generalizable. What is learned in a certain situation does not, necessarily, apply in any other case. However, the bright side of this complication is is that nonlinear systems can exhibit dynamics far more rich and exciting than in linear systems.

3 Nanomechanical resonators

The theory of the previous chapter is not limited to the various pendulums used as illustrations, but can describe a host of different devices: electric circuits, children on the swings on a playground, and mechanical oscillators like vibrating cantilevers and beams. When the length, width, or thickness of such a mechanical oscillator approaches nanometer size, the oscillator is referred to as a *nanomechanical resonator**. In this chapter, I describe how I mathematically model these resonators, and how they can be used to create incredibly precise sensors. This precision might never have been achieved had it not been for the emergence of low-dimensional carbon nanomaterials, which are initially briefly discussed.

3.1 Carbon nanomaterials

Carbon may be the element of which allotropes were known the earliest, though it seems unlikely that diamond-miners millenia ago saw any connection between the gemstone they sought and the graphite they used to write. Alongside these old materials, a plethora of new carbon allotropes have emerged during the past century. Perhaps the two most thoroughly studied are graphene and carbon nanotubes.

Graphene – a single layer of carbon atoms arranged in a honeycomb lattice – was theoretically studied already in 1947, then as a stepping stone to describing

*The standard in the field is to use "resonator" for devices described by variants of equation (2.1), while the term "oscillator" is reserved for devices that *cause* oscillations; the difference is illustrated, for example, in reference [7]. This terminology is adopted henceforth.

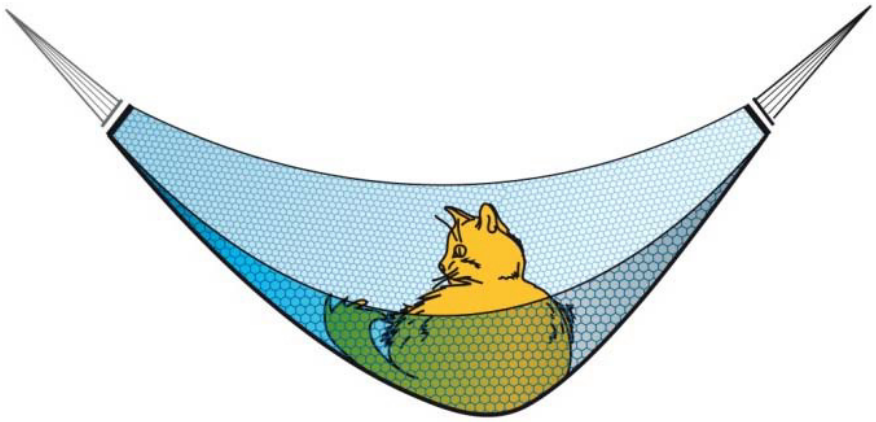

Figure 3.1: A cat sitting in a hammock made of graphene (honeycomb pattern not to scale). The hammock weighs less than one of the cat's whiskers, but is nonetheless strong enough to support the weight of the cat. Image from reference [23], Airi Iliste, © Kungl. Vetenskapsakademien. Reprinted with permission.

the band structure of graphite [8]. For graphene, the electronic band structure was calculated in 1970 [9], and the fact that electrons in graphene obey the Dirac equation was shown in 1984 [10, 11]. However, graphene was only considered a single-layer approximation of three-dimensional graphite, or perhaps an impurity stuck between the proper layers of a graphite crystal. It was not believed that a two-dimensional crystal could be stable at room temperature [12, 13]; when graphene was isolated [14] in 2004, the paper reporting the feat was rejected repeatedly [15]. As quickly as six years later, however, the Nobel Prize was awarded for "groundbreaking experiments regarding ... graphene" [16].

Singlewalled carbon nanotubes* can be thought of as graphene sheets that have been rolled up and pasted into cylinders. They were independently isolated in 1993 by two teams of scientists [17, 18]. Larger carbon filaments, that are today believed to have been multiwalled carbon nanotubes [19], have been studied since the 1950's [20], but the topic did not attract significant attention until 1991 [21].

The contrast between hard, transparent diamond and soft, opaque graphite underlines the fact that allotropes can have drastically different material properties, despite being formed by the same element. This is true also for graphene and carbon nanotubes, which are extraordinary also in a wider context, and not only when compared to other forms of carbon.

Graphene is the strongest [22] material in relation to its mass that is known today. An illustration of the strength of graphene is shown in figure 3.1; a ham-

*When referring to carbon nanotubes without a determiner, I always consider single-walled ones.

mock made from one square meter of graphene would weigh less than a milligram, but be strong enough to support up to four kilograms [23]. Carbon nanotubes also combine an extremely low mass with high tensile strength [24], something which has prompted suggestions that they might be woven together into a space elevator cable. Other properties of these nanomaterials seem tailor-made for applications and incorporation in devices. For instance, graphene has the largest surface area relative to mass there is, which translates to very high interaction cross-section with particles. The electrical conductivity of graphene [14] and the thermal conductivities [25–27] of both materials are also unprecedented. Finally, graphene is transparent [28] and flexible, leading to applications like solar cells [29], bendable touch screens [30, 31], and other types of flexible electronics [32].

3.2 Nanomechanical sensors

The majority of measurements done in physics are not direct measurements, where the quantity of interest is the one detected. Instead, most measurements are indirect; equipment is used that translates something easily-measured, a proxy variable, into another quantity, the target variable*. Measuring length using a ruler is a direct measurement, but a mercury thermometer translates volume to temperature, and an old-school kitchen scale translates the distance a spring is compressed to a mass†.

In section 2.1, I considered a mathematical pendulum, whose natural frequency depended on the gravitational force pulling on the bob. This is an example of a much more general fact; the frequency of an oscillating system is a function of the forces the system is subject to. This fact is indifferent to the nature of the forces involved, be they gravitional, electromagnetic, elastic, or more exotic. Consequently, using the resonant frequency as a proxy variable, resonator-based sensors have shown to be some of the most versatile measurement equipment developed.

The connection between force and frequency has long been exploited in non-contact atomic force microscopy (AFM), where a cantilever probe is oscillated at its resonant frequency a few nanometers above the surface of a sample [33–35]. Electromagnetic and van der Waals forces between the probe and the sample acts to decrease the oscillation frequency: $\omega \to \omega - \Delta\omega$. The relative frequency shift $\Delta\omega/\omega$ is proportional to the force gradient, so by recording the frequency variations, an image of the topology of the sample – or the charge or spin distribution on it – can be generated.

The AFM was originally conceived as an imaging tool, but its uses have ex-

*The terminology of proxy- and target variables is borrowed from statistics.

†Both kinds of measurements rely on correct calibration: that the scale of the ruler or the thermometer is accurate.

panded to include manipulation of nanostructures, resonant sensing, and much more [36, 37]. In a simultaneous development, resonator devices designed specifically for metrology [38, 39] have pushed the limits of sensing charge [40–44], force [45–48], position [49–51], spin [52, 53], and mass [54–61], including detecting when individual molecules attach to or detach from the resonator [62, 63]. Hollow nanoresonators that incorporate a fluid-filled channel can measure the masses of particles and bacteria suspended in the liquid [64–66]; this is only one of the applications behind the increasing prominence of nanomechanical components in chemical and biological sensors [67–75].

It is notable that quite a few of today's state-of-the-art sensors incorporate carbon nanotube [40–42, 48, 58–61, 76–78] or graphene [55, 63, 70, 79–82] resonators. The reason for this is that resonators fabricated from these materials, by virtue of their low mass, small size, and tolerance for being suspended under significant strain, can achieve very high resonance frequencies. This translates to a high sensitivity since, as for the AFM, the *relative* frequency shift is proportional to changes in force [38].

For example, adding a particle of mass m to a resonator of mass M causes a relative frequency shift $\Delta\omega/\omega \propto m/M$. If the human ear could detect a frequency shift of a few Hertz, it might be possible to *hear* the frequency shift resulting from a bumblebee landing on a vibrating guitar string, whose resonant frequency is around 100-300 Hz and whose mass is a few grams. In order to hear the adsorption of something smaller – detect a smaller m/M – one would either need better hearing (smaller $\Delta\omega$) or tune the guitar string to vibrate faster (larger ω). Nanomechanical sensing functions in much the same way. In sensing experiments, it is much easier to decrease the magnitude of $\Delta\omega/\omega$ by increasing the resonant frequency (making a device with larger ω), than by decreasing the frequency resolution (improving the performance of read-out equipment). Thus, a resonator with a higher bare frequency enables the detection of smaller perturbations.

In closing, I note that real-world sensors are now approaching the nanoscale. For instance, in anticipation of the need to be able to detect leakages from hydrogen-powered vehicles, a hydrogen gas-sensor has been developed [83]. The key component is a doubly clamped resonator beam coated with a layer of palladium, thirty nanometers thick. The resonant frequency of the beam changes as the coating chemically reacts with hydrogen, allowing the detection of hydrogen gas before its concentration becomes harmful. This sensor functions in room temperature at atmospheric pressure and high ambient humidity. Truly nanosized room temperature devices are also emerging; a graphene transducer [84] has been constructed, and suspended carbon nanotubes have been proposed to act as antennas in telecommunications devices [85].

3.3 Continuum mechanics description

Nanomechanical resonators are stiff, elastic bodies under deformation, and as such they can be modelled in the framework of continuum mechanics. For beams and plates that are mainly deformed in the transverse direction – they are bent, but not compressed – it is straightforward to show [86] that the Lagrangian is

$$\mathcal{L}_0 = \tfrac{1}{2}\rho\dot{w}^2 - \tfrac{1}{2}\sigma\left[\nabla w \cdot \nabla w\right] - \tfrac{1}{2}\kappa\left[\nabla^2 w\right]^2. \tag{3.1}$$

Here, ρ, σ, and κ are, respectively, the mass density, the stress, and the bending rigidity of the solid. The dot denotes the total time derivative, and $w(\mathbf{x}, t)$ is the flexural displacement of the solid at position $\mathbf{x}$ and time t; see figure 3.2.

The principle of least action leads to the equation of motion

$$\rho\ddot{w} - \sigma\nabla^2 w + \kappa\nabla^4 w = 0. \tag{3.2}$$

Without loss of generality, the displacement $w(\mathbf{x}, t)$ can be written as a linear combination of orthogonal resonator eigenmodes $\varphi_n(\mathbf{x})$:

$$w(\mathbf{x}, t) = \sum_{n=0}^{\infty} q_n(t)\varphi_n(\mathbf{x}). \tag{3.3}$$

The eigenmodes are solutions to

$$-\omega_n^2\rho\varphi_n - \sigma\nabla^2\varphi_n + \kappa\nabla^4\varphi_n = 0, \tag{3.4}$$

where ω_n is the vibration frequency of the n:th mode. It is now straightforward to show that the amplitude $q_n(t)$ of each vibrational mode acts as a harmonic oscillator*, since equation (3.2) transforms into a set of equations of the form

$$\ddot{q}_n + \omega_n^2 q_n = 0. \tag{3.5}$$

The exact form of the eigenmodes $\varphi_n(\mathbf{x})$ and eigenfrequencies ω_n depends on the geometry and boundary conditions of the resonator under consideration. In this thesis, the two relevant cases are a one-dimensional doubly clamped beam, and a two-dimensional drum pinned along the edges, shown in figure 6.4 (page 39). Their eigenmodes and -frequencies are discussed in some detail in appendix A.

*This is, of course, the reason for denoting both the angular displacement of a pendulum and amplitude of a resonator mode as $q(t)$. However, where the former is dimensionless, the latter is, in general, a length. In chapter 6, I normalize the mode amplitudes by defining them as divided with the length or radius of the resonator, thereby returning to dimensionless $q_n(t)$.

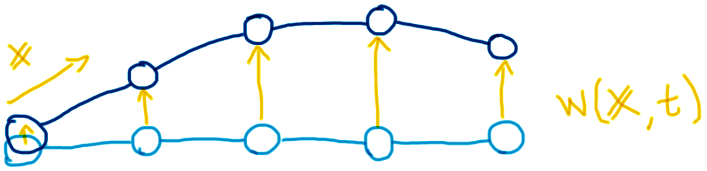

Figure 3.2: A chain of elements is deformed in the transverse direction. The displacement field $w(\mathbf{x}, t)$ contains the distance each element has moved. Note that the $\mathbf{x}$-coordinate system is attached to the chain, and is thus not an inertial frame of reference.

3.3.1 Limitations of the model

Some approximations have been made in the derivation of the above equations; see reference [87] for details. The first is that the solid considered only experiences flexural deflections. In reality, if the edges of a solid are fixed, as it is bent its length increases, so the solid must also be stretched. This longitudinal part of the displacement field is neglected based on that the the characteristic frequencies for the transverse oscillation of a nanoresonator are much lower than the frequencies of longitudinal vibration. Thus, for any deformation, the in-plane displacement field relaxes into a static state before the flexural displacement shows any discernible change. Consequently, longitudinal deformations can be neglected when considering the resonator dynamics.

The second approximation is that the trace of the stress tensor has been set to a constant; $\mathrm{Tr}\,\boldsymbol{\sigma} \equiv \sigma$. This is a valid approximation if the transverse displacement is small, which can be achieved by placing the solid under longitudinal strain; after all, a loose guitar string can be bent much more than one that is properly tuned.

On philosophical grounds, one might object to the use of continuum mechanics altogether; how can a classical theory – one that is routinely applied to the steel beams scaffolding our bridges and buildings – accurately describe a *nano*mechanical resonator? The key is that continuum mechanics performs very well as long as the solid can be considered homogenenous. That is, the length scale of any deformations must be much larger than the length scale of inhomogeneities in the solid being deformed. In the case of a (defect-free) carbon resonator, the length scale for inhomogeneities is the typical distance between atoms in the material: a few Ångström. The characteristic length scale for a deformation is the wavelength of a vibrational mode. For low-lying modes, this wavelength is a large fraction of the resonator size: of the order of a few tenths of a micrometer. This separation of length scales is more than enough to consider the resonator as a smooth, homogeneous solid, and continuum mechanics is then appropriate to use.

4 Superconducting circuits

Superconducting materials* are characterized by that, below a critical temperature T_c, their electrical resistivity abruptly vanishes [89] and surface currents are induced that cancel external magnetic fields [90], effectively turning the interior of the superconductor into a perfect diamagnet†. Superconductors have become the materials of choice whenever strong electromagnets are required, as in particle accelerators, maglev trains, railguns, and medical diagnostic technologies like magnetic resonance imaging and nuclear magnetic resonance. To a physicist, however, perhaps the most striking aspect of superconductivity is that it is a *macroscopic* manifestation of a *quantum* phenomenon.

Briefly, superconductivity arises due to that below T_c, lattice vibrations mediate a coupling of electrons near the Fermi surface into Cooper pairs [91]. A Cooper pair mimics the behaviour of a bosonic particle with twice the mass and charge of an electron [92]. Roughly similar to the formation of a Bose-Einstein condensate‡, the sea of Cooper pairs forms a *superconducting condensate* [90], that can be described by a single complex wave function.

In this chapter, I give a short overview of Josephson junctions, in which the

*Here, the discussion is limited to conventional superconductivity, described by the Bardeen-Cooper-Schrieffer (BCS) theory [88].

†A high enough external magnetic field will not be expelled, but instead destroy the superconductivity. Since a current will induce a magnetic field, it follows that there is a limit to how high a current a superconductor can support. This upper limit is the (material-dependent) critical current.

‡The electrons in a Cooper pair are only weakly bound together, contrasting with the strongly bound, di-fermionic molecules that would be required to form a true Bose-Einstein condensate (BEC) in a gas of fermions. If the electron-electron interaction strength can be continuously increased, it is in principle possible to turn the superconducting (BCS) condensate into a BEC [93, 94]. This BCS-BEC transition was first realized in 2004, in a gas of potassium atoms [95].

quantum nature of superconductivity is made manifest. In superconducting circuits*, these junctions are equally fundamental building blocks as inductors and capacitors. Contrary to the more familiar circuits elements, however, a Josephson junction is nonlinear: a fact that allows for the creation of artifical atoms.

4.1 Josephson physics and SQUIDs

If a superconductor is interrupted by a narrow barrier – a layer of a normal metal or a dielectric, or a spatial constriction – a Josephson junction is formed; see figure 4.1. It is not only possible that electrons tunnel through this barrier, but that intact Cooper pairs do. This type of tunneling causes a *supercurrent*

$$I_\mathrm{J} = I_\mathrm{c} \sin\varphi, \tag{4.1}$$

that flows without resistance across the junction [96, 97]. Here, I_c is the superconductor's critical current, and φ is the gauge-invariant† difference in condensate wave function phase between the two sides of the barrier. This phase difference evolves according to

$$\frac{\mathrm{d}\varphi}{\mathrm{d}t} = \frac{2\pi}{\Phi_0} V, \tag{4.2}$$

where V is the potential difference across the Josephson junction and $\Phi_0 = h/2e$ is the flux quantum, defined through Planck's constant h and the charge of the electron e. From the Josephson equations (4.1) and (4.2), it follows that the potential energy stored in a junction is

$$U_\mathrm{J} = \int I_\mathrm{J} V \mathrm{d}t = E_\mathrm{J}(1 - \cos\varphi), \tag{4.3}$$

where $E_\mathrm{J} = I_\mathrm{c}\Phi_0/2\pi$ is the Josephson energy.

Two Josephson junctions that are connected in parallel – achieved, for instance, by inserting two normal layers into a ring of superconducting material – forms a superconducting quantum interference device (SQUID) [99]; see figure 4.2. When

*Any circuit whose leads are made of a superconducting material is, when cooled below the relevant critical temperature, a superconducting circuit.

†In order to preserve gauge invariance under an external magnetic field, the actual phase difference $\Delta\phi$ has to be replaced [90] with

$$\varphi = \Delta\phi - \frac{2\pi}{\Phi_0} \int_\mathcal{C} \mathrm{d}\mathbf{s} \cdot \mathbf{A},$$

where $\mathcal{C}$ is a curve that crosses the junction. Since the vector potential $\mathbf{A}$ here appears explicitly, the phase shift resulting from a gauge transformation [98] will be immediately cancelled.

Figure 4.1: A Josephson junction consisting of a thin piece of a normal metal (N) sandwiched between two superconducting leads (S) .

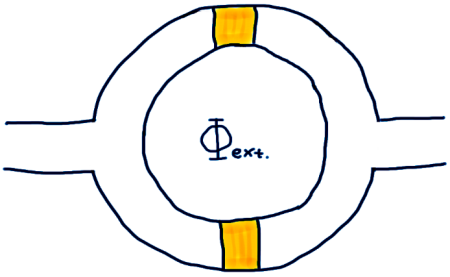

Figure 4.2: Two Josephson junctions in parallel forms a SQUID, threaded by the magnetic flux $\Phi_{\text{ext.}}$.

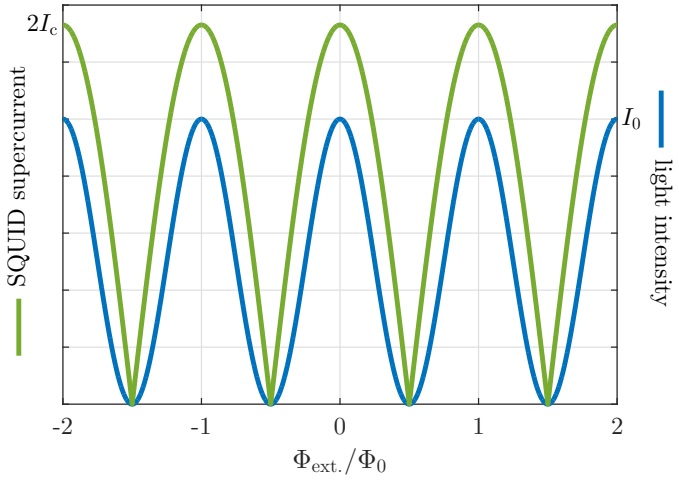

Figure 4.3: The magnitude of the SQUID supercurrent (4.5) ($Vt = \Phi_0/4$) as a function of the external flux, compared with the typical optical diffraction pattern of a double slit (where the slit separation $d = 2\lambda$ and the viewing angle θ relates to $\Phi_{\text{ext.}}/\Phi_0$ as $\pi\Phi_{\text{ext.}}/\Phi_0 = 2\sin\theta$). Tuning $\Phi_{\text{ext.}}$ changes the electromagnetic length that electrons have to travel through the SQUID, and thus the magnitude of the current. This is analogous to moving the observation point along the screen of an optical double slit experiment.

connected to a current source, the two branches of the SQUID become analogous to the slits of an optical double slit experiment; in both cases, particles (Cooper pairs and photons, respectively) can pass through a region of space only through two constrictions, small enough to make the particles instead behave as interfering waves; see figure 4.3. This is the quantum interference of the SQUID, and arises mathematically by considering the change in superconducting phase as a Cooper pair passes from one side of the SQUID to the other.

The phase change φ_{u} across the upper branch of the SQUID will not be the same as that across the lower branch, φ_{l}. The difference between the two is [100]

$$\varphi_{\mathrm{u}} - \varphi_{\mathrm{l}} = \frac{2\pi\Phi_{\mathrm{ext.}}}{\Phi_0} \pmod{2\pi}, \tag{4.4}$$

where $\Phi_{\mathrm{ext.}}$ is the magnetic flux threading the SQUID. This flux is a combination of the flux of any external magnetic fields, and of the magnetic field generated by the supercurrent through the SQUID.

Using equation (4.4), the total supercurrent I_{s} across the SQUID is obtained by summing the Josephson current (4.1) over the two branches of the SQUID. For identical junctions,

$$I_{\mathrm{s}} = 2I_{\mathrm{c}} \cos\frac{\pi\Phi_{\mathrm{ext.}}}{\Phi_0} \sin\frac{2\pi V t}{\Phi_0} \tag{4.5}$$

and the potential energy of the SQUID becomes

$$U_{\mathrm{SQ}} = 2E_{\mathrm{J}} \cos\frac{\pi\Phi_{\mathrm{ext.}}}{\Phi_0} \left(1 - \cos\frac{2\pi V t}{\Phi_0}\right). \tag{4.6}$$

The dependence of I_{s} on $\Phi_{\mathrm{ext.}}$ makes the SQUID exceptionally sensitive to magnetic fields. One of the more eye-catching applications of this is magnetoencephalography [101]; the mapping of activity in the human brain by measuring the minute electromagnetic fields generated by firing neurons.

4.2 Circuit quantum electrodynamics

Josephson junctions are integral components not only in the (dc) SQUID discussed above, but also in several circuit compounds that function as *artificial atoms*: macroscopic systems that have quantized energy levels and whose states can become entangled and superposed [102, 103]. A key feature in an artificial atom is that it has an anharmonic energy spectrum; its energy levels are not equidistant, so that specific transitions can be addressed. An LC-circuit is a harmonic oscillator with equidistant energy levels. Replacing the inductor with a nonlinear element, like a Josephson junction [103], changes the spectrum to the sought-after anharmonic

one.

Artificial atoms can be coupled to the electromagnetic field of the current running through a circuit or a transmission line, and particular field frequencies can be addressed by means of, for instance, coplanar waveguide resonators [104]. Superconducting circuit systems can thus offer an alternative to cavity quantum electrodynamics [105] when it comes to studying the interaction between light and matter: circuit quantum electrodynamics (cQED) [106–108]. In particular, cQED systems show great promise for quantum computing [109, 110].

The interaction between light trapped in a cavity and a two-level atom – or a superconducting circuit analogue – is frequently described by the Jaynes-Cummings [111, 112] Hamiltonian:

$$H_{\mathrm{JC}} = \hbar\omega_{\mathrm{c}} a^{\dagger} a + \tfrac{1}{2}\hbar\omega_{\mathrm{a}}\sigma_z + \tfrac{1}{2}\hbar\Omega(a\sigma_+ + a^{\dagger}\sigma_-), \tag{4.7}$$

here written in the (nearly always used) rotating wave approximation. The cavity mode has frequency ω_{c} and creation (annihilation) operator $a^{\dagger}$ (a); ω_{a} is the atomic transition frequency with σ_z the corresponding inversion operator; $\sigma_{\pm}$ are raising- and lowering operators of the two-level system, and Ω is the interaction strength. The interaction term in the Hamiltonian expresses that a photon can be annihilated by a as the two-level system is raised to its excited state by σ_+ – a photon is absorbed by the atom – and vice versa.

5 Fluctuations and nonequilibrium dynamics

The real world is not only frequently nonlinear, it also tends to be subject to fluctuations and noise, and to spend a fair amount of time out of equilibrium. In fact, a significant fraction of experiments in condensed matter physics concern transport or response properties: inherently nonequilibrium situations. As in the case of nonlinearities (see section 2.2), these issues often have to be dealt with on a case-by-case basis. In this chapter, some relevant aspects of fluctuations and nonequilibrium states are discussed. Frequently, a combination of complications can lead to rich and nonintuitive dynamics; for this reason, particular attention is paid to noise in nonlinear systems.

The smaller a system is, the larger is the influence of fluctuations on it [113–116], sometimes to the point where thermodynamical laws can be violated over short timescales [117, 118]. The nanomechanical sensors discussed in section 3.2 are generally small enough that thermal fluctuations – either thermally excited vibrations of the resonator [43, 45, 46, 48, 52, 119], or noise in the temperature, stiffness, or charge of the device [42, 55, 56, 120–122] – must be taken into account. Fluctuations in material parameters are inherited as fluctuations in the resonator frequency, which broadens the frequency response of a linear resonator and limits its sensitivity [54, 123, 124]. In the nonlinear case, the picture is far more complex, as I discuss in the overview of energy loss and frequency noise in nanomechanical resonators that closes this chapter.

5.1 Brownian particle diffusion in equilibrium

A system in *thermal equilibrium* is characterized by that its macroscopic system state variables (like volume and pressure) do not change over time, or if the system is isolated from its environment*. However, this does not mean, as the word might imply, that a system in equilibrium is completely static. On the microscopic level, the atoms and molecules making up the system are constantly moving. This causes *thermal fluctuations*, where the system randomly changes between all its available states. The probability of finding the system in a state with energy E at temperature T is given by the Gibbs distribution [125], proportional to $\exp[-E/k_{\mathrm{B}}T]$ where k_{B} is Boltzmann's constant. The exponential form of this distribution suggests that, in general, the mean values of macroscopic system state variables are very strongly favoured. This is the reason why thermal fluctuations rarely have an impact on the macroscopic scale.

One example of equilibrium fluctuations is that the atoms in a solid randomly vibrate around their equilibrium positions: in a crystalline solid, the lattice points. Each of these vibrating atoms will hit its neighbours, which hit theirs in turn, so that every atom affects the motion of all others over quite a long range. Hence, while there are only a few atoms that are in contact with a particle adsorbed on the surface of the solid, their motion is a superposition of the thermal motion of many more atoms. The net effect on the adsorbed particle is thus as if it was, at any given time, subject to a very large number of random "kicks". As a result, the particle will perform a random walk over the surface of the solid. It is generally reasonable to think of this random walk as a Brownian motion.

The position† x of the adsorbed particle of mass m is described by Newton's second law:

$$m\ddot{x} = F(t). \tag{5.1}$$

The sum of external forces, $F(t)$, here only includes forces exerted on the particle by the lattice vibrations. There are two qualitatively different contributions: one stochastic (random) and one dissipative.

The stochastic contribution to $F(t)$ is the random kicks discussed above. This random force is the sum of a large number of random variables (the thermal motion

*The second condition is necessary to separate equilibrium states from nonequilibrium steady states. A cooking pot standing on a turned-on stove will, eventually, be in a steady state, where its temperature is constant because the pot is heated by the stove at the same rate as it is cooled by the colder air in the kitchen. It is clear that a constant temperature is not sufficient to claim that the pot is in thermal equilibrium; if it is removed from the stove – isolated from (a part of) its environment – its state will change.

†For convenience, x is written as a scalar in this chapter. For $x \in \mathbb{R}^n$, the force $F(t)$ also becomes an n-dimensional vector, and there will be n copies of equation (5.1): one for each component of x.

of each lattice atom) and will thus tend to a normal distribution according to the central limit theorem [126,127]. Then, the stochastic force can be written as $\sigma\xi(t)$, where the stochastic process $\xi(t)$ is normally distributed. That is, at each time t, $\xi(t) \sim \mathcal{N}(0,1)$. The standard deviation of the stochastic force is σ. Setting the mean $\langle\xi(t)\rangle$ as zero* is based on the assumption that if the particle is stationary it will, on average, be kicked equally often in every direction. Finally, assuming that the net direction of the kicks at time t will not have any influence on the net direction at another time t' means that $\xi(t)$ is a white noise process with correlation function $\langle\xi(t)\xi(t')\rangle = \delta(t-t')$. While truly white noise is an idealization, as will be discussed also in section 5.2, it is an accurate approximation when the correlation time of the noise is sufficiently short.

The dissipative contribution to $F(t)$ arises if the particle is moving. Then, it will be "in range" of the lattice vibrations of a larger number of substrate atoms, in particular along the direction of motion. Consequently, the particle will meet more kicks along that direction. The net effect of this increased collision rate is a friction force between the particle and the substrate, that increases if the particle moves faster. This is modelled by including the term $-\eta\dot{x}$ in $F(t)$. Typically, a dissipation rate γ is defined through $\eta \equiv m\gamma$.

Combining the above, equation (5.1) can be written

$$m\ddot{x} + m\gamma\dot{x} = \sigma\xi(t). \tag{5.2}$$

This is the Langevin equation† [131, 132]. When σ is independent of the system state x the noise is called *additive*; x-dependent σ is discussed in section 5.2.

The fact that, in equilibrium, random forces [the $\sigma\xi(t)$ in equation (5.2)] always‡ occur together with friction (the $m\gamma\dot{x}$) is a reflection of the fluctuation-dissipation theorem [125,126]. In general, this theorem claims that the power spectrum (containing information about fluctuations) of a variable exposed to a field is proportional to the imaginary (or dissipative) part of the Fourier-transformed response function that determines how the variable reacts to that field [92, 133].

*A non-zero mean value of $\xi(t)$ can be taken into account by rescaling the dissipation rate γ.

†A much more careful derivation is certainly possible, for example from the Caldeira-Leggett model [128]. To read this thesis, however, an intuitive understanding of the Langevin equation is sufficient. The presented phenomenological argument is adapted from reference [129], and a similar line of reasoning appears in reference [130].

‡The fluctuation-dissipation theorem is valid as long as the system in question obeys detailed balance [126]. In the context of a random walker, the principle of detailed balance can be formulated as $p(x_A)w_{A\to B} = p(x_B)w_{B\to A}$. Here, $p(x_A)$ is the probability that the particle is found at position x_A and $w_{A\to B}$ is the transition rate (probability per unit time) for the particle to move from x_A to x_B. The equation of detailed balance thus expresses that, over time, the particle will move from x_A to x_B (a transition that, of course, requires that it is present at x_A to begin with) as often as it will move from x_B to x_A.

For the Langevin equation, the fluctuation-dissipation theorem becomes $\sigma = \sqrt{2m\gamma k_{\mathrm{B}}T}$. This relation can be found without involving linear response theory, by formally integrating equation (5.2) to find the particle velocity:

$$\dot{x} = v_0 e^{-\gamma t} + \frac{\sigma}{m}\int_0^t \mathrm{d}t'\ e^{-\gamma(t-t')}\xi(t'), \tag{5.3}$$

where $v_0 = +dotx(t=0)$. Equation (5.3) is then substituted in the equipartition theorem, $\frac{1}{2}k_{\mathrm{B}}T = \frac{1}{2}m\langle\dot{x}\rangle^2$, and the resulting double integral is evaluated using the properties of the stochastic process $\xi(t)$. Transient, nonequilibrium effects are eliminated by considering arbitrarily large times t.

The Langevin equation (5.2) expresses the system dynamics directly in terms of the fluctuating variable x. Another way to deal with stochastic quantities is to work with their probability density function $p(x, \dot{x}, t)$. In terms of this function, the probability P that a particle under the influence of a stochastic force will be at* position x and have velocity $\dot{x}$ at time t can be calculated as

$$P(x, \dot{x}, t) = \int_x^{x+\mathrm{d}x} \mathrm{d}x' \int_{\dot{x}}^{\dot{x}+\mathrm{d}\dot{x}} \mathrm{d}\dot{x}'\ p\left(x', \dot{x}', t\right). \tag{5.4}$$

The time evolution of a probability density function is determined by the Fokker-Planck equation. This description of a system is equivalent to the Langevin description, in that the dynamics captured is the same in the two cases, and there exists a general rule for how to arrive at the corresponding Fokker-Planck equation from a given Langevin equation [130] (see equation (5.7) below). For example, the Fokker-Planck equation corresponding to equation (5.2) is

$$\frac{\partial p}{\partial t} = \gamma p + \gamma\dot{x}\frac{\partial p}{\partial \dot{x}} - \dot{x}\frac{\partial p}{\partial x} + \frac{\gamma k_{\mathrm{B}}T}{m}\frac{\partial^2 p}{\partial \dot{x}^2}. \tag{5.5}$$

5.2 Noise in nonlinear systems

It is not uncommon that fluctuations in physical systems are thought of as a kind of heavy wet blanket, placed over and obscuring the sharp results that are beneath. Noise, one imagines, makes things a little bit harder to measure [134], but will not, on average, cause qualitative changes. While this picture can be accurate in linear systems, it typically fails in nonlinear ones [135]. For example, the presence of noise can alter where and if bifurcations occur (noise-induced transitions [136] and smearing of hysteresis loops [137]), or cause the system to switch between stable states [138]. Perhaps the most dramatic example of the counter-intuitive

*Here, I use "at" in the physicist's sense of "in a sufficiently small interval around".

effect that fluctuations can have is when their presence is *beneficial*, with *stochastic resonance* being the most extreme example.

In its original formulation [139], stochastic resonance is a synchronization phenomenon. The idea is that if there are two stationary points – or potential wells – in a system, the presence of noise will eventually cause the system state to switch from one well to the other. One estimation of the characteristic frequency of such escape events is the Kramers rate [140]. If the system is also driven by a weak periodic signal, whose frequency matches the Kramers rate, the switching between potential wells will pump the signal. This resonance effect can amplify signals far weaker than the strength of the noise to the point where they are detectable. Originally conceived as an explanation for very slow periodic variations in the average temperature of the Earth* [141,142], stochastic resonance has now been shown to occur in electronic circuits [143], optically levitated dielectric spheres from the micro- [144] to the nanoscale [145], nanomechanical resonators [146], crayfish neurons [147], and in the dynamics of the small hairs in mammal ears [148].

It has been argued that all cases of "helpful randomness" [149] that makes systems perform better in the presence of noise than in its absence – the reversal of the "wet blanket" idea – should be considered examples of stochastic resonance. One case where helpful randomness (different from traditional stochastic resonance) appears, is the ring-laser gyroscope† [151] used in inertial navigation. Here, randomness is not only helpful but crucial; when the noise is too weak, there is a dead band of low rotation frequencies where the gyroscope does not work as intended. This dead band can be narrowed and made to vanish by increasing the levels of noise [152, 153]. More recent examples of beneficial noise include a stochastic heat engine [154] and a thermally gated transistor [155]. Many biological systems also rely on randomly occurring events: in muscle contraction processes, neural signals, and the opening of channels in cell walls [156, 157].

It is clear that a nonlinear stochastic differential equation results if a stochastic force is added to a previously nonlinear differential equation‡: say, if the driving term $F(t)$ in the Duffing equation (2.7) is a Langevin term. It is also possible that a stochastic differential equation is nonlinear due to that the strength of the noise depends on the state of the system. Then, a generalized Langevin equation with the structure

$$\frac{\partial \mathbf{x}}{\partial t} = \mathbf{A}(\mathbf{x}, t) + \mathbb{B}(\mathbf{x}, t)\boldsymbol{\xi}(t) \tag{5.6}$$

has to be treated; the deterministic part $\mathbf{A}(\mathbf{x}, t)$ is the drift of $\mathbf{x}$, and $\mathbb{B}(\mathbf{x}, t)$ is the diffusion strength. This kind of *multiplicative* noise appears, for instance, if there

*To my knowledge, while stochastic resonance is now a well-studied phenomenon, its relevance in Earth's climate has, ironically, still not been confirmed.

†Traditional stochastic resonance can also be observed in the ring-laser gyroscope [150].

‡The "use and abuse" of this *Langevin approach* is extensively discussed in reference [130].

is noise in the parameters of a differential equation: say, if the mass or the friction in equation (5.2) fluctuates [158].

There is a built-in ambiguity in equation (5.6) [130, 159, 160]; if the stochastic force $\boldsymbol{\xi}(t)$ is thought of as giving the system a "kick" at time t, at what time is it decided how strong this kick is? In other words: how do the time arguments in $\boldsymbol{\xi}(t)$ and $\mathbb{B}(\mathbf{x}(t), t)$ relate to each other? In order for equation (5.6) to be well-defined, a rule must be defined to solve this ambiguity. From a mathematical perspective, all such rules are equally valid (but not necessarily equally easy to use). From a physical perspective, on the other hand, the microscopic details of the system of which the Langevin equation is a coarse-grained description [161] determine what is the correct interpretation rule. Essentially, it is a question of what kind of process the white noise $\boldsymbol{\xi}(t)$ is a limit of. Two versions of stochastic calculus have come to dominate the literature.

In Itō stochastic calculus [162], the strength of the stochastic force at time t is given by the state of the system a moment before; $\mathbb{B}(\mathbf{x}(t), t)$ is thought of as $\mathbb{B}(\mathbf{x}(t - \delta t), t - \delta t)$. This choice corresponds to evaluating the stochastic integral over the fluctuation term, $\int \mathbb{B}(\mathbf{x}(t), t)\boldsymbol{\xi}(t)\mathrm{d}t$, using the left-hand rectangular rule. The Itō formalism arises when a series of discrete stochastic impulses is approximated as a continuous white noise process [161], and is used in applied mathematics and financial modelling [127].

In physics, the standard choice is Stratonovich stochastic calculus [163]. Then, the stochastic integral $\int \mathbb{B}(\mathbf{x}(t), t)\boldsymbol{\xi}(t)\mathrm{d}t$ is evaluated using the midpoint rectangular rule, corresponding to that the strength of the kick is determined in the middle of the time interval that defines the impulse of the stochastic force. The Stratonovich formalism naturally arises [130, 159] when treating the white noise-limit of coloured noise, which has a finite correlation time τ_c so that $\langle \xi_i(s)\xi_j(t)\rangle = \delta_{i,j}\sigma^2\tau_\mathrm{c}^{-1}\exp\left[-\tau_\mathrm{c}^{-1}|t-s|\right]$. This is the type of noise that is most common in physical processes, and may be approximated as white when τ_c is very small compared to the other relevant timescales in the system. The limit $\tau_\mathrm{c} \to 0$ leads to a white noise process that is accurately treated in the Stratonovich way; an example is found in reference [135]. Stratonovich calculus also has the advantage that transformation of variables and partial integration works in the same way as in deterministic calculus.

Different choices of integration rules lead to different values of a stochastic integral. However, for a physical system, the evolution of the probability density function must be independent of the choice of stochastic calculus. It follows that the equivalent Fokker-Planck equation looks different depending on the formalism used; the Itō solution of a Langevin equation is identical to the Stratonovich solution of a slightly different Langevin equation, where the drift term has been rescaled. With Stratonovich calculus, the Fokker-Planck equation equivalent to

the general Langevin equation (5.6) is [126, 130]

$$\frac{\partial p}{\partial t} = -\sum_i \frac{\partial}{\partial x_i}\left[A_i(\mathbf{x},t)p(\mathbf{x},t)\right] + \frac{1}{2}\sum_{i,j,k}\frac{\partial}{\partial x_i}\left[B_{ik}(\mathbf{x},t)\frac{\partial}{\partial x_j}\left[B_{jk}(\mathbf{x},t)p(\mathbf{x},t)\right]\right]. \tag{5.7}$$

5.3 Nonequilibrium dynamics

It is easy to imagine the furor caused by Newton's formulation of his first law of mechanics [164]. To claim that a body in motion will stay in motion is to contradict the physical intuition of any child old enough to throw a ball, so ubiquitous are *nonequilibrium* processes where the state of a system changes over time. Of course, the matter is settled by the less-often-quoted second half of the first law; the body stays in motion unless acted upon by an external force. In most quotidian examples of dynamical systems, such external forces are unavoidable. Air molecules and floating dust collide with the pendulum of a clock, slowing it; small imperfections in the surface of a table hook into similar ones on a fork, causing friction that keeps silverware in its place.

Nonequilibrium systems have already appeared in this thesis. Any system where there is a driving force is out of equilibrium, like some of the pendulums in chapter 2 and the weakly driven, stochastically resonant systems discussed above. In fact, the very first system I mentioned – the mathematical pendulum (2.1) – would be in a nonequilibrium steady state once given an initial push.

The pendulum equations of motion discussed in chapter 2 are *initial value problems*; their dynamics is completely determined by the form of the differential equation, along with some initial value for deflection and angular rate of change. The equilibrium case ($q = 0$, $\dot{q} = 0$ and no external drive) is the trivial solution, that is typically considered fundamentally uninteresting. Instead, the study of initial value problems is almost exclusively a study of nonequilibrium states. In particular, chaotic dynamics (in the mathematical sense) is a nonequilibrium phenomenon.

In real systems, it can be very difficult to separate the effects of deterministic chaos and stochastic noise. Even one of the most decisive tests for chaos there is – the existence of a positive Lyapunov exponent – cannot differentiate between noise and chaos [165]. A time series that is irregular only due to noise can sometimes be discerned from one whose irregularity is only due to chaos by means of spectral analysis, or by calculating the respective Poincaré sections. However, in real data from nonlinear systems, both effects can be present simultaneously. Considering the counterintuitive way that noise can act in nonlinear systems, and adding high sensitivity to initial conditions, it is easy to see what a challenge is involved in

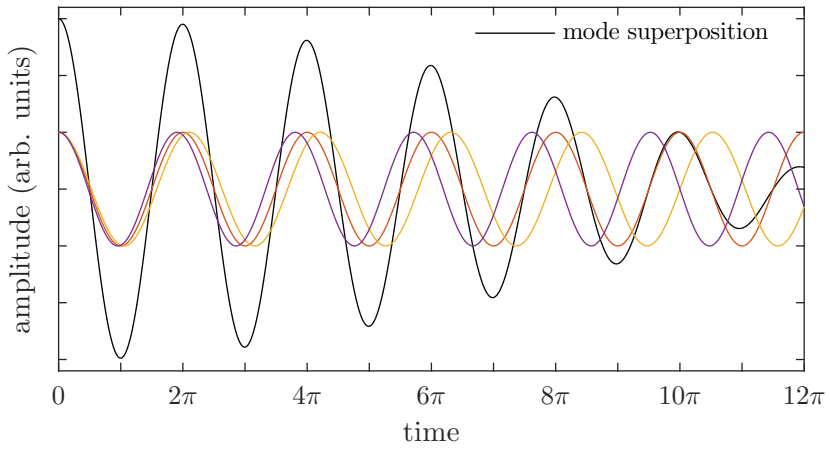

Figure 5.1: Superposition of three initially in-phase modes with slightly different frequencies. Despite there being no damping of individual modes, the total oscillation amplitude decreases due to dephasing. Inspired by a similar figure in reference [167].

predicting results in a noisy, chaotic system [166].

If a system in a nonequilibrium state can interact with a thermal environment, it will do so in order to return to its equilibrium state: a process known as *relaxation*. One simple functional form of a relaxation process is an exponential loss of energy proportional to $\exp(-\gamma t)$. This type of *dissipation* is common in oscillatory systems, where it results from a friction term $\gamma\dot{q}$ like the one in equation (2.3).

In multimode systems, the total amplitude of an oscillation can also decrease due to *dephasing*, a consequence of modes having different time dependence. Since an oscillation is typically the sum of several modes, if these interfere with each other, the total mode amplitude can change regardless of whether drive or damping is present. This is illustrated in figure 5.1, which shows the time evolution of three modes with the same phase, but slightly different frequencies. As the modes fall out of sync, the amplitude of their superposition decreases. Over a longer time period, the modes would once more line up and add constructively, followed by another decrease. In this way, dephasing can cause slow beats in the oscillation amplitude.

Dephasing can also occur if the phase of each mode [see equation (2.6)] has a time dependence. A case of particular interest is a system with a large number of modes present, where the phase of each fluctuates and the phase noise of different modes is uncorrelated; many vibrating solids can be described in this way. Then, no coherent beats in oscillation amplitude will be seen. Instead, since the phases are randomly distributed due to the noise, on average, the modes will add in a manner that decreases the oscillation amplitude [168]. This process is irreversible viewed over long time scales. In the context of nanomechanics, "dephasing" refers

to this kind of amplitude loss caused by random phase variation.

While the oscillation energy is unaffected by dephasing, what is measured in an experiment is typically the magnitude of the oscillation amplitude. Thus, dephasing can make it appear as if the energy of a system changes, and can be difficult to separate from dissipation. For instance, both effects causes resonance peaks (see figure 2.2) to broaden. The combined effect of dissipation and dephasing on amplitude is the *ringdown* of an oscillation.

5.4 Dephasing and dissipation in nanoresonators

The exceptional sensitivity of sensors based on nanomechanical resonators (see section 3.2) is a double-edged sword. Measuring small things involves monitoring the response of the sensor to a very small, *intentional* perturbation. It follows that an *unintentional* perturbation also causes a measurable response, but since this is an unplanned one, it becomes noise. As the proxy variable of a nanomechanical sensor is its resonant frequency, it is relevant to consider sources and consequences of frequency fluctuations [54, 169, 170]. Typically, "frequency noise" and "phase noise" are used synonymously.

As an illustrative example, I consider the frequency shift $\Delta\omega$ caused by adding a particle of mass m to a resonator of mass M:

$$\Delta\omega \approx \frac{\omega m}{2M}\phi^2(x). \tag{5.8}$$

Here x is the point where the particle adsorbs, ω is the bare resonant frequency, and ϕ is the mode shape of the resonator*. Fluctuations in any of the variables on the right-hand side of equation (5.8) will cause noise in the frequency shift, and hence in the measured frequency $\omega - \Delta\omega$.

One unplanned perturbation that, in this manner, could cause frequency noise is changes in m due to adsorption and desorption of other particles than the one being measured [61–63,171]. This kind of noise will not only cause dephasing that broadens the Lorentzian frequency response of the resonator, but can also change the number and shape of peaks in the spectrum [171,172]. Another source of phase noise evident in equation (5.8) is fluctuations in the position x of the particle [57, 61,62], which causes dephasing [173,174] and a bistable response to driving [175], as well as effects that are discussed in section 6.2. Finally, the bare resonant frequency ω is not immune to noise. As it is a function of material parameters (like the resonator's stiffness) and external factors (like the tension the resonator is under)

*The mode shape depends on the boundary conditions for the resonator and whether it is one- or twodimensional; see appendix A. For example, a string of length L vibrating in its fundamental mode has a mode shape $\phi(x) \propto \cos(\pi x)$, where $x \in [-L/2, L/2]$.

that can fluctuate, its value is not completely stable. In experiments to date, the dominant cause of frequency fluctuations [124] in nanomechanical resonators is noise in the experimental setup, arising at the resonator suspension points or in the measurement equipment connected to the resonator [7, 42–44, 53, 59, 60].

The suspension of nanomechanical resonators also introduces an intrinsic nonlinearity; as its deflection increases, a resonator whose edges are fixed must stretch. The resulting increased strain adds a nonlinear restoring force, typically modelled as a Duffing nonlinearity [176]. Additionally, graphene resonators have been shown to be nonlinearly damped [177–179]. These nonlinearities cause vibrational modes to be coupled together [180, 181], a mode coupling that, in turn, can cause anomalous, nonexponential dissipation [182–185] and non-Lorentzian spectra [186].

As several mechanisms contribute to broadening of the resonant response peak, as well as its shape, in order to study the dissipative dynamics in a nanomechanical resonator it does not suffice to consider its frequency response. Instead, time-domain experiments, like ringdown measurements [187–190], must be done. In a ringdown experiment, clever use of quadratures makes it possible to separate the amplitude loss that is due to dephasing and the amplitude loss that follows from the dissipation of energy. In this way, the dynamics of the latter can be isolated.

6 Dynamics of Brownian motion-coupled resonators

In this chapter, I summarize some results of papers I-IV concerning the nonequilibrium dynamics of resonators coupled to a noisy subsystem. The resonators are modelled as linear, but the coupling to the auxiliary system is not. Consequently, the equations of motion that I considered are quite nonlinear. This means that while the subsystems I have studied are some of the simplest and most well-studied in physics – harmonic oscillators and Brownian motion – their coupled dynamics exhibits a variety of intriguing effects. The research reported in this thesis primarily has the character of basic research. My main contribution to the the field is that I have investigated and created a record of new dynamics that might appear in future experiments, for instance when room temperature nanomechanics begins to breed applications.

I have studied the time evolution of coupled resonator-Brownian motion systems by numerically integrating their stochastic equations of motion, using a

second-order algorithm [191–193]. Numerical results were supplemented by analytical ones when possible, like in single mode-cases, and in limits of high or low noise.

The first three sections of this chapter are organized by realization of the resonator-Brownian motion system: a general, Hamiltonian model (section 6.1), a nanomechanical resonator with adsorbed particles (section 6.2), and a superconducting LC-resonator inductively coupled to a SQUID (section 6.3). In the summarizing section 6.4, I point out some connections between these three. A discussion of how my research can be continued is deferred to chapter 7.

The initial motivation behind considering the superconducting system was to recover resonator-diffusion dynamics in a system that would be easier to fabricate in the relevant parameter range than the nanomechanical one. Before arriving at the superconducting system discussed here, I investigated a dielectric sphere levitated in an optical cavity. This optomechanical system is described in appendix B.

6.1 Stepwise relaxation in a Hamiltonian model

A set of N harmonic oscillators coupled to a set of K free particle-degrees of freedom is described by the Hamiltonian

$$H = \frac{1}{2}\sum_{n=1}^{N}\left(\dot{q}_n^2 + \omega_n^2 q_n^2\right) + \frac{\mu}{2}\sum_{k=1}^{K}\dot{x}_k^2 - \frac{1}{2}\sum_{k,n,m} g_{mn} q_n q_m \phi_n(x_k)\phi_m(x_k). \tag{6.1}$$

Here, $g_{mn} = g_{nm}$ are coupling constants and the $\phi_n(x_k)$ specify the functional form of the interaction between oscillators and "particles". This very general model can be adapted to represent a wide range of physical systems. Despite the model's simplicity, its dynamics is rich and complex. In paper IV, I study a reduced version of the Hamiltonian (6.1), where the degrees of freedom were restricted to a minimal set. Even this minimal model retains quite intricate system dynamics. In this section, I discuss the main result of paper IV; the oscillator energy decays in a stepwise manner, connected to unpredictable trapping-retrapping behaviour of the particle degree of freedom.

The minimal model includes two degenerate oscillators and a single particle; $N = 2$, $K = 1$, and $\omega_1 = \omega_2 \equiv \Omega$. The coupling matrix is set to $g_{mn} = g$, and $\phi_1(x) = \sqrt{2}\cos\pi x$, $\phi_2(x) = \sqrt{2}\sin 2\pi x$. The position x is normalized and constrained to remain in a unit interval; $x \in [-1/2, 1/2]$. Thermal noise is not considered, but a friction term for the particle is included. Thus, the equations of

motion for the minimal model are

$$\begin{aligned} \ddot{q}_1 + \left[\Omega^2 - g\phi_1^2\right] q_1 - g\phi_1\phi_2 q_2 &= 0, \\ \ddot{q}_2 + \left[\Omega^2 - g\phi_2^2\right] q_2 - g\phi_1\phi_2 q_1 &= 0, \\ \ddot{x} + \gamma\dot{x} - \frac{g}{2\mu}\partial_x \left[(q_1\phi_1 + q_2\phi_2)^2\right] &= 0. \end{aligned} \tag{6.2}$$

Equations (6.2) were numerically integrated using a second order method: essentially the one discussed in references [191–193] with the coefficients of the stochastic force set to zero. The reason why I did not use a more sophisticated integrator is that x evolves under reflecting boundary conditions, which are non-trivial to include in higher-order methods adapted to initial value problems. The typical initial condition used was nonzero q_1 and x, and $q_2 = 0$, $\dot{q}_1 = \dot{q}_2 = \dot{x} = 0$. After the initial displacement of the q_1-oscillator, the free evolution of the system was simulated, and its relaxation studied.

The equations of motion (6.2) are deceptively simple; two coupled harmonic oscillators, whose frequencies and coupling strength depend on the position of the particle. This particle, in turn, moves in a time-dependent potential $U(x,t)$ defined by the oscillators; $U(x,t) \propto (q_1\phi_1 + q_2\phi_2)^2$. While this may sound like a textbook problem – perhaps tricky, but ultimately straight-forward – the reality is much more involved, due to the interdependence of the variables q_1, q_2, and x.

The x-equation of (6.2) describes particle motion in a potential. One thus expects that, for a low enough particle energy, x will be trapped near some minimum of the potential. Conversely, for a high enough particle energy, x will move above all potential barriers and seem free. On short timescales, this is indeed what happens. However, interference between the q_1- and the q_2-oscillators will, over longer timescales, change the depth, number, and location of the potential wells. This results in particle dynamics that switches between trapped and free regimes, as illustrated in figure 6.1 (b).

As the particle friction term is the only source of dissipation in equations (6.2), it is not surprising to see that regions of large particle motion in figure 6.1 (b) correspond to regions of high dissipation of oscillator energy ($E_n = \dot{q}_n^2 + \omega_n^2 q_n^2$, $E = \sum_n E_n$) in figure 6.1 (a). When the total and individual oscillator energies change, so does the shape of the potential that x moves in. In other words: the freely moving particle causes dissipation; because of this dissipation, the potential that the particle moves in changes, and can become deep enough to trap the particle again. The switch from free to trapped motion is a rapid process, that, as the region traversed by the particle is rapidly restricted, causes the oscillator dissipation rate to sharply shift to a much lower value. The resulting stepwise relaxation of the oscillators is shown in figure 6.1 (a). The particle decay rate γ influences how easy it is for the particle to escape a potential trap; figure 6.1 (c)-(f)

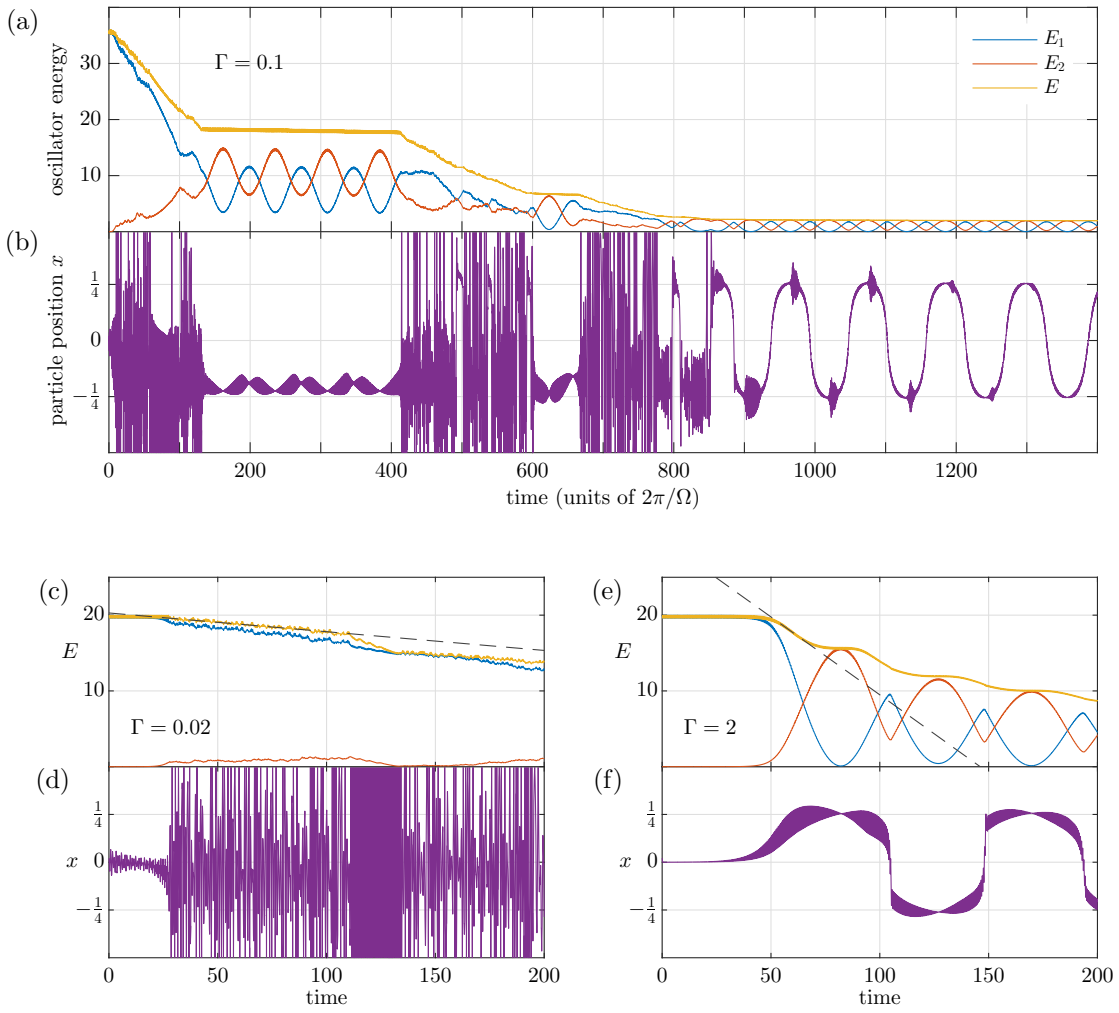

Figure 6.1: Time evolution of the energies of individual oscillators in the minimal Hamiltonian model, along with their total energy, at (a) intermediate, (c) low, and (e) high decay rate γ (Γ in the figure). The stepwise decay of total oscillator energy E is clear, as well as coherent coupled oscillations at the low-dissipation energy plateaus. These plateaus correspond to a trapped particle, and vice versa, as can be seen in the simultaneous evolution of the particle coordinate in (b), (d), and (f). The gray dashed lines illustrate that, over short times, the energy decay is linear.

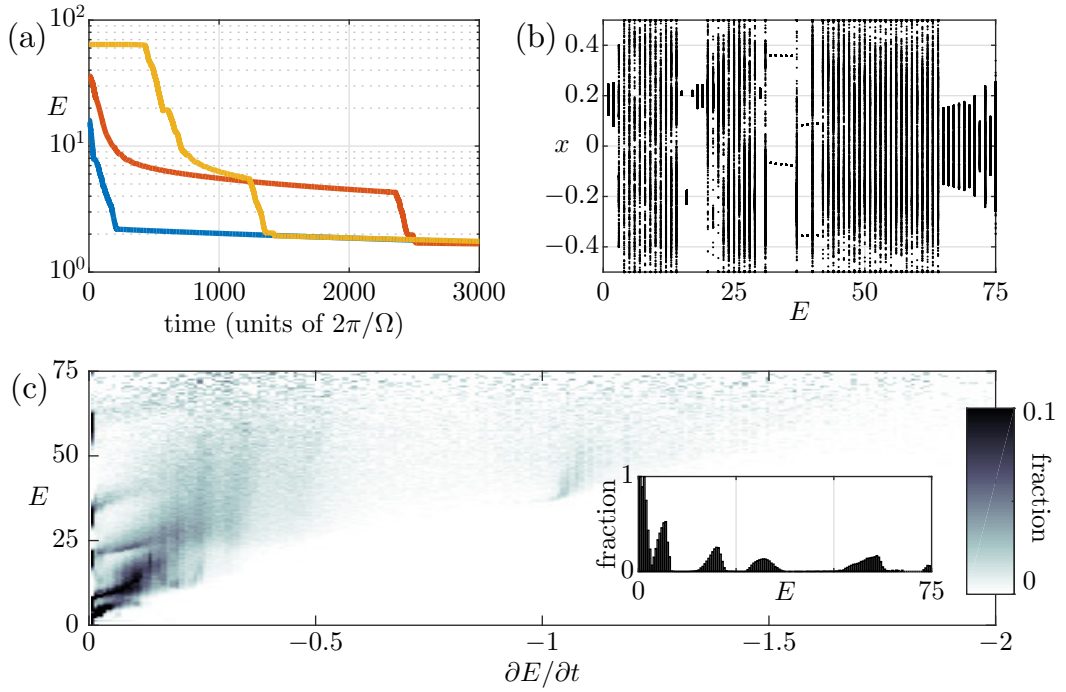

Figure 6.2: (a) Stepwise decay of total oscillator energy, at different initial conditions and $\gamma = 0.2$. (b) Periodicity diagram of the particle motion for a wide range of oscillator energies; each point is the position $x(t)$ when $\dot{x}(t) = 0$. Hence, exactly two points for a given E indicates that the particle here moves periodically. (c) Distribution of dissipation rates during the ringdown, as a function of energy. The color indicates the fraction of time spent at a certain energy that is also spent at a certain dissipation rate $\partial E/\partial t$. Fractions equal to or greater than 0.1 are coloured black. Inset: Distribution of energies for which $|\partial E/\partial t| < 0.05$: the low-dissipation plateaus of the ring-down.

illustrates the underdamped (low γ) and overdamped (high γ) system dynamics.

The stepwise decay of oscillator energy is a stable feature, that does not vanish when averaging a large number of ringdowns. As can be seen in figure 6.2 (a), the energy plateaus appear at similar energies, for quite different initial conditions. This fact is solidified in figure 6.2 (c). For each timestep in the numerical integration of equations (6.2), the value of E and a finite difference-approximation of $\partial E/\partial t$ was recorded. Repeating this process over many ringdowns gives a kind of energy phase space distribution of time spent at each point $(E, \dot{E})$. Figure 6.2 (c) is a density plot of this data from 10^5 trajectories with random initial conditions, normalized* so that the density for every E adds to 1. There is a definite structure of correlations between the value and the decay rate of oscillator energy, that

*That is, if the ringdown passes a certain energy E, the probability that it there takes some value of $\partial E/\partial t$ is 1. The opposite is clearly not true.

is particularly clear for the plateaus of very small $|\partial E/\partial t|$ shown in the inset of figure 6.2 (c).

Figure 6.2 (b) is a Poincaré-like diagram of the particle dynamics. Here, the total oscillator energy was conserved during the numerical integration by normalizing the coordinates $q_n, \dot{q}_n$ with $\sqrt{E(0)/E(t)}$ in each timestep, allowing the system dynamics in a particular regime to be studied. For each value of E, the value of x when $\dot{x} = 0$ was plotted. Thus, if there are only two x-points for a given E, the particle performs periodic motion between these two extrema. This is the case for $E \approx 30$. For $E \approx 0$ and $E \approx 20$, the particle is trapped in a narrow region near a potential minimum. Comparison with the inset in figure 6.2 (c) further emphasizes that the oscillation energy plateaus correspond to regions of trapped, regular particle motion. The sharply delineated regions of regular and irregular particle behaviour bring to mind the Poincaré diagrams of chaotic systems.

While I have not determined if the particle dynamics in the untrapped regions is indeed chaotic, the erratic and unpredictable behaviour of this nonlinear system is certainly suggestive. Also implying chaotic dynamics is figure 6.3, which shows the dependence of $\Delta x = \max x(t) - \min x(t)$, $t \in [1200, 1500]$ on oscillator energy E and particle damping rate γ, when using the energy-conserving normalization. The difference Δx is the fraction of its domain traversed by the particle, after initial transients have vanished (compare with figure 6.1), and indicates if a particle trajectory is trapped and regular ($\Delta x \lesssim 0.7$) or if it is irregular (higher Δx). The overall look of the diagram in figure 6.3 is somewhat similar to the Arnold tongues [6] of the Mathieu equation (2.9), but on a smaller scale the regions of trapped, regular particle dynamics look almost fractal. Even if this complexity is not true chaos, a comparable level of unpredictability is clearly inherent in the dynamics of the system (6.2).

Even when only considering the reduced version of the Hamiltonian (6.1) that I discussed in this section, complicated dynamics arise that are not yet completely understood. Nevertheless, the more experimentally relevant systems that are the subject of the remainder of this chapter can be derived from (6.1), under certain limitations and approximations. Consequently, despite its complexity, the general model can illuminate some aspects of the systems of papers I-III.

6.2 Nanomechanical resonators with adsorbed particles

The dynamics of K noninteracting, identical particles loosely adsorbed on and diffusing across the surface of a nanomechanical resonator (see figure 6.4) with N

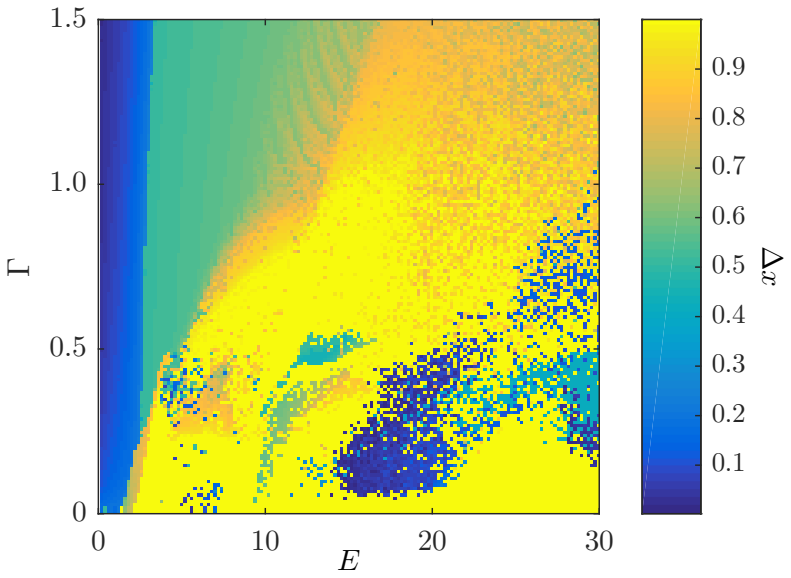

Figure 6.3: The distance Δx between minimum and maximum values of x (compare with the particle trajectories in Fig. 6.1) as a function of damping rate γ (Γ in the figure) and oscillator energy E. States with $\Delta x \lesssim 0.7$ are trapped near one or both of the potential well at $x \approx \pm 0.25$, and evolve in a predictable manner. The untrapped states are typically irregular and unpredictable.

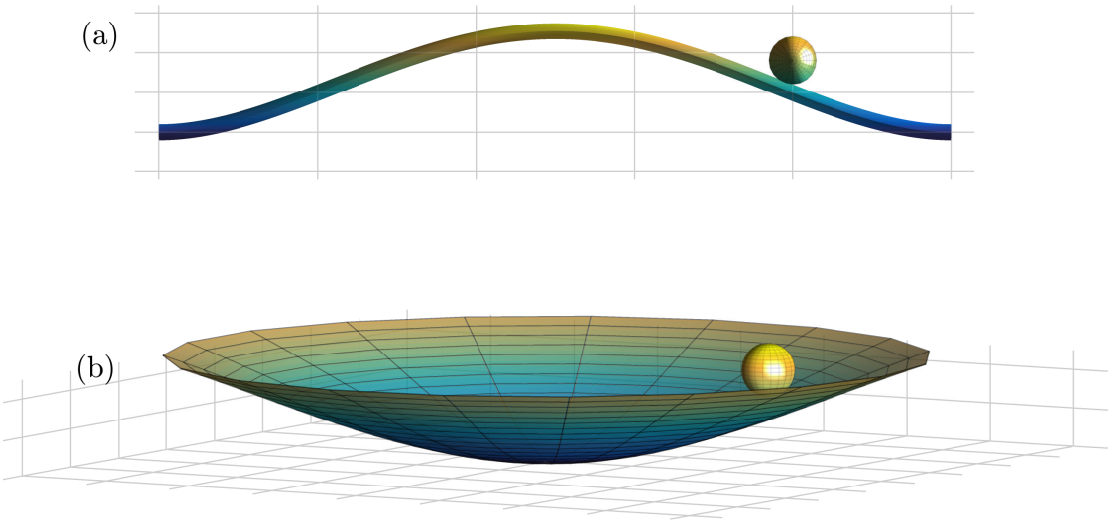

Figure 6.4: A particle adsorbed on the surface of a suspended (a) carbon nanotube beam resonator (b) graphene drum resonator. Thermal fluctuations cause the adsorbate to perform a random walk over the resonator surface, which induces dissipation in the vibrational motion. Here, only a single adsorbed particle is shown for clarity.

flexural vibrational modes is described by the equations of motion

$$\ddot{q}_n + \omega_n^2 q_n - \epsilon \sum_{m=1}^{N} \sum_{k=1}^{K} \omega_m^2 q_m \phi_n(\mathbf{x}_k)\phi_m(\mathbf{x}_k) = 0, \tag{6.3}$$

$$\ddot{\mathbf{x}}_k + \gamma \dot{\mathbf{x}}_k - \sum_{m,n} \omega_m^2 q_m q_n \phi_m(\mathbf{x}_k)\nabla\phi_n(\mathbf{x}_k) = \gamma\sqrt{2D}\ \boldsymbol{\xi}_k(t). \tag{6.4}$$

The coupling constant is here $\epsilon = m/M$, the ratio between the mass of a single particle and the mass of the resonator; the particles are set to be identical, and the dissipation constant $D = k_\mathrm{B}T/m\gamma$. In equations (6.3)-(6.4), the geometry of the resonator is determined by defining ϕ_n and ω_n as the appropriate mode shapes and mode frequencies; see appendix A. Choosing the resonator geometry in turn determines if the particle's position $\mathbf{x}_k$ and the stochastic force $\boldsymbol{\xi}_k$ are one- or twodimensional. Some details regarding the integration algorithm in the case of twodimensional diffusion in polar coordinates are found in appendix C.

The equations of motion (6.3)-(6.4) are found by variation of the Lagrangian for the entire system: the sum of the resonator Lagrangian (3.1) and the kinetic energy of the particles

$$\mathcal{T} = \frac{1}{2} m \sum_{k=1}^{K} \delta(\mathbf{x} - \mathbf{x}_k) \left[\dot{\mathbf{x}}_k^2 + (\dot{w} + \dot{\mathbf{x}}_k \cdot \nabla w)^2\right], \tag{6.5}$$

where $w(\mathbf{x}, t)$ is the transverse displacement field of the resonator; see section 3.3. For low-lying modes, the equations of motion (6.4) capture the same qualitative dynamic as those following from the general Hamiltonian (6.1); for details, see paper IV.

As in the case of the general system discussed in section 6.1, in this nanomechanical system, the action of the particles on the resonator and vice versa causes unconventional dynamics. I have studied this type of resonator-particle system in papers I, II, and IV; the primary results are summarized below.

6.2.1 Particle motion: inertial trapping to free diffusion

The particles adsorbed at positions $\mathbf{x}_k(t)$ perform Brownian motion in the inertial potential $U(\mathbf{x}_k, t) \propto w^2(\mathbf{x}_k, t)$. When the motion is dominated by a single mode – the typical situation in the beginning of a ringdown measurement – the inertial force corresponding to $U(\mathbf{x}_k, t)$ is proportional to $q_n^2(t)\phi_n(\mathbf{x}_k)\nabla\phi_n(\mathbf{x}_k)$. This force is always directed towards an antinode of the mode function, where the coupling term of equation (6.4) vanishes. Hence, the particles adsorbed on the resonator act as beads on a string that is twirled; they are pulled towards the point of maximal

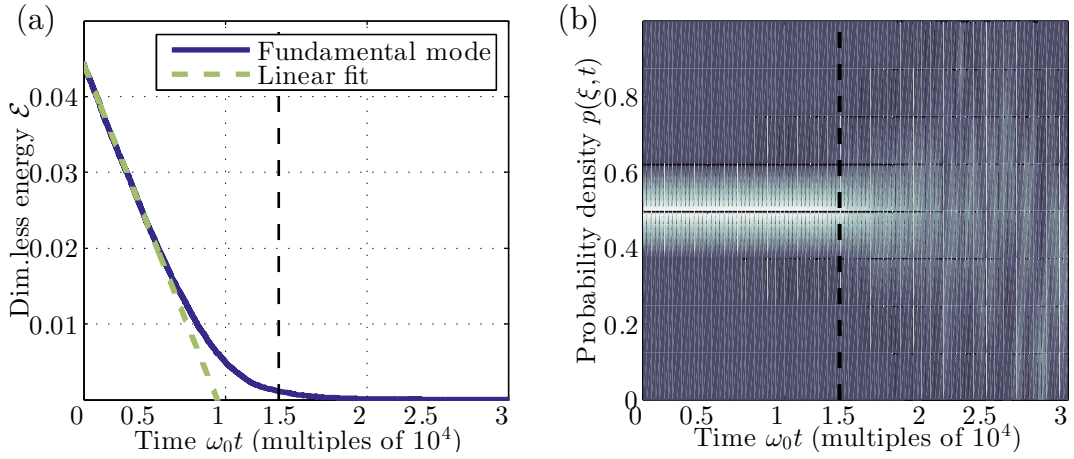

Figure 6.5: (a) Ringdown of the fundamental mode energy E_0 ($\mathcal{E}$ in the figure) of a carbon nanotube resonator. (b) Corresponding probability density $p(x,t)$ (the coordinate x is denoted ξ in the figure) of particle positions for a single trajectory. At high resonator amplitude, the particles are trapped near the antinode of the mode function (the length of the nanotube is normalized to one). The strength of the inertial trap decreases with the amplitude, until the particles can escape and diffuse across the entire resonator. With this escape, the resonator dissipation switches from linear to algebraic.

resonator deflection. As the resonator amplitude decreases, so does the strength of the inertial trap, and eventually the particles escape to diffuse freely across the resonator. This long-timescale behaviour is shown in figure 6.5.

When a single mode dominates the resonator motion, the dynamic regime of the system is determined by the ratio $\frac{1}{2}m\omega_n^2 q_n^2/k_\mathrm{B}T \equiv E_\mathrm{vib.}/E_\mathrm{therm.}$; the ratio between the kinetic energy of each particle due to the resonator vibration, and the thermal energy. When $E_\mathrm{vib.}/E_\mathrm{therm.} \gtrsim 1$, the particles are inertially trapped, and when the ratio falls below one, they escape to diffuse freely.

On short timescales, in the trapped regime, the periodic motion of the resonator leads to a periodically varying force on the particles, illustrated in figure 6.6. As the particles are alternately forced towards the resonator antinode (as the resonator deflection $|q_n|$ increases towards its maximum) and diffuse away from it (as the resonator approaches its relaxed state $q_n = 0$), the ensemble of adsorbed particles oscillate in a kind of breathing mode where the distance from the potential minimum to each particle on average varies with frequency $2\omega_n$. The fact that the particle positions $\mathbf{x}_k$ change not only in a Brownian manner but also contain this periodic component causes a periodic modulation of the effective mode frequency $\tilde{\omega}_n^2 = \omega_n^2\left[1 - \epsilon\sum_k \phi_n^2(\mathbf{x}_k)\right]$ (the combination of the term with $m = n$ in the sum of equation (6.3) and the q_n-term outside the sum). However, since it takes a

finite time for the particles to respond to the inertial forcing, the particle ensemble breathing mode is out-of-phase with the resonator motion. Consequently, this periodic frequency modulation results in parametric *attenuation*; compare with equation (2.9) and discussion thereof.

6.2.2 Diffusion-induced dissipation of resonator energy

The particle-generated parametric attenuation of resonator energy discussed above is the source of the linear dissipation seen in the trapping regime in figure 6.5 (a). Using a single-mode approximation $w(\mathbf{x}, t) = q_0(t)\phi_0(\mathbf{x})$, the dissipation of resonator energy can be analytically studied.

In the trapped regime, where particles remain in the vicinity of the antinode, the mode functions in equation (6.4) can be expanded. The Langevin equation describing particle motion then becomes linear in $\mathbf{x}_k$ and can be solved, assuming that the evolution of q_0^2 is much slower than the particle dynamics; see papers I and II for details. The end result is that the mean fundamental mode energy obeys

$$\frac{\partial \langle E_0 \rangle}{\partial t} \approx 2T_{\text{sim.}} K z_K(t) I\left[z_K(t)\right], \tag{6.6}$$

where K is the number of particles, and the dimensionless simulation temperature $T_{\text{sim.}} = k_{\text{B}}T/ML^2\omega_0^2$ with L the length (radius) of a beam (drum) resonator. The integral $I(z)$ is

$$I(z) = \frac{1}{2\pi}\int_0^{2\pi} \mathrm{d}t \sin 2\omega_0 t \int_{-\infty}^{t} \mathrm{d}t' e^{-z\int_{t'}^{t}\mathrm{d}t''\cos^2 t''}, \tag{6.7}$$

and $z_K = -2\gamma^{-1}\phi_0(0)\phi_0''(0)E_0(t)$. When E_0 (and hence z_K) is large*, $I(z_K)$ asymptotically approaches $-2/z_K\sqrt{\pi}$ and equation (6.6) can be integrated, revealing a linear decay of energy:

$$\langle E_0 \rangle(t) = E_0(0) - \alpha_K t, \quad \text{with} \quad \alpha_K = 4T_{\text{sim.}} K\pi^{-1/2}. \tag{6.8}$$

Since $k_{\text{B}}T = Dm\gamma$, $\alpha_K \propto Km$: the total added mass. Considering that in the trapped regime particles are forced together at the antinode, it is reasonable that only the total adsorbed mass, and not what number of particles it is distributed among, plays a significant role in determining the dissipation rate.

As shown in figure 6.7, equation (6.8) holds for both the graphene and the carbon nanotube resonator, over several orders of magnitude of $z_K \propto \gamma^{-1}E_0(0)$.

*In this context, "large" means resonator amplitudes that are much larger than the amplitude of thermally excited vibrations. Oscillations can be large in this sense while still remaining small enough that the continuum mechanics model is valid, as discussed in section 3.3.1

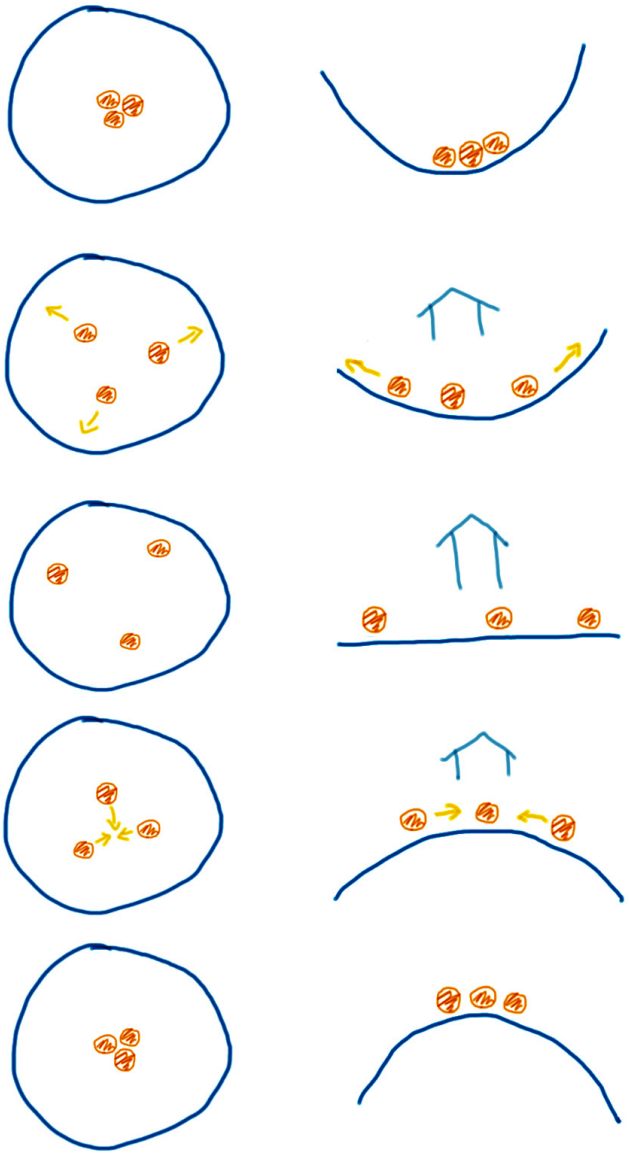

Figure 6.6: Trapped regime short-timescale dynamics of an ensemble of particles adsorbed on a nanomechanical drum resonator oscillating in its fundamental mode. On the left, the resonator is viewed from above, and on the right, from the side. From top to bottom: When q_0 takes its maximum negative value, the particles are trapped at the fundamental mode antinode. As $|q_0|$ decreases and $|\dot{q}_0|$ increases, the particles begin to diffuse away from the antinode. They reach a characteristic distance $\propto k_{\mathrm{B}}T$ when the resonator is momentarily relaxed ($q_0 = 0$, $\dot{q}_0$ maximal). As the resonator deflection begins to increase once more, the process is reversed. The inertial trap reforms, forcing the particles to the resonator antinode once more.

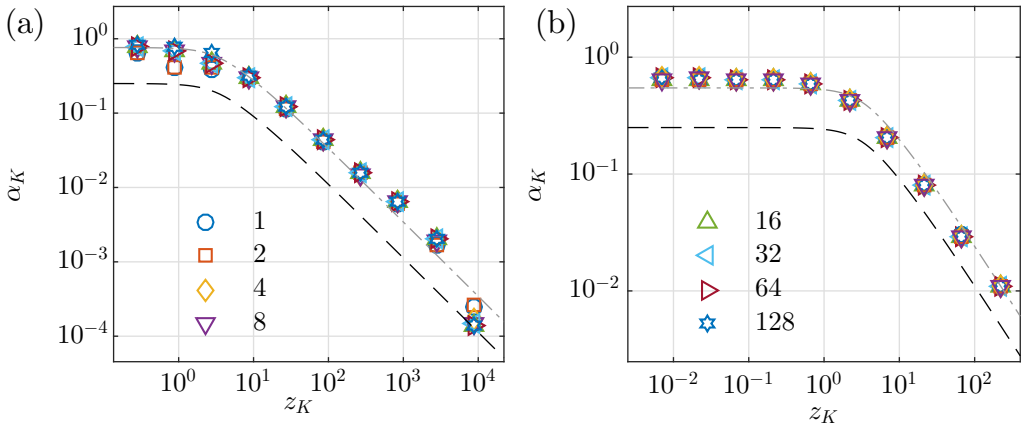

Figure 6.7: Dissipation rate α_K together with $|I(z)|$ (black dashed line) as functions of z_K for (a) a carbon nanotube resonator and (b) a graphene resonator. Here, $N = 1$ and K is given by the legend. The gray dash-dotted line is $|I(z)|$ shifted vertically to fit the data points, in order to show the excellent qualitative agreement between analytical and numerical results.

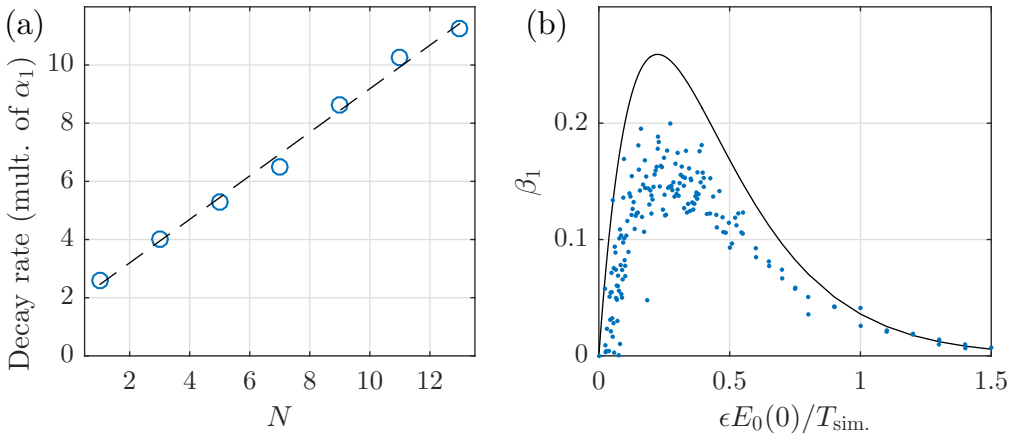

Figure 6.8: (a) Initial linear decay rate of resonator energy for a carbon nanotube resonator for different numbers of modes N in the simulation (blue circles), with a linear fit (dashed line); $K = 1$. (b) Comparison of analytically (black line) and numerically (blue dots) calculated decay rates in the diffusive regime for a carbon nanotube resonator. Here, $\epsilon E_0(0)/T_{\text{sim.}} = E_{\text{vib.}}/E_{\text{therm.}}$, $N = 1$, and $K = 1$.

I numerically investigated how the initial, linear decay rate changed when more than one vibrational mode was present; the result is shown in figure 6.8 (a). As the presence of adsorbed particles couple modes together, when there are more than a single mode present, energy can be transferred from the initially excited mode to initially frozen ones. This new path of energy transfer quantitatively increases the dissipation rate of resonator energy, but the qualitative behaviour of the ringdown is unchanged. Once the initially frozen modes are thermalized, the energy transferred in this way is dissipated through interaction with the particles. That is, each additional mode acts as a new dissipation channel, and consequently the actual linear dissipation rate increases proportionally to the number of modes. While the numerically determined α_1 for $N = 1$ seen in figure 6.8 (a) does not quite match the analytical expression (6.8), this latter estimation is clearly within the correct order of magnitude. Finally, since the number of modes N is arbitrarily large in a real system, there must be a cut-off value for the increase in dissipation with N; this value was estimated to 20 in paper I. However, as the equations (6.3)-(6.4) only follow from the Hamiltonian (6.1) for low-lying modes (see paper IV), any conclusions regarding the high-mode dynamics must be tentative.

When the resonator amplitude is no longer large enough to inertially trap the particles, these diffuse over the entire resonator and are best described in terms of their probability density function. In the single-mode approximation, equation (5.7) can be used to find the Fokker-Planck equation equivalent to (6.3)-(6.4), which is solved with a pertubative approach; details are found in paper I. To first order, the time evolution of the mean fundamental mode energy is given by

$$\langle E_0 \rangle(t) = \frac{E_0(0)}{1 + E_0(0)\beta_K t}, \tag{6.9}$$

where

$$\beta_K = 4T_{\text{sim.}} K \pi^4 \frac{1}{\gamma^2} \sum_j \frac{j^4 f_j^2}{\lambda_j^2 + 16}, \tag{6.10}$$

with $f_j = \int \mathrm{d}x \cos(j\pi x)\phi_0^2(x)$ and $\lambda_j = 2j^2\pi^2 T_{\text{sim.}}/\epsilon\gamma$. Including also second-order corrections will ensure that $\langle E_0 \rangle \to k_{\text{B}}T$ over long timescales. Figure 6.8 (b) shows that the analytical expression (6.9) well captures the actual decay rates found in simulations, when $N = 1$ also in the numerical integration. As shown in figure 6.9 (b), the number of modes included does not affect results in the diffusive regime, in contrast to in the trapped regime. Similarly, where in the trapped regime only the total added mass matters, in the diffusive regime the microscopic details of how that mass is distributed among adsorbates also play a role. This fact is indicated by the presence of the single-particle friction coefficient γ in equation (6.10). Simulation revealed that β_K scales as Km^2; see figure 6.9 (a).

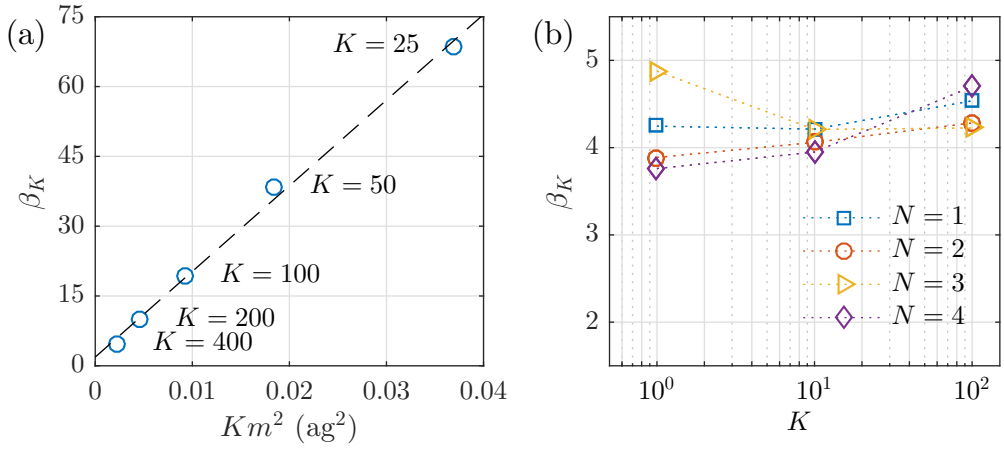

Figure 6.9: (a) Diffusive regime dissipation rates β_K for different numbers of particles K, where the total adsorbed mass Km is kept constant. (b) Decay rates β_K in the diffusive regime for different numbers of modes N and particles K, with Km^2 constant.

6.2.3 Diffusion-induced intermode dynamics

The presence of adsorbed particles couples resonator modes together, evidenced by the N-dependent dissipation rate of figure 6.8 (a). As I here model the vibrational modes of a carbon nanotube resonator as linear, there are no strong internal resonances, and the diffusion-induced mode coupling only acts to transfer energy in the manner discussed above. One example of the process is shown in figure 6.10; initially frozen modes thermalize rapidly and, apart from what might be a slight initial overshoot, their energies remain fluctuating around the thermal energy until the system reaches thermal equilibrium.

In contrast, in a graphene membrane, degenerate modes are present by symmetry. The energy transfer between these can be very efficient, enabling more complex ringdown dynamics. An example is shown in figure 6.11, where a graphene membrane was initialized in a superposition of the two degenerate first excited modes (indexed by 1^+ and 1^-). Then, for a short time in the beginning of the free evolution of the membrane, large amounts of energy is traded between the two degenerate modes while the total resonator energy remains almost constant. This low-dissipation region is then followed by a sharp drop in total energy, that levels into a second plateau when the fundamental mode is sufficiently excited to dominate the dynamics. At this point the relaxation proceeds as in section 6.2.2. This ringdown is reminiscent of the stepwise relaxation discussed in section 6.1, as well as of the mode coupling-induced anomalous dissipation seen in references [182] and [183].

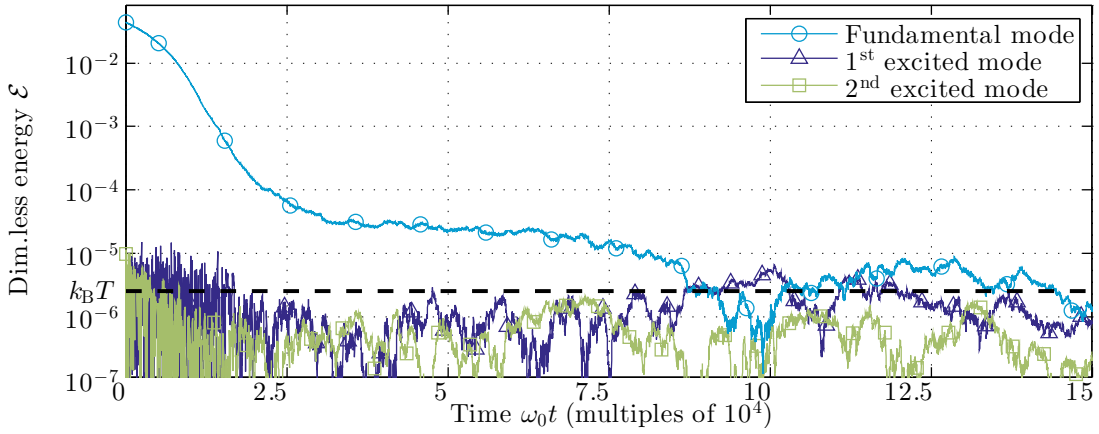

Figure 6.10: Relaxation to thermal equilibrium of a carbon nanotube resonator with an adsorbed Brownian particle (fundamental mode curve the same as in figure 6.5).

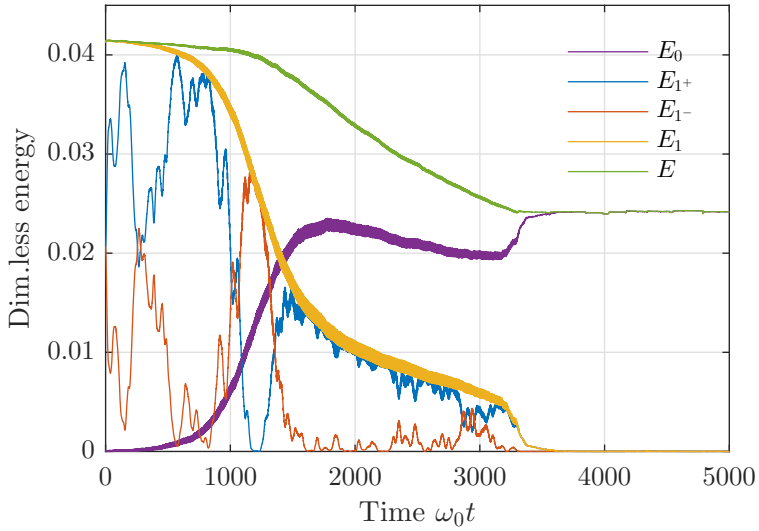

Figure 6.11: Initial ringdown of a graphene resonator, with large mode coupling and stepwise relaxation reminiscent of figure 6.1. Once the fundamental mode has come to dominate the resonator motion, the relaxation proceeds as discussed in section 6.2.2. Here, $E_1 = E_{1+} + E_{1-}$ and $E = E_0 + E_1$.

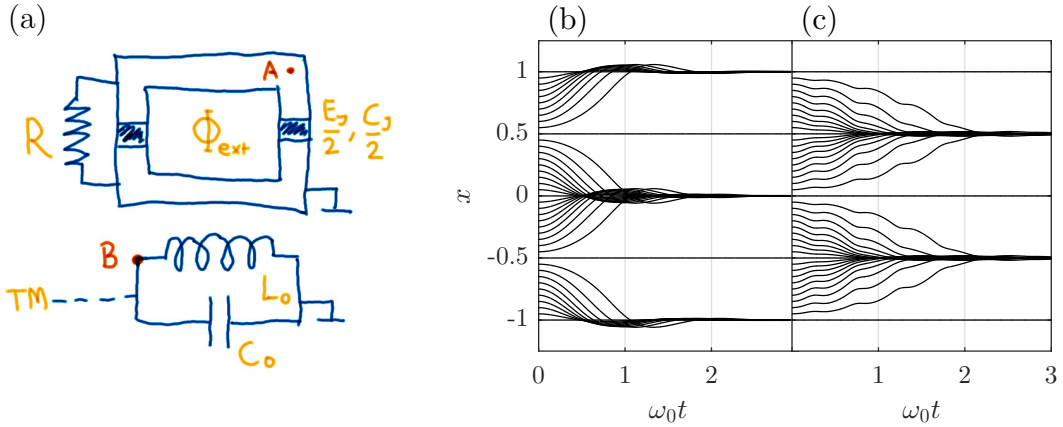

Figure 6.12: (a) Superconducting circuit realization of a diffusion-resonator system; a symmetric SQUID is inductively coupled to an LC-resonator. For read-out and actuation, the LC-resonator can be coupled inductively or capacitively to an external transmission line (TM). The nodes A and B indicate where the node fluxes used below as dynamic variables are defined. (b)-(c) Numerical integration of the full equations of motion, absent external drive and noise ($f(\tau) = 0$, $\gamma = 0$, $\eta = 0$, and $\mathcal{D} = 0$). The phase of the SQUID is rapidly trapped at integer (b) or half-integer (c) values of x, depending on resonator amplitude; $q(0) = 0.45$ in (b) and 3.65 in (c).

6.3 Superconducting LC-circuit coupled to a SQUID

A superconducting LC-resonator inductively coupled to a SQUID can be described in terms of the node fluxes $\Phi_{\mathrm{A,B}}(t) = \int_{-\infty}^{t} \mathrm{d}t'\, V_{\mathrm{A,B}}(t')$ at points A and B [194], indicated in the system sketch in figure 6.12 (a). The Lagrangian of this system is

$$L = \frac{1}{2} C_0 \dot{\Phi}_{\mathrm{B}}^2 - \frac{1}{2} \frac{\Phi_{\mathrm{B}}^2}{L_0} + \frac{1}{2} C_{\mathrm{J}} \dot{\Phi}_{\mathrm{A}}^2 - E_{\mathrm{J}} \cos \frac{\pi \Phi_{\mathrm{ext}}}{\Phi_0} \left(1 - \cos \frac{2\pi \Phi_{\mathrm{A}}}{\Phi_0} \right), \tag{6.11}$$

where C_0 (L_0) is the capacitance (inductance) of the LC-resonator, and $C_{\mathrm{J}}/2$ ($E_{\mathrm{J}}/2$) is the capacitance (Josephson energy) of each Josephson junction in the symmetric SQUID. The last term, proportional to E_{J}, is the potential energy of a SQUID: equation (4.6). When there is no applied field or other external sources of flux, $\Phi_{\mathrm{ext.}}$ is determined by the current through the resonator. To lowest order, then, $\Phi_{\mathrm{ext.}} \approx 2g\Phi_{\mathrm{B}}$.

Variation of the Lagrangian leads to the equations of motion

$$\ddot{q} + \gamma\dot{q} + q - \epsilon \sin q\,(1 - \cos 2\pi x) = F_0 \cos \Omega t \tag{6.12}$$

$$\ddot{x} + \eta\dot{x} + \alpha \cos q \sin 2\pi x = \eta\sqrt{\mathcal{D}}\xi(\tau). \tag{6.13}$$

where dimensionless variables $q = 2\pi g \Phi_{\mathrm{B}}/\Phi_0$ and $x = \Phi_{\mathrm{A}}/\Phi_0$ were defined; $\omega_0 \equiv 1$. A dissipation term and a harmonic driving force have been included in equation (6.12), whereas damping and noise according to the resistively and capacitively shunted Josephson junction-model [195,196] has been added to equation (6.13). In paper III, I studied this description of a superconducting resonator-Brownian motion system; I refer to that paper for algebraic details, and definitions and values of the dimensionless coefficients.

For $|q| \ll 1$, identifying $\phi(x) = \sqrt{2}\sin \pi x$, equations (6.12)-(6.13) almost reduce to the $N = 1$, $K = 1$-case of equations (6.3)-(6.4). The only difference is that the "particle" described by x now moves in a potential $\propto \phi^2(x)$, in addition to the q-dependent potential induced by the resonator. Hence, many of the results for the nanomechanical system carry over to this superconducting circuit. For experimental relevance, I consider the driven response of this circuit, instead of the ringdown studied in sections 6.1 and 6.2.

6.3.1 The superconducting phase as a classical two-level system

When the LC-resonator is driven, its amplitude q will be high in the sense of section 6.2, and the system dynamics will be analogous to the trapped regime of the nanomechanical system of that section. In particular, the superconducting phase x will be driven towards a trapped position. The trapped values $x_{\mathrm{eq.}}$ are given by the vanishing of the supercurrent (4.5) through the SQUID; in the present variables, $I_{\mathrm{s}} = I_{\mathrm{c}} \cos q \sin 2\pi x$. Hence, $x_{\mathrm{eq.}} = n/2$, $n \in \mathbb{Z}$.

It turns out that whether the SQUID phase is trapped at an integer or a half-integer value depends on the amplitude of the resonator; see figure 6.12 (b)-(c). The reason for this is clear from equation (6.13). The full potential that x moves in is proportional to $\cos q \sin^2 \pi x$, so its sign is completely determined by the value of q. When q is in the interval $[-\pi/2, \pi/2]$, $\cos q$ is positive and the potential minima are at integer x. For $q \in [\pi/2, 3\pi/2]$, the potential flips upside down so that its minima move to half-integer x. These intervals match those in figure 6.13 (a), where smearing due to the very shallow potential near $q = \pi/2, 3\pi/2$ can also be seen. This inversion of stable and unstable points is not entirely unexpected, considering the Kapitza-like structure of equation (6.13); compare with equation (2.8) and discussion thereof.

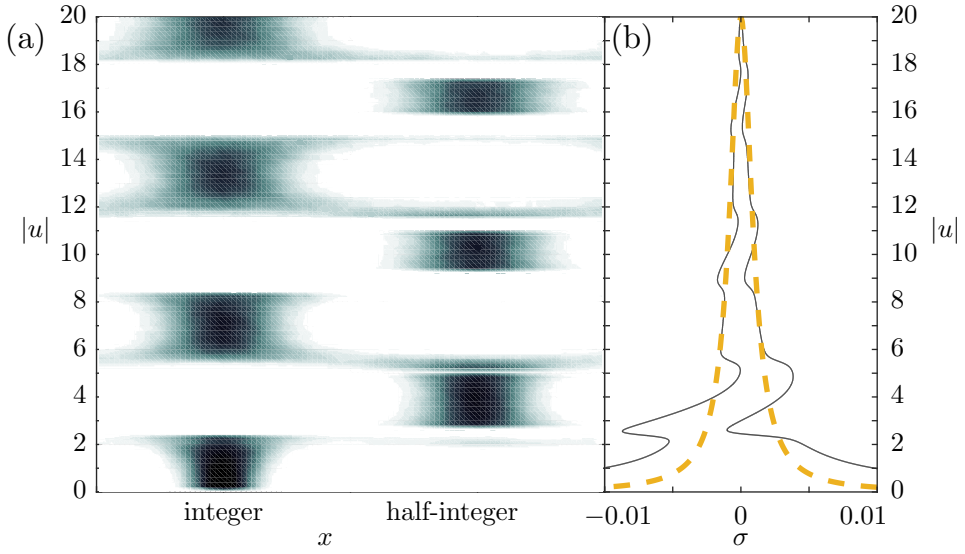

Figure 6.13: (a) Distribution of the SQUID phase x (mapped to the interval $[-\frac{1}{4}, \frac{3}{4}]$) as a function of resonator amplitude envelope $|u|$ (defined through equation (6.14)). The gaps in the distribution occur where the slope of the resonance curve is infinite, and no stable state could be found. (b) Theoretical response curve (solid black line) for $F_0 = 0.02$ and $\alpha/\pi\eta\mathcal{D} = 25$ together with the unperturbed Lorentzian response (yellow dashed line). When x is an integer, the resonator decouples from the SQUID, and the resonator response is very close to the Lorentzian. For half-integer x, the magnitude of the coupling to the SQUID is maximized, and the resonator response is highly non-linear.

Figure 6.12 (b)-(c) shows that the process of trapping is very quick, and figure 6.13 (a) illustrates rapid switching of x as a function of q. Additionally, the periodicity of equations (6.12)-(6.13) means that for the system dynamics, only whether x is close to an integer or a half-integer value matters, not the exact value of n. In this sense, the SQUID phase x of this system can be considered a classical two-level system.

As such, my results in paper III could be the first steps down a new avenue of studying the *classical* limit of Jaynes-Cummings systems; compare with section 4.2. Since this is a classical system, there is not an obvious parallel to electromagnetic quanta being absorbed and emitted by an atom that, as a consequence, switches between levels. However, it is suggestive that the state of the SQUID is completely determined by the amplitude of the electromagnetic field in the LC-resonator, and flips between two possible states as the field continuously changes.

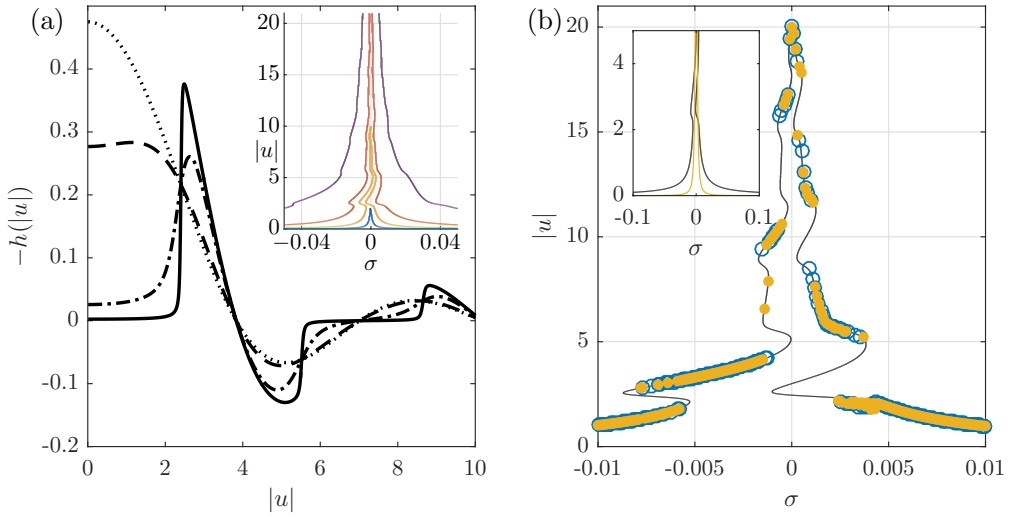

Figure 6.14: (a) Frequency shift $h(|u|)$ as function of amplitude $|u|$ for $\alpha/\pi\eta\mathcal{D} = 0.1$ (dotted curve), 1 (dashed curve), 10 (dash-dotted curve) and 100 (solid curve). The inset shows how the frequency response curves vary with driving force, for $\alpha/\pi\eta\mathcal{D} = 25$ and $F_0 = 0.002$ (blue curve), 0.01 (yellow curve), 0.04 (red curve), and 0.2 (purple curve). For moderate drive amplitudes, the frequency response can be multistable. (b) Simulated resonant response of the circuit as the drive frequency is swept up (yellow dots) and down (blue circles), with $F_0 = 0.02$, and $\alpha/\pi\eta\mathcal{D} = 25$; the agreement with the analytical black curve is excellent. The inset shows the broadening induced by the coupling to the SQUID; the response of the full system (black) compared with the Lorentzian response of an unperturbed LC-resonator (yellow).

6.3.2 Noise-tunable resonator nonlinearity

It is evident from equation (6.12) that the cases of integer and half-integer $x_{\text{eq.}}$ correspond to very different resonator dynamics. If the SQUID phase fluctuates around integer $x_{\text{eq.}}$, the ϵ-term in equation (6.12) fluctuates around zero, and the coupling between SQUID and resonator is very weak. Consequently, the resonator response to driving is linear. If, on the other hand, $x_{\text{eq.}}$ is a half-integer, equation (6.12) approaches the highly nonlinear Holweck-Lejay pendulum (2.10). As the $x_{\text{eq.}}$ depends on the resonator amplitude, during a single sweep across the resonant frequency the resonator response alternates between linear and nonlinear regimes, as shown in figure 6.13 (b).

The resonant response to driving – the black line in figure 6.13 (b) – was analytically calculated in the rotating wave approximation. The slow-moving envelope

$|u|$ of the resonator oscillation was defined through

$$q = \tfrac{1}{2}(ue^{i\Omega t} + u^* e^{-i\Omega t}), \quad \dot{q} = \tfrac{i}{2}\Omega(ue^{i\Omega t} - u^* e^{-i\Omega t}), \tag{6.14}$$

and rapidly oscillating terms in the equations of motion were discarded. The stationary probability distribution of x was found from the equivalent Fokker-Planck equation, and was used to replace the factor $(1-\cos 2\pi x)$ in equation (6.12) with a mean-field value. The result is that the steady-state value of $|u|$ when the circuit is driven is given by the transcendental equation

$$|u|^2 \left[\frac{\gamma^2}{4} + [\sigma - \epsilon h(|u|)]^2\right] = \frac{F_0^2}{4}. \tag{6.15}$$

Here, the detuning $\sigma = \Omega - 1$ is assumed to be small, and the frequency shift is given by

$$h(|u|) = \frac{J_1(|u|)}{|u|}\left[\frac{I_1\left(J_0(|u|)\frac{\alpha}{\pi\eta\mathcal{D}}\right)}{I_0\left(J_0(|u|)\frac{\alpha}{\pi\eta\mathcal{D}}\right)} - 1\right] \tag{6.16}$$

where $(I_{0,1})$ $J_{0,1}$ are (modified) Bessel functions of the first kind [197]. The frequency shift (6.16) as a function of amplitude $|u|$ is shown in figure 6.14 (a). Self-consistently solving equation (6.15) gives the resonant response of the LC-resonator to a periodic drive: the black line in figure 6.13 (b). See also the inset of figure 6.14 (a).

Where the qualitative behaviour of the nanomechanical system was determined by the ratio $E_{\text{vib.}}/E_{\text{therm.}}$, it is clear from equations (6.15)-(6.16) that the dynamics of the superconducting circuit is set by $\alpha/\pi\eta\mathcal{D} = 2\pi E_{\text{J}}/k_{\text{B}}T$. In the former case, I considered ringdown dynamics, whereas in the present case, I study the driven steady state. Despite this, it is striking that both these resonator-Brownian motion systems reduce to a single determining parameter: a ratio between the thermal energy and the characteristic energy of the Brownian subsystem.

As can be seen in figure 6.14 (a), as the level of noise in the system (that is, the size of $\mathcal{D}$) decreases, the frequency shift becomes less smooth, to the point where it switches between regions where $h(|u|) \approx 0$ and highly nonlinear regions in an almost discontinuous manner. The sharper the frequency shift, the more pronounced will the anomalous, flame-like frequency response be. Hence, the noise level can be used to tune the nonlinearity of this superconducting circuit. As more noise means a smoother, more well-behaved response, this system may be an example of the kind of helpful randomness I discussed in section 5.2.

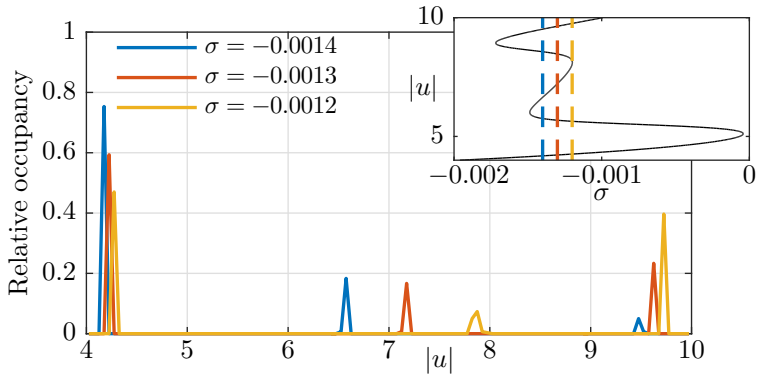

Figure 6.15: Distribution of resonator amplitudes for three values of the detuning σ. The inset shows a close-up of the relevant region of the analytical resonance curve, where the dashed lines indicate the examined values of σ. The tristability of the analytical response curve is reflected in the three possible steady states found.

6.3.3 Multistable frequency response

It is clear in figure 6.14 (b) that, in this circuit, the analytically calculated frequency response implies that multistability beyond bistability is possible. However, the finite temperature of the simulation means that many of the potential hysteresis loops of the driven response are smeared; there is little difference between frequency sweeps up and down as calculated with the full, stochastic equations of motion (6.12)-(6.13).

In order to determine if the possibility for multistability is real, or an artefact of the approximations made in arriving at equation (6.15), the time evolution of equations (6.12)-(6.13), with σ chosen in a theoretically tristable region, was simulated several hundred times, with random initial conditions. For each trajectory, the final steady state amplitude was recorded; the distribution of these amplitudes is shown in figure 6.15. Evidently, multistability is possible also in the full equations of motion (6.12)-(6.13). While there is likely to be some correlation between initial and final states, as shown in figure 6.16, even if the initial state of the system is the same apart from small variations in $q(0)$, its time evolution can sample all three stable steady states. Figure 6.16 also illustrates, once more, that the amplitude of the resonator determines the state of the SQUID phase, and, like other two-level systems, the phase switches very rapidly between the two $x_{\text{eq.}}$.

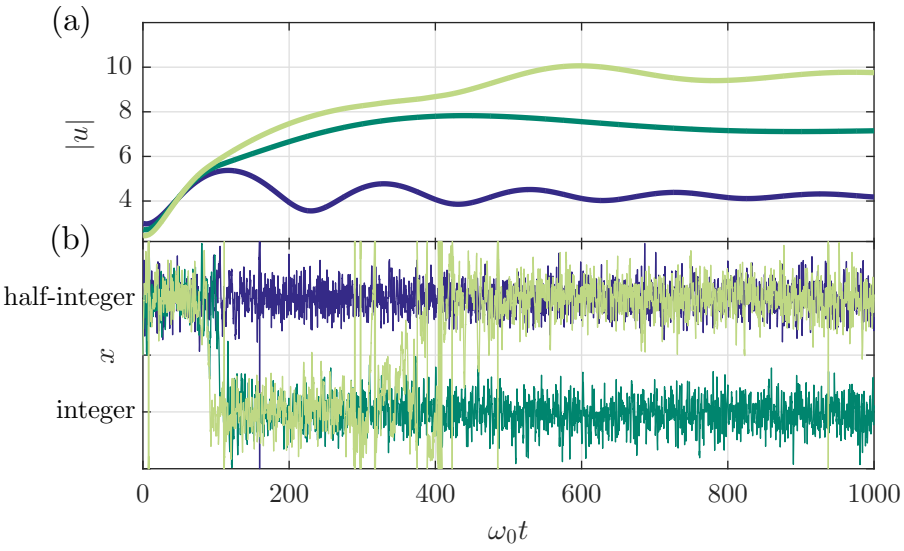

Figure 6.16: (a) Three examples of the time evolution of $|u|$ for $\sigma = -0.0013$. Despite quite small variations in the initial conditions, the system eventually settles in very different states. (b) The corresponding time evolutions of x. In each case, the SQUID phase is initially trapped at a half-integer value. The subsequent evolution of $x_{\text{eq.}}$ is dictated by the resonator amplitude $|u|$, in agreement with figure 6.13 (a)

6.4 Summary

I have studied harmonic oscillators coupled to auxiliary systems, primarily auxiliary Brownian systems.

In paper IV and section 6.1, the nonlinearity of a set of oscillators coupled to free particles was illustrated by a minimal model without noise. The action-back action interplay between particles and oscillators creates unpredictable particle dynamics, switching between trapped, regular oscillations, and untrapped, possibly chaotic motion. The trapping-retrapping dynamics of the particle corresponds to switching between high and low dissipation of oscillator energy, leading to an unusual, stepwise relaxation.

One physical realization of resonator-Brownian motion systems is particles adsorbed on the surface of nanomechanical resonators. This kind of system appears in mass sensing experiments, and can also be relevant to nanomechanical resonators operated in ambient conditions, exposed to air molecules and floating nanoparticles. There is also recent experimental interest in the diffusion of ^{4}He on carbon nanotube and graphene resonators. I have studied ensembles of particles on one- and twodimensional multimode resonators in papers I, II, and IV, and summarized some results in section 6.2. In particular, the ringdown of the res-

onator has been characterized and described, in the two regimes of high and low $E_{\text{vib.}}/E_{\text{therm.}}$: particle vibrational energy over thermal energy. The two regimes correspond to trapped and freely diffusing particle dynamics, with qualitatively different resonator ringdown behaviour. The ringdown is never exponential, and, if degenerate modes are present, there are indications of a stepwise relaxation also in this system. This part of my work functions as a record of possible diffusion-induced ringdown effects, and, as such, could prove useful in the future when nanomechanics experiments in ambient conditions becomes commonplace.

Finally, in paper III and section 6.3, I considered a realization of a resonator-Brownian motion system that is straightforward to fabricate: a superconducting LC-resonator coupled to a SQUID. I have showed that the circuit's resonant response to driving is highly nonlinear and multistable. The level of noise tunes the resonator from linear to nonlinear and back, determined by the ratio between the Josephson energy and the thermal energy: $E_{\text{J}}/E_{\text{therm.}}$. My results in this paper are well within reach of experimental verification.

7 Outlook

The subsystems I consider – the harmonic oscillator and Brownian motion – are, I emphasize again, very general and can model a wide range of physical systems. Counting the one discussed in appendix B, this thesis discusses three quite disparate realizations: one nanomechanical, one optomechanical, and one superconducting. Together, these three systems represent a significant fraction of the field of condensed matter physics. As such, my work can be continued in a myriad of directions.

Experimentally, my work in paper III was designed to facilitate reproduction. Fabricating and studying this superconducting resonator-Brownian motion circuit is a natural next step for the work discussed in this thesis. Another aspect of the superconducting circuit is that noise can be *injected*. One is thus not confined to the Gaussian thermal noise I studied; both the level and the distribution of noise can be customized and closely controlled.

Theoretically, relaxing some of the constraints and approximations used in my work leads to a number of possible smaller projects. For instance, the requirement that particles are noninteracting is likely not accurate when the number of particles becomes large. To take particle interactions and collisions into account, it is likely that one must turn to molecular dynamics or multiscale methods.

Another, more straightforward, generalization is to consider particles that are not identical. Then, parameters that depend on the particle mass must be replaced with indexed versions: ϵ_k, γ_k and D_k. While I do not believe that such a generalization will significantly alter the qualitative dynamics of the nanomechanical resonator-particles system, it can nonetheless be a worthwhile study. For instance, experiments in ambient conditions can be modelled using one or a few heavy adsorbates, and a large number of light ones that represent air molecules. In this vein, it is also straightforward to expand my work to take adsorption- and desorption-events into account.

One interesting avenue for further study, that is likely to connect the results of the four papers even closer, is the ringdown dynamics of a higher mode. My work in papers I and II assumed that it was the fundamental resonator mode that was initially excited. The fundamental mode only has a single antinode, but if a

higher mode is dominant, the inertial potential will have several minima. As long as the particles are closely trapped to a single antinode, the analysis of section 6.2 does not qualitatively depend on the exact mode shape considered. However, even in the trapped regime, switching between the antinodes of a higher mode can be present, and will be present for long enough times. It seems probable that, at least in a transient state, this switching could trigger trapping-retrapping dynamics like those of paper IV. Possibly, the introduction of another timescale (the Kramers escape rate) could cause synchronization phenomena, including stochastic resonance. If the nanomechanical resonator is driven in a higher mode, there might be connections to the switching behaviour of the superconducting phase in paper III.

Finally, real nanomechanical resonators are almost exclusively modelled as Duffing resonators, a model that agrees well with experimental results. In order to connect to existing experimental and theoretical knowledge on Duffing systems, both driven and relaxing, the most relevant extension of my work is to include a cubic nonlinearity in the equations of motion. Considering the here presented dynamical richness that arises in a *linear* resonator coupled to diffusing degrees of freedom, it seems likely that also the Brownian motion-coupled *Duffing* resonator can be the topic of a whole thesis.

A Eigenmodes and -frequencies

Here, I derive the eigenmodes and eigenfrequecies for a doubly clamped beam and a circular, pinned membrane*.

In the case of a one-dimensional beam resonator of length L that is doubly clamped ($\varphi_n(0) = \varphi_n(L) = \varphi_n'(0) = \varphi_n'(L) = 0$), the now-ordinary differential equation (3.4) has the characteristic equation

$$\kappa k^4 - \sigma k^2 - \rho\omega_n^2 = 0. \tag{A.1}$$

Its roots are $\pm k_n^+, \pm i k_n^-$, where

$$k_n^\pm = \sqrt{\sqrt{\frac{\sigma^2}{4\kappa^2} + \frac{\rho\omega_n^2}{\kappa}} \pm \frac{\sigma}{2\kappa}}. \tag{A.2}$$

The general solution for each eigenfunction $\varphi_n(x)$ is thus

$$\varphi_n(x) = A_n \sinh k_n^+ x + A_n' \sin k_n^- x + B_n \cosh k_n^+ x + B_n' \cos k_n^- x, \tag{A.3}$$

where the integration constants will be chosen so that the φ_n are real and normalized to L:

$$\int_0^L \mathrm{d}x\ \varphi_m(x)\varphi_n(x) = L\delta_{mn}. \tag{A.4}$$

That the eigenfunctions are orthogonal is straight-forwardly verified; see, for example, reference [198].

The algebra involved in determining the $A_n^{(\prime)}, B_n^{(\prime)}$ and the eigenfrequencies ω_n turns out to be simplified by a change of variables to $\chi = x - L/2$. Then, the boundary conditions neatly divide the φ_n into sets of even and odd functions:

$$\begin{aligned} \varphi_n(\chi) &= A_n \cosh k_n^+ \chi + A_n' \cos k_n^- \chi, \quad n = 0, 2, 4, \ldots, \\ \varphi_n(\chi) &= B_n \sinh k_n^+ \chi + B_n' \sin k_n^- \chi, \quad n = 1, 3, 5, \ldots. \end{aligned} \tag{A.5}$$

*This appendix was originally published as a section in [87].

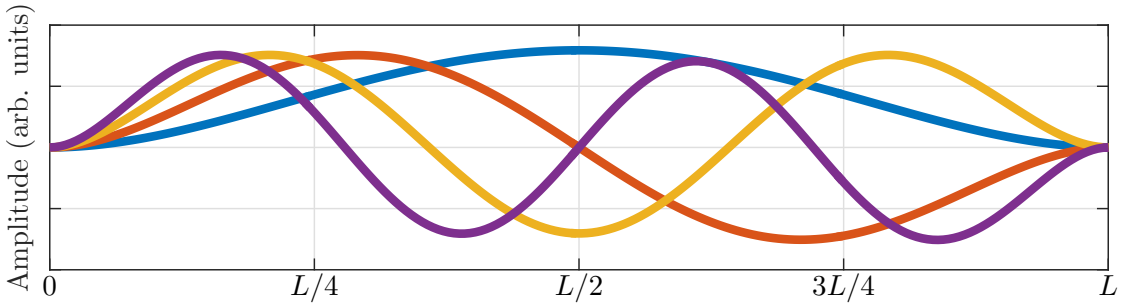

Figure A.1: Flexural eigenmodes of a doubly clamped beam of length L.

The eigenfrequencies ω_n are determined from the equation

$$\frac{k_n^{\mp}}{k_n^{\pm}} = \pm \frac{\tan k_n^- L/2}{\tanh k_n^+ L/2}, \tag{A.6}$$

where upper (lower) signs correspond to odd (even) n. While the value of the frequencies depend on material parameters, the ratio between them is only a function of the resonator geometry. Table A.1 lists the ratio ω_n/ω_0 for some excited mode; ω_0 denotes the fundamental mode frequency. A quick estimate is given by $\omega_n/\omega_0 \approx \frac{1}{9}(2n+1)^2$.

Finally, the integration constants $A_n^{(\prime)}$ and $B_n^{(\prime)}$ are found from the boundary conditions combined with the normalization chosen in (A.4). The result is that

$$A_n' = -\frac{\cosh k_n^+ \frac{L}{2}}{\cos k_n^- \frac{L}{2}} A_n, \quad B_n' = -\frac{\sinh k_n^+ \frac{L}{2}}{\sin k_n^- \frac{L}{2}} B_n \tag{A.7}$$

and

$$\begin{aligned} |A_n|^2 &= 2\left[1 + \frac{\sinh k_n^+ L}{k_n^+ L} + \frac{\cosh^2 k_n^+ \frac{L}{2}}{\cos^2 k_n^- \frac{L}{2}} \left(1 + \frac{\sin k_n^- L}{k_n^- L}\right)\right]^{-1}, \\ |B_n|^2 &= 2\left[1 - \frac{\sinh k_n^+ L}{k_n^+ L} - \frac{\sinh^2 k_n^+ \frac{L}{2}}{\sin^2 k_n^- \frac{L}{2}} \left(1 - \frac{\sin k_n^- L}{k_n^- L}\right)\right]^{-1}. \end{aligned} \tag{A.8}$$

The final undetermined phase is chosen so that the φ_n are real.

While the expressions for the eigenmodes may look complicated, the mode shapes can be thought of as sines and cosines that have been somewhat deformed in order to fit the doubly clamped boundary conditions. The four lowest vibrational modes are shown in figure A.1.

Table A.1: Normalized eigenfrequency ω_n/ω_0 for the n:th excited mode of a beam and a membrane resonator, where ω_0 is the fundamental mode frequency (corresponding to $(\mu,\nu) = (0,1)$ for the membrane). For the beam resonator, a good approximation for the ratio ω_n/ω_0 is $\frac{1}{9}(2n+1)^2$, while for the membrane $\omega_n/\omega_0 \approx \frac{6}{5}\sqrt{n}$. Note also the two-fold degeneracy of many of the membrane excited modes.

n	Beam	Membrane	(μ,ν)
1	2.7245	1.5933	$(\pm1,1)$
2	5.3139	2.1355	$(\pm2,1)$
3	8.7633	2.2954	$(0,2)$
4	13.074	2.6531	$(\pm3,1)$
5	18.246	2.9173	$(\pm1,2)$
6	24.280	3.1555	$(\pm4,1)$
7	31.176	3.5001	$(\pm2,2)$

In the case of a two-dimensional membrane with vanishing thickness, the bending rigidity κ is negligibly small [199]. Then, (3.4) becomes the Helmholtz equation

$$\nabla^2\varphi_n = -\frac{\omega_n^2\rho}{\sigma}\varphi_n, \tag{A.9}$$

with the known [197] solutions

$$\varphi_n(r,\theta) = A_n e^{i\mu\theta} J_{|\mu|}\left(r\omega_n\sqrt{\frac{\rho}{\sigma}}\right). \tag{A.10}$$

Here, $\mu \in \mathbb{Z}$ and $J_{|\mu|}$ are Bessel functions of the first kind. All eigenmodes with $\mu \neq 0$ are doubly degenerate.

The boundary condition that $\varphi_n(R,\theta) = 0$ fixes the eigenfrequencies as

$$\omega_n = \frac{\alpha_{|\mu|\nu}}{R}\sqrt{\frac{\sigma}{\rho}}, \tag{A.11}$$

where $\alpha_{\mu\nu}$ is the ν:th zero of J_μ. The index n must now be interpreted as a vector index $n = (\mu,\nu)$. Again, the ratio between eigenfrequencies depends only on the resonator geometry: some of the normalized excited mode frequencies are listed in table A.1. A quick estimate of the frequency ratio is $\omega_n/\omega_0 \approx \frac{6}{5}\sqrt{n}$.

The membrane eigenfunctions are orthogonal by construction, and the normal-

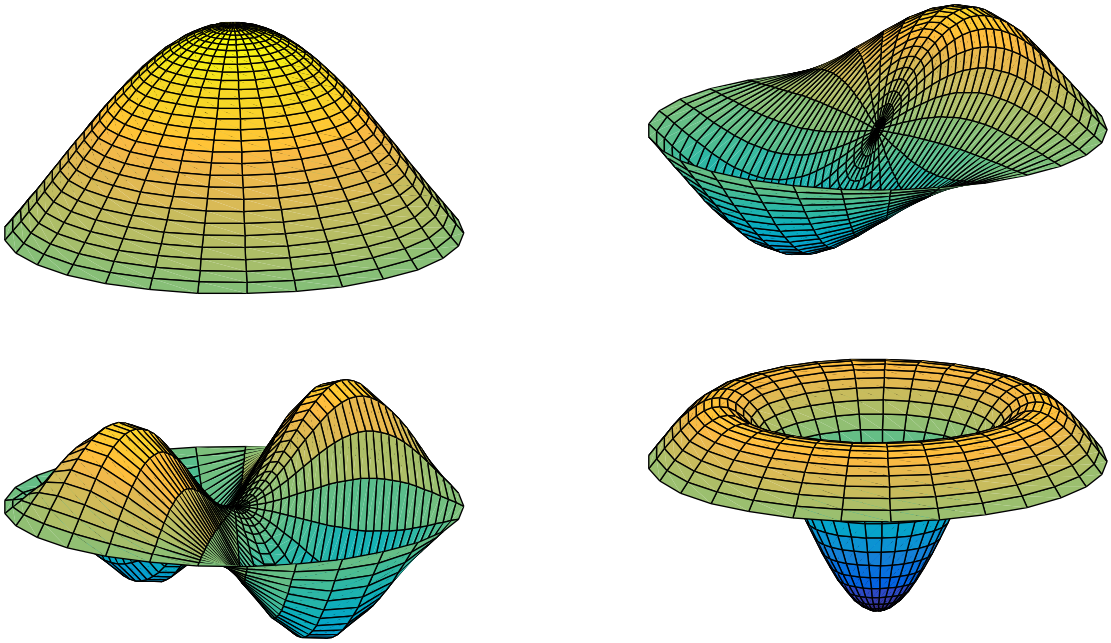

Figure A.2: Flexural eigenmodes of a circular membrane. Those excited modes that are not rotationally symmetric are degenerate; there is a second eigenmode with the same frequency but with a phase difference of $\pi/2$.

ization is chosen so that

$$\int_0^{2\pi} \mathrm{d}\theta \int_0^R r\mathrm{d}r \; \varphi_n^*(r,\theta)\varphi_m(r,\theta) = \pi R^2 \delta_{mn} \tag{A.12}$$

by setting

$$A_n = \left[J_{|\mu|+1}\left(\omega_n \sqrt{\frac{\rho}{\sigma}} R \right) \right]^{-1} = \left[J_{|\mu|+1}\left(\alpha_{|\mu|\nu} \right) \right]^{-1}. \tag{A.13}$$

The shape of the four lowest vibrational modes is shown in figure A.2.

B Optomechanical analogous system

When considering ways to realize a resonator-Brownian motion system different from the nanomechanical one discussed in section 6.2, the first one I studied was an optomechanical [200] system: a levitated dielectric sphere in an optical cavity [201], sketched in figure B.1. The sphere is trapped in a harmonic potential using optical tweezers [202]. By levitating the particle, interactions with a thermal environment are minimized, enabling cooling to the quantum ground state in a room temperature [203] environment and, possibly, quantum superposition of bacteria-sized objects [204].

Conceptually, as this system contains a particle, whose position can be allowed to stochastically vary, interacting with a harmonic mode, there are clear similarities to a single particle on a nanomechanical resonator. It is also possible to levitate the sphere using a multimode optical cavity [205], in which case a separate optical tweezer is not necessary, and the conceptual likeness increases further. For simplicity, I here consider a separate trap and only a single cavity mode.

In this appendix, I show that the classical limit of the levitated sphere in an optical cavity does indeed obey equations of motions analogous to the ones discussed in chapter 6. However, the frequency mismatch between the optical and the mechanical frequency is very large, so the parametric component of the sphere motion becomes weak. Thus, the anomalous coupled dynamics is very unlikely to be detectable. For this reason, study of this system was not pursued further.

The levitated sphere in an optical cavity is described by the Hamiltonian [206]

$$H = \hbar\omega_{\mathrm{c}} a^\dagger a + \frac{p}{2m} + \tfrac{1}{2} m\omega_{\mathrm{t}}^2 x^2 + \tfrac{1}{2}\hbar g \sin^2\left(\tfrac{\omega_{\mathrm{c}}}{c}x + \tfrac{\pi}{4}\right)\left(a + a^\dagger\right)^2, \qquad \text{(B.1)}$$

where ω_{c} is the frequency of the optical cavity mode, c the speed of light, the optical mode creation (annihilation) operator is $a^\dagger$ (a), the sphere has mass m and center-of-mass position (momentum) x (p), ω_{t} is the frequency of the optical tweezer trap, and g is a coupling constant.

The time evolution of the mean values of the operators in equation (B.1) is

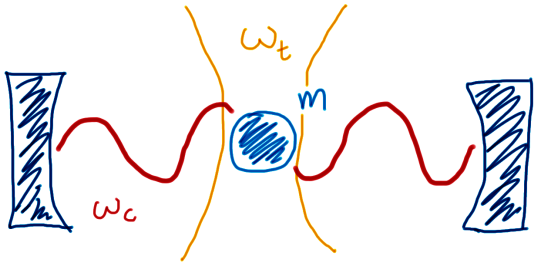

Figure B.1: A dielectric sphere with mass m, levitated by optical tweezers with frequency ω_t inside an optical cavity with frequency ω_c.

given by $\mathrm{d}\langle\,\cdot\,\rangle/\mathrm{d}t = i\hbar^{-1}[H,\,\cdot\,]$, where the brackets signify commutation with the Hamiltonian. With the notational redefinitions $\langle a\rangle \to a$, $\langle a^\dagger\rangle \to a^*$, $\langle x\rangle \to x$, and $\langle p\rangle \to p$, the equations of motion for the mean values are

$$\begin{aligned}
\dot{a} &= -i\omega_\mathrm{c} a - ig\sin^2\left(\tfrac{\omega_\mathrm{c}}{c}x + \tfrac{\pi}{4}\right)(a + a^*) \\
\dot{a}^* &= i\omega_\mathrm{c} a^* + ig\sin^2\left(\tfrac{\omega_\mathrm{c}}{c}x + \tfrac{\pi}{4}\right)(a + a^*) \\
\dot{x} &= p/m \\
\dot{p} &= -m\omega_\mathrm{t}^2 x - \frac{\omega_\mathrm{c}}{c} g\sin\left(\tfrac{\omega_\mathrm{c}}{c}x + \tfrac{\pi}{4}\right)\cos\left(\tfrac{\omega_\mathrm{c}}{c}x + \tfrac{\pi}{4}\right)(a + a^*)^2 .
\end{aligned} \tag{B.2}$$

In analogy with (6.14), the mode amplitude $q = a + a^*$ and velocity $v = i\,(a - a^*)$ are defined. Note that $\dot{q} = \dot{a} + \dot{a}^* = -\omega_\mathrm{c} v$ and

$$\dot{v} = i\,(\dot{a} - \dot{a}^*) = \omega_\mathrm{c} q + 2\sin^2\left(\tfrac{\omega_\mathrm{c}}{c}x + \tfrac{\pi}{4}\right) q. \tag{B.3}$$

It follows that, defining $\phi(x) = \sqrt{2}\sin\left(\frac{\omega_\mathrm{c}}{c}x + \frac{\pi}{4}\right)$, equations (B.2) can be written

$$\begin{aligned}
\ddot{q} &= -\omega_\mathrm{c}^2 q + g\omega_\mathrm{c}\phi^2(x) q \\
\ddot{x} &= -\omega_\mathrm{t}^2 x - \tfrac{1}{2} g m^{-1} q^2 \partial_x \phi^2(x).
\end{aligned} \tag{B.4}$$

In order to include thermal fluctuations in x, damping and diffusion terms can now be introduced by hand.

Equations (B.4) are clearly the single-mode version of equations (6.2), with the addition of an external harmonic potential that the sphere moves in. They are also equivalent to the limit when $q, x \ll 1$ of equations (6.12)-(6.13).

C Integration algorithm details

To numerically integrate the stochastic differential equations (SDEs) that appear throughout my work, the second-order algorithm proposed in [191–193] was used. It deals with SDEs of the form

$$\dot{x}_i = f_i(\mathbf{x}) + g_i(\mathbf{x})\xi(t), \tag{C.1}$$

where $i = 1, \ldots, N$, $\mathbf{x} = (x_1, \ldots, x_N)$; $\mathbf{f}$ and $\mathbf{g}$ are defined analogously. The stochastic force $\xi_i(t)$ is Gaussian, characterized by $\langle \xi(t) \rangle = 0$ and, here, $\langle \xi(s)\xi(t) \rangle = \delta(s - t)$. See references [191–193] for the extension to coloured noise.

In equation (C.1) there is a single source of noise, that acts differently on the different coordinates through $\mathbf{g}(\mathbf{x})$. It is not immediately obvious how an algorithm written for this type of SDE can be applied to the problem of two-dimensional diffusion, where $\xi(t) \to \xi_i(t)$. A generalization to several uncorrelated stochastic forces exists [191], but only to first order. Fortunately, for additive noise and the Langevin-like equations of motion considered in this thesis, this difficulty can be circumvented, as detailed below. The key is that, when rewritten to a set of first-order differential equations, the noise is in the equations for particle velocity. These velocity coordinates only appear in linear damping terms, leading to the vanishing of non-Gaussian terms; see equation (C.18) and discussion thereof.

Another complication that appeared in my work is that if one naïvely makes a change from Cartesian coordinates to polar coordinates in the SDE, it appears as if the additive Cartesian noise has been transformed into multiplicative polar noise: clearly not something that is physically sound. By instead making the change of variables in the expressions for numerically integrating the SDE over a timestep, this issue is avoided.

C.1 Two-dimensional diffusion

The equations of motion discussed in chapter 6 are of the form

$$\begin{aligned} \dot{q}_n &= p_n, & \dot{p}_n &= -\omega_n^2 q_n + \epsilon\, \partial_{q_n} \mathcal{U}(q_n, x, y), \\ \dot{x} &= u, & \dot{u} &= -\gamma u + \partial_x \mathcal{U}(q_n, x, y) + \gamma\sqrt{2D}\; \xi_x(t), \\ \dot{y} &= v, & \dot{v} &= -\gamma v + \partial_y \mathcal{U}(q_n, x, y) + \gamma\sqrt{2D}\; \xi_y(t), \end{aligned} \tag{C.2}$$

where $\xi_i(t)$, $i = x, y$ is Gaussian, with mean $\langle \xi_i(t) \rangle = 0$ and correlation function $\langle \xi_i(s)\xi_j(t) \rangle = \delta_{i,j}\delta(s-t)$. Equation (C.2) is cast in the form of equation (C.1) by identifying $\mathbf{x} = (q_1, p_1, \ldots, q_N, p_N, x, u, y, v)$, and $\mathbf{f}$ and $\mathbf{g}$ with the appropriate parts of the right-hand side of (C.2). The algorithm for numerical integration is derived by formally integrating the SDE over a short time period $[0, h]$:

$$x_i(h) - x_i(0) = \int_0^h f_i(x_1, \ldots, x_N)\mathrm{d}t + g_i \int_0^h \xi_i(t)\mathrm{d}t. \tag{C.3}$$

The f_i are Taylor expanded around zero, and the $\Delta x_i(t) = x_i(t) - x_i(0)$ that appear in this expansion are replaced by equation (C.3). By iterating this procedure, successively higher-order terms can be determined. However, I first discuss the stochastic (Stratonovich) integral in (C.3).

The integral over a stochastic process is itself a random variable. In order to numerically integrate systems like (C.2), the strategy is to find the distribution of $\int_0^h \xi_i(t)\mathrm{d}t$ (and any other random variables that arise by integration), and, at each time step, replace this integral with a random number generated from that distribution.

As the process $\xi_i(t)$ is Gaussian, any increment $\xi(t_n) - \xi(t_{n-1})$ is also normally distributed [127]. It follows that the integral

$$Z_1^{(i)}(h) \equiv \int_0^h \xi_i(t)\mathrm{d}t \tag{C.4}$$

is the sum over a large number of normal variables, making also $Z_1^{(i)}(h)$ a Gaussian variable. It is thus completely determined by its first two moments, which are straight-forwardly calculated:

$$\left\langle Z_1^{(i)}(h) \right\rangle = \int_0^h \langle \xi_i(t) \rangle \, \mathrm{d}t = 0, \tag{C.5}$$

and

$$\left\langle Z_1^{(i)}(h)Z_1^{(j)}(h)\right\rangle = \int_0^h \mathrm{d}t \int_0^h \langle \xi_i(t)\xi_j(s)\rangle \,\mathrm{d}s = \delta_{i,j}\int_0^h \mathrm{d}t \int_0^h \delta(t-s)\mathrm{d}s$$
$$= h\delta_{i,j}. \tag{C.6}$$

That is, $Z_1^{(i)}(h) \sim \mathcal{N}(0,h)$, and the $Z_1^{(i)}(h)$ that correspond to different stochastic forces (different values of i) are uncorrelated.

Time integrals of $Z_1^{(i)}(t)$ will also appear;

$$Z_2^{(i)}(h) \equiv \int_0^h Z_1^{(i)}(t)\mathrm{d}t = \int_0^h \mathrm{d}t \int_0^t \xi_i(s)\mathrm{d}s, \tag{C.7}$$

$$Z_3^{(ij)}(h) \equiv \int_0^h Z_1^{(i)}(t)Z_1^{(j)}(t)\mathrm{d}t = \int_0^h \mathrm{d}t \int_0^t \xi_j(s)\mathrm{d}s \int_0^t \xi_j(s')\mathrm{d}s'. \tag{C.8}$$

By the same argument as for $Z_1^{(i)}(h)$, $Z_2^{(i)}(h)$ is normally distributed. The relevant moments are $\left\langle Z_2^{(i)}(h)\right\rangle = 0$ and

$$\left\langle Z_1^{(i)}(h)Z_2^{(j)}(h)\right\rangle = \int_0^h \mathrm{d}t \int_0^h \mathrm{d}t' \int_0^{t'} \langle \xi_i(t)\xi_j(s)\rangle \,\mathrm{d}s = \delta_{i,j}\int_0^h \mathrm{d}t' \int_0^{t'} \mathrm{d}s$$
$$= \tfrac{1}{2}h^2\delta_{i,j}, \tag{C.9}$$

$$\left\langle Z_2^{(i)}(h)Z_2^{(j)}(h)\right\rangle = \int_0^h \mathrm{d}t \int_0^h \mathrm{d}t' \int_0^t \mathrm{d}s \int_0^{t'} \langle \xi_i(s)\xi_j(s')\rangle \,\mathrm{d}s'. \tag{C.10}$$

In order to evaluate the autocorrelator of $Z_2^{(i)}(h)$, the integral over t' is split into two parts: over the intervals $[0,t]$ and $[t,h]\cdot$ Considering the first of these intervals gives a contribution

$$\int_0^h \mathrm{d}t \int_0^t \mathrm{d}t' \int_0^{t'} \mathrm{d}s' \int_0^t \delta(s-s')\mathrm{d}s = \int_0^h \mathrm{d}t \int_0^t \mathrm{d}t' \int_0^{t'} \mathrm{d}s' = \frac{h^3}{6}. \tag{C.11}$$

To ensure that the integral over $\delta(s-s')$ in nonzero (that the point $s=s'$ exists in the integration interval), the integral over $s \in [0,t]$ was evaluated first; $s' \in [0,t'] \subset [0,t]$. By the same argument, in the second contribution over $t' \in [t,h]$, the s'-integral must be the first to be evaluated. That is,

$$\int_0^h \mathrm{d}t \int_t^h \mathrm{d}t' \int_0^t \mathrm{d}s \int_0^{t'} \delta(s-s')\mathrm{d}s' = \int_0^h \mathrm{d}t \int_t^h \mathrm{d}t' \int_0^t \mathrm{d}s = \frac{h^3}{6}, \tag{C.12}$$

leading to

$$\left\langle Z_2^{(i)}(h) Z_2^{(j)}(h) \right\rangle = \frac{h^3}{3}\delta_{i,j}. \tag{C.13}$$

With the moments of $Z_1^{(i)}(h)$ and $Z_2^{(i)}(h)$ found, it is easy to realize that the correct replacements in the numerical integration are

$$Z_1^{(i)}(h) \to h^{1/2} Y_1^{(i)}, \qquad Z_2^{(i)}(h) \to h^{3/2}\left[\tfrac{1}{2} Y_1^{(i)} + \tfrac{1}{2\sqrt{3}} Y_2^{(i)}\right], \tag{C.14}$$

where $Y_1^{(i)}$ and $Y_2^{(i)}$ are uncorrelated and normally distributed with mean zero and variance one.

The moments of the non-Gaussian [191] variable $Z_3^{(ij)}(h)$ are quite complicated alredy in the case of one-dimensional noise (when $i = j$), and have not, to my knowledge, been determined in the higher-dimensional case. Luckily, as shown below, all the $Z_3^{(ij)}(h)$-terms will vanish when the noise is additive and the integrated differential equation has the particular structure of (C.2).

With the stochastic integrals defined, the rest is algebra.

Expanding the f_i in equation (C.3) leads to

$$\Delta x_i(h) \approx g_i Z_1^{(i)}(h) + \int_0^h \mathrm{d}t \left[f_i(\mathbf{x}(0)) + f_{i,j}(\mathbf{x}(0))\Delta x_j(t) + \tfrac{1}{2} f_{i,jk}(\mathbf{x}(0))\Delta x_j(t)\Delta x_k(t) \right], \tag{C.15}$$

where $f_{i,j} \equiv \partial f_i / \partial x_j$, and analogously for $f_{i,jk}$. Summation over repeated indicies is implied. For brevity, the argument of the f_i and its derivatives will henceforth be omitted.

The integration over the constant term in the expansion can be performed, leading to

$$\Delta x_i(h) \approx g_i Z_1^{(i)}(h) + f_i h, \tag{C.16}$$

which is substituted back into the right-hand side of (C.15). That is,

$$\begin{aligned} \Delta x_i(h) &\approx g_i Z_1^{(i)}(h) + f_i h + \int_0^h \mathrm{d}t \Big[f_{i,j} \left(g_j Z_1^{(j)}(t) + f_j t \right) \\ &\qquad + \tfrac{1}{2} f_{i,jk} \left(g_j Z_1^{(j)}(t) + f_j t \right) \left(g_k Z_1^{(k)}(t) + f_k t \right) \Big] \\ &= g Z_1^{(i)}(h) + f_i h + f_{i,j} g_j Z_2^{(j)}(h) + \tfrac{1}{2} f_{i,j} f_j h^2 + \tfrac{1}{2} f_{i,jk} g_j g_k Z_3^{(ij)}(h). \end{aligned} \tag{C.17}$$

where terms above order h^2 have been discarded; the order of each stochastic integral can be inferred from equation (C.14). Refining the algorithm by substituting (C.17) in (C.15) is not necessary; this yields only higher-order terms*.

*Attempting to take this integration scheme beyond second order "involves evaluation of

For equation (C.2), $\mathbf{g} = \gamma\sqrt{2D}(0, \ldots, 0, 0, 1, 0, 1)$. Hence, the only potentially non-zero terms in the sum $f_{i,jk}g_jg_k$ are

$$2D\gamma^2\frac{\partial^2 f_i}{\partial u^2}, \quad 2D\gamma^2\frac{\partial^2 f_i}{\partial v^2}, \quad \text{and} \quad 4D\gamma^2\frac{\partial^2 f_i}{\partial u\partial v}\,: \tag{C.18}$$

all derivatives that vanish. It follows that for the type of systems studied in this thesis, the non-Gaussian $Z_3^{(ij)}(h)$ is an avoided complication, and the final, second-order algorithm for numerical integration that I used is

$$\Delta x_i(h) \approx g_i Z_1^{(i)}(h) + f_i h + f_{i,j}g_j Z_2^{(j)}(h) + \tfrac{1}{2}f_{i,j}f_j h^2. \tag{C.19}$$

C.2 Polar coordinates

As shown in appendix A, the eigenfunctions of a circular drum resonator are naturally phrased in terms of polar coordinates. For simplicity, it is thus desirable to reformulate the equations describing particle dynamics from the Cartesian coordinates used in equation (C.2) to polar coordinates.

By substituting $x = r\cos\phi$ and $y = r\sin\phi$, equation (C.2) is transformed to

$$\begin{aligned} \dot{r} &= w, \qquad \dot{w} = r\zeta^2 - \gamma w + \partial_r\mathcal{U}(q_n, r, \phi) + \gamma\sqrt{2D}\;\xi_r(t), \\ \dot{\phi} &= \zeta, \qquad \dot{\zeta} = -2wr^{-1}\zeta - \gamma\zeta + r^{-2}\partial_\phi\mathcal{U}(q_n, r, \phi) + r^{-1}\gamma\sqrt{2D}\;\xi_\phi(t). \end{aligned} \tag{C.20}$$

The only change in the q_n- and p_n-equations is that $\mathcal{U}(q_n, x, y)$ is replaced by $\mathcal{U}(q_n, r, \phi)$, so these equations are omitted in this section.

The significant issue with equation (C.20) is that the angular noise is multiplicative. This represents a significant change in the physical properties of the system, one that should not be caused by a simple change of variables. Additionally, the new terms involving w and ζ means that the $Z_3^{(ij)}(h)$-coefficient no longer vanishes, so the numerical integration is now only valid to first order. Clearly, naïve substitution of variables is not as straight-forward as it might seem.

Instead, I consider small increments in x and y, with corresponding polar increments. To first order,

$$\begin{aligned} x + \Delta x &= (r + \Delta r)\cos(\phi + \Delta\phi) \approx r\cos\phi + \Delta r\cos\phi - r\Delta\phi\sin\phi, \\ y + \Delta y &= (r + \Delta r)\sin(\phi + \Delta\phi) \approx r\sin\phi + \Delta r\sin\phi + r\Delta\phi\cos\phi. \end{aligned} \tag{C.21}$$

stochastic integrals of an increasingly complex nature and the difficulty in evaluating them does not appear to be commensurate with the gain in accuracy" [207].

It follows that

$$\Delta u \approx \Delta w \cos\phi - r\Delta\zeta \sin\phi \qquad \text{and} \qquad \Delta v \approx \Delta w \sin\phi + r\Delta\zeta\cos\phi. \tag{C.22}$$

Now, an algorithm for integrating the equations of motion in polar coordinates can be found using equation (C.19). For instance,

$$\begin{aligned}\Delta r(h) &= \cos\phi\Delta x(h) + \sin\phi\Delta y(h)\\ &= \cos\phi\left(g_x Z_1^{(x)}(h) + f_x h + f_{x,j}g_j Z_2^{(j)}(h) + \tfrac{1}{2}f_{x,j}f_j h^2\right)\\ &\quad + \sin\phi\left(g_y Z_1^{(y)}(h) + f_y h + f_{y,j}g_j Z_2^{(j)}(h) + \tfrac{1}{2}f_{y,j}f_j h^2\right)\\ &\equiv g_r Z_1^{(r)}(h) + f_r h + f_{r,j}g_j Z_2^{(j)}(h) + \tfrac{1}{2}f_{r,j}f_j h^2.\end{aligned} \tag{C.23}$$

In the last step, I defined $f_r(\mathbf{x}(0)) = f_x(\mathbf{x}(0))\cos\phi + f_y(\mathbf{x}(0))\sin\phi$ and $f_{r,j}(\mathbf{x}(0)) = f_{x,j}(\mathbf{x}(0))\cos\phi + f_{y,j}(\mathbf{x}(0))\sin\phi$. The new stochastic integral $Z_1^{(r)}(h)$ is defined as $\cos\phi Z_1^{(x)}(h) + \sin\phi Z_1^{(y)}(h)$. It has expectation zero and variance

$$\begin{aligned}\left\langle Z_1^{(r)}(h)Z_1^{(r)}(h)\right\rangle &= \left\langle\left(\cos\phi Z_1^{(x)}(h) + \sin\phi Z_1^{(y)}(h)\right)^2\right\rangle\\ &= h\cos^2\phi + h\sin^2\phi = h,\end{aligned} \tag{C.24}$$

just like the Cartesian $Z_1^{(j)}(h)$. I have also used that $g_x = g_y = g_r$ (= 0, but all terms are here kept for clarity). One step in the change of variables remains; in equation (C.23), I would like to interpret the summation index j as indexing polar coordinates. This issue is solved by transforming differentiation with respect to Cartesian coordinates into differentiation with respect to polar ones.

It is easy to show that, for any (sufficiently smooth) function F,

$$\begin{aligned}\partial_x F &= \cos\phi\partial_r F - \tfrac{1}{r}\sin\phi\partial_\phi F, \qquad & \partial_y F &= \sin\phi\partial_r F + \tfrac{1}{r}\cos\phi\partial_\phi F,\\ \partial_u F &= \cos\phi\partial_w F - \tfrac{1}{r}\sin\phi\partial_\zeta F, \qquad & \partial_v F &= \sin\phi\partial_w F + \tfrac{1}{r}\cos\phi\partial_\zeta F,\end{aligned} \tag{C.25}$$

since the relationship between u, v, w, and ζ mirrors that of x, y, r, and ϕ. Additionally, new random variables are defined:

$$\begin{aligned}Z_2^{(x)}(h) &= \cos\phi Z_2^{(r)}(h) - \sin\phi Z_2^{(\phi)}(h), \quad & Z_2^{(y)}(h) &= \sin\phi Z_2^{(r)}(h) + \cos\phi Z_2^{(\phi)}(h),\\ Z_2^{(u)}(h) &= \cos\phi Z_2^{(w)}(h) - \sin\phi Z_2^{(\zeta)}(h), \quad & Z_2^{(v)}(h) &= \sin\phi Z_2^{(w)}(h) + \cos\phi Z_2^{(\zeta)}(h).\end{aligned} \tag{C.26}$$

As for $Z_1(h)$, it can be shown that the polar $Z_2(h)$ have the same moments as the Cartesian ones.

Straight-forward substitution now yields

$$\begin{aligned}
f_{r,j}g_jZ_2^{(j)}(h) &= f_{r,x}g_xZ_2^{(x)}(h) + f_{r,y}g_yZ_2^{(y)}(h) + f_{r,u}g_uZ_2^{(u)}(h) + f_{r,v}g_vZ_2^{(v)}(h) \\
&= g_x\left(\cos\phi Z_2^{(r)}(h) - \sin\phi Z_2^{(\phi)}(h)\right)\left(\cos\phi\partial_r - \tfrac{1}{r}\sin\phi\partial_\phi\right)f_r \\
&\quad + g_y\left(\sin\phi Z_2^{(r)}(h) + \cos\phi Z_2^{(\phi)}(h)\right)\left(\sin\phi\partial_r + \tfrac{1}{r}\cos\phi\partial_\phi\right)f_r \\
&\quad + g_u\left(\cos\phi Z_2^{(w)}(h) - \sin\phi Z_2^{(\zeta)}(h)\right)\left(\cos\phi\partial_w - \tfrac{1}{r}\sin\phi\partial_\zeta\right)f_r \\
&\quad + g_v\left(\sin\phi Z_2^{(w)}(h) + \cos\phi Z_2^{(\zeta)}(h)\right)\left(\sin\phi\partial_w + \tfrac{1}{r}\cos\phi\partial_\zeta\right)f_r \\
&= f_{r,r}g_rZ_2^{(r)}(h) + \tfrac{1}{r}f_{r,\phi}Z_2^{(\phi)}(h) + f_{r,w}g_wZ_2^{(w)}(h) + \tfrac{1}{r}f_{r,\zeta}Z_2^{(\zeta)}(h) \\
&= f_{r,j}g_jZ_2^{(j)}(h). \qquad \text{(C.27)}
\end{aligned}$$

In the final line, the summation index j does indeed refer to polar coordinates, with the understanding that $f_{r,\phi} = r^{-1}\partial_\phi f_r$ and $f_{r,\zeta} = r^{-1}\partial_\zeta f_r$. Again, I used the diffusion strength $g_x = g_y = g_r = g_\phi = 0$, and $g_u = g_v = g_w = g_\zeta = \gamma\sqrt{2D}$. Repeating these manipulations for the remaining terms verifies that equation (C.23) is true also when summation is taken over polar coordinates.

In the same manner, I find:

$$\begin{aligned}
\Delta w(h) &= g_wZ_1^{(w)}(h) + f_wh + f_{w,j}g_jZ_2^{(j)}(h) + \tfrac{1}{2}f_{w,j}f_jh^2, \\
\Delta\phi(h) &= \frac{1}{r}\left(g_\phi Z_1^{(\phi)}(h) + f_\phi h + f_{\phi,j}g_jZ_2^{(j)}(h) + \tfrac{1}{2}f_{\phi,j}f_jh^2\right), \\
\Delta\zeta(h) &= \frac{1}{r}\left(g_\zeta Z_1^{(\zeta)}(h) + f_\zeta h + f_{\zeta,j}g_jZ_2^{(j)}(h) + \tfrac{1}{2}f_{\zeta,j}f_jh^2\right), \qquad \text{(C.28)}
\end{aligned}$$

where $Z_1^{(j)}(h)$ and $Z_2^{(j)}(h)$ are given by equation (C.14).

Bibliography

[1] G. L. Baker and J. A. Blackburn. *The Pendulum: A Case Study in Physics*. Oxford University Press, first edition (2005).

[2] D. K. Campbell. Nonlinear physics: Fresh breather. Nature **432**, 455 (2004).

[3] Harvard Natural Sciences Lecture Demonstrations. Inverted pendulum. `https://sciencedemonstrations.fas.harvard.edu/presentations/inverted-pendulum`. Accessed: 2017-05-30.

[4] P. Coullet, J.-M. Gilli, and G. Rousseaux. On the critical equilibrium of the spiral spring pendulum. Proc. R. Soc. London, Ser. A **466**, 407 (2009).

[5] L. Tolstoy. *Anna Karenina*. Yale University Press (2014).

[6] A. H. Nayfeh and D. T. Mook. *Nonlinear Oscillations*. Wiley-VCH (1995).

[7] X. L. Feng, C. J. White, A. Hajimiri, and M. L. Roukes. A self-sustaining ultrahigh-frequency nanoelectromechanical oscillator. Nat. Nanotech. **3**, 342 (2008).

[8] P. R. Wallace. The band theory of graphite. Phys. Rev. **71**, 622 (1947).

[9] G. S. Painter and D. E. Ellis. Electronic band structure and optical properties of graphite from a variational approach. Phys. Rev. B **1**, 4747 (1970).

[10] G. W. Semenoff. Condensed-matter simulation of a three-dimensional anomaly. Phys. Rev. Lett. **53**, 2449 (1984).

[11] D. P. DiVincenzo and E. J. Mele. Self-consistent effective-mass theory for intralayer screening in graphite intercalation compounds. Phys. Rev. B **29**, 1685 (1984).

[12] R. Peierls. Quelques propriétés typiques des corps solides. Annales de l'institut Henri Poincaré **5**, 177 (1935).

[13] N. D. Mermin. Crystalline order in two dimensions. Phys. Rev. **176**, 250 (1968).

[14] K. S. Novoselov, A. K. Geim, S. V. Morozov, D. Jiang, Y. Zhang, S. V. Dubonos, I. V. Grigorieva, and A. A. Firsov. Electric field effect in atomically thin carbon films. Science **306**, 666 (2004).

[15] A. Geim. Random walk to graphene. Nobel Lecture (2010).

[16] The 2010 Nobel Prize in Physics - Press Release (2010).

[17] S. Iijima and T. Ichihashi. Single-shell carbon nanotubes of 1-nm diameter. Nature **363**, 603 (1993).

[18] D. S. Bethune, C. H. Klang, M. S. de Vries, G. Gorman, R. Savoy, J. Vazquez, and R. Beyers. Cobalt-catalysed growth of carbon nanotubes with single-atomic-layer walls. Nature **363**, 605 (1993).

[19] M. Monthioux and V. L. Kuznetsov. Who should be given the credit for the discovery of carbon nanotubes? Carbon **44**, 1621 (2006).

[20] L. J. E. Hofer, E. Sterling, and J. T. McCartney. Structure of carbon deposited from carbon monoxide on iron, cobalt and nickel. J. Phys. Chem. **59**, 1153 (1955).

[21] S. Iijima. Helical microtubules of graphitic carbon. Nature **354**, 56 (1991).

[22] C. Lee, X. Wei, J. W. Kysar, and J. Hone. Measurement of the elastic properties and intrinsic strength of monolayer graphene. Science **321**, 385 (2008).

[23] The 2010 Nobel Prize in Physics - Advanced Information (2010).

[24] K. N. Kudin, G. E. Scuseria, and B. I. Yakobson. C_2F, BN, and C nanoshell elasticity from *ab initio* computations. Phys. Rev. B **64**, 235406 (2001).

[25] E. Pop, D. Mann, Q. Wang, K. Goodson, and H. Dai. Thermal conductance of an individual single-wall carbon nanotube above room temperature. Nano Lett. **6**, 96 (2006).

[26] A. A. Balandin, S. Ghosh, W. Bao, I. Calizo, D. Teweldebrhan, F. Miao, and C. N. Lau. Superior thermal conductivity of single-layer graphene. Nano Lett. **8**, 902 (2008).

[27] S. Chen, A. L. Moore, W. Cai, J. W. Suk, J. An, C. Mishra, C. Amos, C. W. Magnuson, J. Kang, L. Shi, and R. S. Ruoff. Raman measurements of thermal transport in suspended monolayer graphene of variable sizes in vacuum and gaseous environments. ACS Nano **5**, 321 (2011).

[28] R. R. Nair, P. Blake, A. N. Grigorenko, K. S. Novoselov, T. J. Booth, T. Stauber, N. M. R. Peres, and A. K. Geim. Fine structure constant defines visual transparency of graphene. Science **320**, 1308 (2008).

[29] X. Wang, L. Zhi, and K. Müllen. Transparent, conductive graphene electrodes for dye-sensitized solar cells. Nano Lett. **8**, 323 (2008).

[30] C. D. Sheraw, L. Zhou, J. R. Huang, D. J. Gundlach, T. N. Jackson, M. G. Kane, I. G. Hill, M. S. Hammond, J. Campi, B. K. Greening, J. Francl, and J. West. Organic thin-film transistor-driven polymer-dispersed liquid crystal displays on flexible polymeric substrates. Appl. Phys. Lett. **80**, 1088 (2002).

[31] G. G. Liangbing Hu. Touch screen devices employing nanostructure networks. U.S. patent no. 8390589 (2013).

[32] T. Georgiou, R. Jalil, B. D. Belle, L. Britnell, R. V. Gorbachev, S. V. Morozov, Y.-J. Kim, A. Gholinia, S. J. Haigh, O. Makarovsky, L. Eaves, L. A. Ponomarenko, A. K. Geim, K. S. Novoselov, and A. Mishchenko. Vertical field-effect transistor based on graphene-WS_2 heterostructures for flexible and transparent electronics. Nat. Nanotech. **8**, 100 (2013).

[33] G. Binnig, C. F. Quate, and C. Gerber. Atomic force microscope. Phys. Rev. Lett. **56**, 930 (1986).

[34] Y. Martin, C. C. Williams, and H. K. Wickramasinghe. Atomic force microscope–force mapping and profiling on a sub 100-Å scale. J. Appl. Phys. **61**, 4723 (1987).

[35] T. R. Albrecht, P. Grütter, D. Horne, and D. Rugar. Frequency modulation detection using high-Q cantilevers for enhanced force microscope sensitivity. J. Appl. Phys. **69**, 668 (1991).

[36] H. P. Lang, M. Hegner, E. Meyer, and C. Gerber. Nanomechanics from atomic resolution to molecular recognition based on atomic force microscopy technology. Nanotechnology **13**, R29 (2002).

[37] V. Friedli, S. Hoffmann, J. Michler, and I. Utke. AFM sensors in scanning electron and ion microscopes: Tools for nanomechanics, nanoanalytics, and

nanofabrication. In B. Bhushan, H. Fuchs, and M. Tomitori, editors, *Applied Scanning Probe Methods VIII: Scanning Probe Microscopy Techniques*. Springer, Berlin, Heidelberg (2008).

[38] K. L. Ekinci and M. L. Roukes. Nanoelectromechanical systems. Rev. Sci. Instrum. **76**, 061101 (2005).

[39] B. Arash, J.-W. Jiang, and T. Rabczuk. A review on nanomechanical resonators and their applications in sensors and molecular transportation. Appl. Phys. Rev. **2**, 021301 (2015).

[40] H. B. Meerwaldt, G. Labadze, B. H. Schneider, A. Taspinar, Y. M. Blanter, H. S. J. van der Zant, and G. A. Steele. Probing the charge of a quantum dot with a nanomechanical resonator. Phys. Rev. B **86**, 115454 (2012).

[41] P. Häkkinen, A. Isacsson, A. Savin, J. Sulkko, and P. Hakonen. Charge sensitivity enhancement via mechanical oscillation in suspended carbon nanotube devices. Nano Lett. **15**, 1667 (2015).

[42] G. A. Steele, A. K. Hüttel, B. Witkamp, M. Poot, H. B. Meerwaldt, L. P. Kouwenhoven, and H. S. J. van der Zant. Strong coupling between single-electron tunneling and nanomechanical motion. Science **325**, 1103 (2009).

[43] A. N. Cleland and M. L. Roukes. A nanometre-scale mechanical electrometer. Nature **392**, 160 (1998).

[44] J. Jalil, Y. Zhu, C. Ekanayake, and Y. Ruan. Sensing of single electrons using micro and nano technologies: a review. Nanotechnology **28**, 142002 (2017).

[45] L. M. de Lépinay, B. Pigeau, B. Besga, P. Vincent, P. Poncharal, and O. Arcizet. A universal and ultrasensitive vectorial nanomechanical sensor for imaging 2D force fields. Nat. Nanotech. **12**, 156 (2017).

[46] H. J. Mamin and D. Rugar. Sub-attonewton force detection at millikelvin temperatures. Appl. Phys. Lett. **79**, 3358 (2001).

[47] G. Yoshikawa, T. Akiyama, S. Gautsch, P. Vettiger, and H. Rohrer. Nanomechanical membrane-type surface stress sensor. Nano Lett. **11**, 1044 (2011).

[48] J. Moser, J. Güttinger, A. Eichler, M. J. Esplandiu, D. E. Liu, M. I. Dykman, and A. Bachtold. Ultrasensitive force detection with a nanotube mechanical resonator. Nat. Nanotech. **8**, 493 (2013).

[49] A. N. Cleland, J. S. Aldridge, D. C. Driscoll, and A. C. Gossard. Nanomechanical displacement sensing using a quantum point contact. Appl. Phys. Lett. **81**, 1699 (2002).

[50] R. G. Knobel and A. N. Cleland. Nanometre-scale displacement sensing using a single electron transistor. Nature **424**, 291 (2003).

[51] M. D. LaHaye, O. Buu, B. Camarota, and K. C. Schwab. Approaching the quantum limit of a nanomechanical resonator. Science **304**, 74 (2004).

[52] D. Rugar, R. Budakian, H. J. Mamin, and B. W. Chui. Single spin detection by magnetic resonance force microscopy. Nature **430**, 329 (2004).

[53] J. M. Nichol, E. R. Hemesath, L. J. Lauhon, and R. Budakian. Nanomechanical detection of nuclear magnetic resonance using a silicon nanowire oscillator. Phys. Rev. B **85**, 054414 (2012).

[54] K. L. Ekinci, Y. T. Yang, and M. L. Roukes. Ultimate limits to inertial mass sensing based upon nanoelectromechanical systems. J. Appl. Phys. **95**, 2682 (2004).

[55] J. Atalaya, J. M. Kinaret, and A. Isacsson. Nanomechanical mass measurement using nonlinear response of a graphene membrane. Europhys. Lett. **91**, 48001 (2010).

[56] E. Gil-Santos, D. Ramos, J. Martinez, M. Fernandez-Regulez, R. Garcia, A. San Paulo, M. Calleja, and J. Tamayo. Nanomechanical mass sensing and stiffness spectrometry based on two-dimensional vibrations of resonant nanowires. Nat. Nanotech. **5**, 641 (2010).

[57] M. S. Hanay, S. Kelber, A. K. Naik, D. Chi, S. Hentz, E. C. Bullard, E. Colinet, L. Duraffourg, and M. L. Roukes. Single-protein nanomechanical mass spectrometry in real time. Nat. Nanotech. **7**, 602 (2012).

[58] A. Tavernarakis, J. Chaste, A. Eichler, G. Ceballos, M. C. Gordillo, J. Boronat, and A. Bachtold. Atomic monolayer deposition on the surface of nanotube mechanical resonators. Phys. Rev. Lett. **112**, 196103 (2014).

[59] K. Jensen, K. Kim, and A. Zettl. An atomic-resolution nanomechanical mass sensor. Nat. Nanotech. **3**, 533 (2008).

[60] B. Lassagne, D. Garcia-Sanchez, A. Aguasca, and A. Bachtold. Ultrasensitive mass sensing with a nanotube electromechanical resonator. Nano Lett. **8**, 3735 (2008).

[61] J. Chaste, A. Eichler, J. Moser, G. Ceballos, R. Rurali, and A. Bachtold. A nanomechanical mass sensor with yoctogram resolution. Nat. Nanotech. **7**, 301 (2012).

[62] W. J. Venstra, M. J. Capener, and S. R. Elliott. Nanomechanical gas sensing with nonlinear resonant cantilevers. Nanotechnology **25**, 425501 (2014).

[63] F. Schedin, A. K. Geim, S. V. Morozov, E. W. Hill, P. Blake, M. I. Katsnelson, and K. S. Novoselov. Detection of individual gas molecules adsorbed on graphene. Nat. Mater. **6**, 652 (2007).

[64] T. P. Burg, M. Godin, S. M. Knudsen, W. Shen, G. Carlson, J. S. Foster, K. Babcock, and S. R. Manalis. Weighing of biomolecules, single cells and single nanoparticles in fluid. Nature **446**, 1066 (2007).

[65] J. Lee, W. Shen, K. Payer, T. P. Burg, and S. R. Manalis. Toward attogram mass measurements in solution with suspended nanochannel resonators. Nano Lett. **10**, 2537 (2010).

[66] S. Olcum, N. Cermak, S. C. Wasserman, K. S. Christine, H. Atsumi, K. R. Payer, W. Shen, J. Lee, A. M. Belcher, S. N. Bhatia, and S. R. Manalis. Weighing nanoparticles in solution at the attogram scale. Proc. Natl. Acad. Sci. U.S.A. **111**, 1310 (2014).

[67] J. Fritz, M. K. Baller, H. P. Lang, H. Rothuizen, P. Vettiger, E. Meyer, H. J. Güntherodt, C. Gerber, and J. K. Gimzewski. Translating biomolecular recognition into nanomechanics. Science **288**, 316 (2000).

[68] P. S. Waggoner and H. G. Craighead. Micro- and nanomechanical sensors for environmental, chemical, and biological detection. Lab Chip **7**, 1238 (2007).

[69] P. A. Greaney and J. C. Grossman. Nanomechanical resonance spectroscopy: A novel route to ultrasensitive label-free detection. Nano Lett. **8**, 2648 (2008).

[70] Y. Shao, J. Wang, H. Wu, J. Liu, I. Aksay, and Y. Lin. Graphene based electrochemical sensors and biosensors: A review. Electroanalysis **22**, 1027 (2010).

[71] J. L. Arlett, E. B. Myers, and M. L. Roukes. Comparative advantages of mechanical biosensors. Nat. Nanotech. **6**, 203 (2011).

[72] K. Eom, H. S. Park, D. S. Yoon, and T. Kwon. Nanomechanical resonators and their applications in biological/chemical detection: Nanomechanics principles. Phys. Rep. **503**, 115 (2011).

[73] J. Tamayo, P. M. Kosaka, J. J. Ruz, A. San Paulo, and M. Calleja. Biosensors based on nanomechanical systems. Chem. Soc. Rev. **42**, 1287 (2013).

[74] J. W. Ndieyira, N. Kappeler, S. Logan, M. A. Cooper, C. Abell, R. A. McKendry, and G. Aeppli. Surface-stress sensors for rapid and ultrasensitive detection of active free drugs in human serum. Nat. Nanotech. **9**, 225 (2014).

[75] O. Malvar, J. J. Ruz, P. M. Kosaka, C. M. Domínguez, E. Gil-Santos, M. Calleja, and J. Tamayo. Mass and stiffness spectrometry of nanoparticles and whole intact bacteria by multimode nanomechanical resonators. Nat. Commun. **7**, 13452 (2016).

[76] V. Sazonova, Y. Yaish, H. Ustunel, D. Roundy, T. A. Arias, and P. L. McEuen. A tunable carbon nanotube electromechanical oscillator. Nature **431**, 284 (2004).

[77] D. Garcia-Sanchez, A. San Paulo, M. J. Esplandiu, F. Perez-Murano, L. Forró, A. Aguasca, and A. Bachtold. Mechanical detection of carbon nanotube resonator vibrations. Phys. Rev. Lett. **99**, 085501 (2007).

[78] A. K. Hüttel, G. A. Steele, B. Witkamp, M. Poot, L. P. Kouwenhoven, and H. S. J. van der Zant. Carbon nanotubes as ultrahigh quality factor mechanical resonators. Nano Lett. **9**, 2547 (2009).

[79] J. S. Bunch, A. M. van der Zande, S. S. Verbridge, I. W. Frank, D. M. Tanenbaum, J. M. Parpia, H. G. Craighead, and P. L. McEuen. Electromechanical resonators from graphene sheets. Science **315**, 490 (2007).

[80] J. Atalaya, A. Isacsson, and J. M. Kinaret. Continuum elastic modeling of graphene resonators. Nano Lett. **8**, 4196 (2008).

[81] D. Garcia-Sanchez, A. M. van der Zande, A. S. Paulo, B. Lassagne, P. L. McEuen, and A. Bachtold. Imaging mechanical vibrations in suspended graphene sheets. Nano Lett. **8**, 1399 (2008).

[82] C. Chen, S. Rosenblatt, K. I. Bolotin, W. Kalb, P. Kim, I. Kymissis, H. L. Stormer, T. F. Heinz, and J. Hone. Performance of monolayer graphene nanomechanical resonators with electrical readout. Nat. Nanotech. **4**, 861 (2009).

[83] J. Henriksson, L. G. Villanueva, and J. Brugger. Ultra-low power hydrogen sensing based on a palladium-coated nanomechanical beam resonator. Nanoscale **4**, 5059 (2012).

[84] M. Kumar and H. Bhaskaran. Ultrasensitive room-temperature piezoresistive transduction in graphene-based nanoelectromechanical systems. Nano Lett. **15**, 2562 (2015).

[85] V. Gouttenoire, T. Barois, S. Perisanu, J.-L. Leclercq, S. T. Purcell, P. Vincent, and A. Ayari. Digital and FM demodulation of a doubly clamped single-walled carbon-nanotube oscillator: Towards a nanotube cell phone. Small **6**, 1060 (2010).

[86] L. D. Landau and E. M. Lifshitz. *Theory of Elasticity*, volume 7 of *Course of Theoretical Physics*. Butterworth-Heinemann, third edition (1986).

[87] C. Edblom. *Diffusion-Induced Nonlinear Dynamics in Carbon Nanomechanical Resonators*. Phil. Lic. thesis, Chalmers University of Technology (2015).

[88] J. Bardeen, L. N. Cooper, and J. R. Schrieffer. Theory of superconductivity. Phys. Rev. **108**, 1175 (1957).

[89] H. Kamerlingh Onnes. Further experiments with liquid helium. D. On the change of electrical resistance of pure metals at very low temperatures, etc. V. The disappearance of the resistance of mercury. Proc. R. Soc. Amsterdam **14**, 113 (1911).

[90] L. D. Landau and E. M. Lifshitz. *Statistical Physics, Part 2*, volume 9 of *Course of Theoretical Physics*. Butterworth-Heinemann, third edition (1980).

[91] L. N. Cooper. Bound electron pairs in a degenerate Fermi gas. Phys. Rev. **104**, 1189 (1956).

[92] A. Altland and B. Simons. *Condensed Matter Field Theory*. Cambridge University Press, second edition (2010).

[93] P. Nozières and S. Schmitt-Rink. Bose condensation in an attractive fermion gas: From weak to strong coupling superconductivity. J. Low Temp. Phys. **59**, 195 (1985).

[94] A. J. Leggett and S. Zhang. The BEC–BCS crossover: Some history and some general observations. In W. Zwerger, editor, *The BCS-BEC Crossover and the Unitary Fermi Gas*. Springer, Berlin, Heidelberg (2012).

[95] C. A. Regal, M. Greiner, and D. S. Jin. Observation of resonance condensation of fermionic atom pairs. Phys. Rev. Lett. **92**, 040403 (2004).

[96] B. Josephson. Possible new effects in superconductive tunnelling. Phys. Lett. **1**, 251 (1962).

[97] P. W. Anderson and J. M. Rowell. Probable observation of the Josephson superconducting tunneling effect. Phys. Rev. Lett. **10**, 230 (1963).

[98] J. D. Jackson. *Classical Electrodynamics*. Wiley, third edition (1999).

[99] R. C. Jaklevic, J. Lambe, A. H. Silver, and J. E. Mercereau. Quantum interference effects in Josephson tunneling. Phys. Rev. Lett. **12**, 159 (1964).

[100] M. Tinkham. *Introduction to Superconductivity*. Dover Publications, second edition (1996).

[101] M. Hämäläinen, R. Hari, R. J. Ilmoniemi, J. Knuutila, and O. V. Lounasmaa. Magnetoencephalography: theory, instrumentation, and applications to noninvasive studies of the working human brain. Rev. Mod. Phys. **65**, 413 (1993).

[102] J. Clarke and F. K. Wilhelm. Superconducting quantum bits. Nature **453**, 1031 (2008).

[103] J. Q. You and F. Nori. Atomic physics and quantum optics using superconducting circuits. Nature **474**, 589 (2011).

[104] M. Göppl, A. Fragner, M. Baur, R. Bianchetti, S. Filipp, J. M. Fink, P. J. Leek, G. Puebla, L. Steffen, and A. Wallraff. Coplanar waveguide resonators for circuit quantum electrodynamics. J. Appl. Phys. **104**, 113904 (2008).

[105] H. Walther, B. T. H. Varcoe, B.-G. Englert, and T. Becker. Cavity quantum electrodynamics. Rep. Prog. Phys. **69**, 1325 (2006).

[106] I. Chiorescu, P. Bertet, K. Semba, Y. Nakamura, C. J. P. M. Harmans, and J. E. Mooij. Coherent dynamics of a flux qubit coupled to a harmonic oscillator. Nature **431**, 159 (2004).

[107] A. Wallraff, D. I. Schuster, A. Blais, L. Frunzio, R.-S. Huang, J. Majer, S. Kumar, S. M. Girvin, and R. J. Schoelkopf. Strong coupling of a single photon to a superconducting qubit using circuit quantum electrodynamics. Nature **431**, 162 (2004).

[108] M. Hofheinz, H. Wang, M. Ansmann, R. C. Bialczak, E. Lucero, M. Neeley, A. D. O'Connell, D. Sank, J. Wenner, J. M. Martinis, and A. N. Cleland. Synthesizing arbitrary quantum states in a superconducting resonator. Nature **459**, 546 (2009).

[109] A. Blais, R.-S. Huang, A. Wallraff, S. M. Girvin, and R. J. Schoelkopf. Cavity quantum electrodynamics for superconducting electrical circuits: an architecture for quantum computation. Phys. Rev. A **69**, 062320 (2004).

[110] R. J. Schoelkopf and S. M. Girvin. Wiring up quantum systems. Nature **451**, 664 (2008).

[111] E. T. Jaynes and F. W. Cummings. Comparison of quantum and semiclassical radiation theories with application to the beam maser. Proc. IEEE **51**, 89 (1963).

[112] B. W. Shore and P. L. Knight. The Jaynes-Cummings model. J. Mod. Opt. **40**, 1195 (1993).

[113] F. R. Carlos Bustamante, Jan Liphardt. The nonequilibrium thermodynamics of small systems. Physics Today **58**, 43 (2005).

[114] M. L. Simpson and P. T. Cummings. Fluctuations and correlations in physical and biological nanosystems: The tale is in the tails. ACS Nano **4**, 2425 (2011).

[115] U. Seifert. Stochastic thermodynamics, fluctuation theorems and molecular machines. Rep. Prog. Phys. **75**, 126001 (2012).

[116] M. T. H. Reid, A. W. Rodriguez, and S. G. Johnson. Fluctuation-induced phenomena in nanoscale systems: Harnessing the power of noise. Proc. IEEE **101**, 531 (2013).

[117] G. M. Wang, E. M. Sevick, E. Mittag, D. J. Searles, and D. J. Evans. Experimental demonstration of violations of the second law of thermodynamics for small systems and short time scales. Phys. Rev. Lett. **89**, 050601 (2002).

[118] G. E. Crooks. On thermodynamic and microscopic reversibility. J. Stat. Mech. Theor. Exp. **2011**, P07008 (2011).

[119] I. Tsioutsios, A. Tavernarakis, J. Osmond, P. Verlot, and A. Bachtold. Real-time measurement of nanotube resonator fluctuations in an electron microscope. Nano Lett. **17**, 1748 (2017).

[120] K. Y. Fong, W. H. P. Pernice, and H. X. Tang. Frequency and phase noise of ultrahigh Q silicon nitride nanomechanical resonators. Phys. Rev. B **85**, 161410 (2012).

[121] T. Miao, S. Yeom, P. Wang, B. Standley, and M. Bockrath. Graphene nanoelectromechanical systems as stochastic-frequency oscillators. Nano Lett. **14**, 2982 (2014).

[122] Y. Zhang, J. Moser, J. Güttinger, A. Bachtold, and M. I. Dykman. Interplay of driving and frequency noise in the spectra of vibrational systems. Phys. Rev. Lett. **113**, 255502 (2014).

[123] A. W. Barnard, V. Sazonova, A. M. van der Zande, and P. L. McEuen. Fluctuation broadening in carbon nanotube resonators. Proc. Natl. Acad. Sci. U.S.A. **109**, 19093 (2012).

[124] M. Sansa, E. Sage, E. C. Bullard, M. Gély, T. Alava, E. Colinet, A. K. Naik, L. G. Villanueva, L. Duraffourg, M. L. Roukes, G. Jourdan, and S. Hentz. Frequency fluctuations in silicon nanoresonators. Nat. Nanotech. **11**, 552 (2016).

[125] L. D. Landau and E. M. Lifshitz. *Statistical Physics, Part 1*, volume 5 of *Course of Theoretical Physics*. Butterworth-Heinemann, third edition (1980).

[126] C. W. Gardiner. *Handbook of Stochastic Methods for Physics, Chemistry and the Natural Sciences*. Springer, second edition (1985).

[127] S. E. Shreve. *Stochastic Calculus for Finance II: Continuous-Time Models*. Springer (2008).

[128] A. O. Caldeira and A. J. Leggett. Influence of dissipation on quantum tunneling in macroscopic systems. Phys. Rev. Lett. **46**, 211 (1981).

[129] D. Midtvedt. *Nonlinear Electromechanics of Nanomembranes and Nanotubes*. Ph.D. thesis, Chalmers University of Technology (2013).

[130] N. G. van Kampen. *Stochastic Processes in Physics and Chemistry*. North-Holland (1981).

[131] P. Langevin. Sur la théorie du mouvement Brownien. Comptes Rendus de l'Académie des Sciences **146**, 530 (1908).

[132] G. E. Uhlenbeck and L. S. Ornstein. On the theory of the brownian motion. Phys. Rev. **36**, 823 (1930).

[133] R. Kubo. The fluctuation-dissipation theorem. Rep. Prog. Phys. **29**, 255 (1966).

[134] E. Loken and A. Gelman. Measurement error and the replication crisis. Science **355**, 584 (2017).

[135] R. Mannella and P. V. E. McClintock. Noise in nonlinear dynamical systems. Contemp. Phys. **31**, 179 (1990).

[136] W. Horsthemke and R. Lefever. Noise-induced nonequilibrium phase transitions. In *Noise-Induced Transitions: Theory and Applications in Physics, Chemistry, and Biology*. Springer, Berlin, Heidelberg (1984).

[137] S. Aldridge. The Duffing oscillator for nanoelectromechanical systems. In G. Radons, B. Rumpf, and H. Schuster, editors, *Nonlinear Dynamics of Nanosystems*. Wiley, Weinheim (2010).

[138] H. B. Chan and C. Stambaugh. Activated switching in nonlinear micromechanical resonators. In M. I. Dykman, editor, *Fluctuating Nonlinear Oscillators: From Nanomechanics to Quantum Superconducting Circuits*. Oxford University Press, Oxford (2012).

[139] L. Gammaitoni, P. Hänggi, P. Jung, and F. Marchesoni. Stochastic resonance. Rev. Mod. Phys. **70**, 223 (1998).

[140] H. Kramers. Brownian motion in a field of force and the diffusion model of chemical reactions. Physica **7**, 284 (1940).

[141] R. Benzi, G. Parisi, A. Sutera, and A. Vulpiani. Stochastic resonance in climatic change. Tellus **34**, 10 (1982).

[142] C. Nicolis. Stochastic aspects of climatic transitions – response to a periodic forcing. Tellus **34**, 1 (1982).

[143] S. Fauve and F. Heslot. Stochastic resonance in a bistable system. Phys. Lett. A **97**, 5 (1983).

[144] A. Simon and A. Libchaber. Escape and synchronization of a B rownian particle. Phys. Rev. Lett. **68**, 3375 (1992).

[145] F. Ricci, R. A. Rica, M. Spasenović, J. Gieseler, L. Rondin, L. Novotny, and R. Quidant. Optically levitated nanoparticle as a model system for stochastic bistable dynamics. Nat. Commun. **8**, 15141 (2017).

[146] R. L. Badzey and P. Mohanty. Coherent signal amplification in bistable nanomechanical oscillators by stochastic resonance. Nature **437**, 995 (2005).

[147] K. Wiesenfeld and F. Moss. Stochastic resonance and the benefits of noise: from ice ages to crayfish and squids. Nature **373**, 33 (1995).

[148] E. Shapira, R. Pujol, M. Plaksin, and E. Kimmel. Sound-induced motility of outer hair cells explained by stochastic resonance in nanometric sensors in the lateral wall. Physics in Medicine **2**, 1 (2016).

[149] A. D. McDonnell, Mark D. What is stochastic resonance? Definitions, misconceptions, debates, and its relevance to biology. PLOS Comput. Biol. **5**, e1000348 (2009).

[150] B. McNamara, K. Wiesenfeld, and R. Roy. Observation of stochastic resonance in a ring laser. Phys. Rev. Lett. **60**, 2626 (1988).

[151] W. M. Macek and D. T. M. Davis Jr. Rotation rate sensing with traveling-wave ring lasers. Appl. Phys. Lett. **2**, 67 (1963).

[152] K. Vogel, H. Risken, W. Schleich, M. James, F. Moss, and P. V. E. McClintock. Skewed probability densities in the ring laser gyroscope: A colored noise effect. Phys. Rev. A **35**, 463 (1987).

[153] K. Vogel, H. Risken, and W. Schleich. Noise in a ring-laser gyroscope. In F. Moss and P. V. E. McClintock, editors, *Noise in Nonlinear Dynamical Systems*, volume 2. Cambridge University Press, Cambridge (1989).

[154] M. Serra-Garcia, A. Foehr, M. Molerón, J. Lydon, C. Chong, and C. Daraio. Mechanical autonomous stochastic heat engine. Phys. Rev. Lett. **117**, 010602 (2016).

[155] R. Sánchez, H. Thierschmann, and L. W. Molenkamp. All-thermal transistor based on stochastic switching. Phys. Rev. B **95**, 241401 (2017).

[156] A. A. Faisal, L. P. J. Selen, and D. M. Wolpert. Noise in the nervous system. Nat. Rev. Neurosci. **9**, 292 (2008).

[157] C. Blomberg. Fluctuations for good and bad: The role of noise in living systems. Phys. Life Rev. **3**, 133 (2006).

[158] M. Gitterman. *The Noisy Oscillator. Random Mass, Frequency, Damping.* World Scientific, second edition (2013).

[159] N. G. van Kampen. Itô versus Stratonovich. J. Stat. Phys. **24**, 175 (1981).

[160] R. Mannella and P. V. E. McClintock. Itô versus Stratonovich: 30 years later. Fluct. Noise Lett. **11**, 1240010 (2012).

[161] I. Sokolov. Ito, Stratonovich, Hänggi and all the rest: The thermodynamics of interpretation. Chem. Phys. **375**, 359 (2010).

[162] K. Itō. Stochastic integral. Proc. Imp. Acad. **20**, 519 (1944).

[163] R. L. Stratonovich. A new representation for stochastic integrals and equations. SIAM J. Control **4**, 362 (1966).

[164] I. Newton. *The Mathematical Principles of Natural Philosophy*, volume 1. Benjamin Motte, London (1729).

[165] M. Dämmig and F. Mitschke. Estimation of Lyapunov exponents from time series: the stochastic case. Phys. Lett. A **178**, 385 (1993).

[166] N. Sviridova and K. Nakamura. Local noise sensitivity: insight into the noise effect on chaotic dynamics. Chaos **26**, 123102 (2016).

[167] F. Marquardt. An introduction to the basics of dephasing. `http://www.quantum3000.narod.ru/papers/edu/dephasing.pdf`. Accessed: 2017-07-10.

[168] J. W. S. Rayleigh. *The Theory of Sound*, volume 1. Dover, second edition (2014).

[169] A. N. Cleland and M. L. Roukes. Noise processes in nanomechanical resonators. J. Appl. Phys. **92**, 2758 (2002).

[170] Z. A. Maizelis, M. L. Roukes, and M. I. Dykman. Detecting and characterizing frequency fluctuations of vibrational modes. Phys. Rev. B **84**, 144301 (2011).

[171] J. Atalaya. Mass loading induced dephasing in nanomechanical resonators. J. Phys. Condens. Matter **24**, 475301 (2012).

[172] M. I. Dykman, M. Khasin, J. Portman, and S. W. Shaw. Spectrum of an oscillator with jumping frequency and the interference of partial susceptibilities. Phys. Rev. Lett. **105**, 230601 (2010).

[173] J. Atalaya, A. Isacsson, and M. I. Dykman. Diffusion-induced dephasing in nanomechanical resonators. Phys. Rev. B **83**, 045419 (2011).

[174] Y. T. Yang, C. Callegari, X. L. Feng, and M. L. Roukes. Surface adsorbate fluctuations and noise in nanoelectromechanical systems. Nano Lett. **11**, 1753 (2011).

[175] J. Atalaya, A. Isacsson, and M. I. Dykman. Diffusion-induced bistability of driven nanomechanical resonators. Phys. Rev. Lett. **106**, 227202 (2011).

[176] R. Lifshitz and M. C. Cross. Nonlinear dynamics of nanomechanical resonators. In G. Radons, B. Rumpf, and H. Schuster, editors, *Nonlinear Dynamics of Nanosystems*. Wiley-VCH, Weinheim (2010).

[177] A. Eichler, J. Moser, J. Chaste, M. Zdrojek, I. Wilson-Rae, and A. Bachtold. Nonlinear damping in mechanical resonators made from carbon nanotubes and graphene. Nat. Nanotech. **6**, 339 (2011).

[178] A. Croy, D. Midtvedt, A. Isacsson, and J. M. Kinaret. Nonlinear damping in graphene resonators. Phys. Rev. B **86**, 235435 (2012).

[179] J. Atalaya, T. W. Kenny, M. L. Roukes, and M. I. Dykman. Nonlinear damping and dephasing in nanomechanical systems. Phys. Rev. B **94**, 195440 (2016).

[180] A. M. Eriksson, D. Midtvedt, A. Croy, and A. Isacsson. Frequency tuning, nonlinearities and mode coupling in circular mechanical graphene resonators. Nanotechnology **24**, 395702 (2013).

[181] D. Midtvedt, A. Croy, A. Isacsson, Z. Qi, and H. S. Park. Fermi-Pasta-Ulam physics with nanomechanical graphene resonators: intrinsic relaxation and thermalization from flexural mode coupling. Phys. Rev. Lett. **112**, 145503 (2014).

[182] P. A. Greaney, G. Lani, G. Cicero, and J. C. Grossman. Anomalous dissipation in single-walled carbon nanotube resonators. Nano Lett. **9**, 3699 (2009).

[183] C. Chen, D. H. Zanette, D. A. Czaplewski, S. Shaw, and D. López. Direct observation of coherent energy transfer in nonlinear micromechanical oscillators. Nat. Commun. **8**, 15523 (2017).

[184] J. Güttinger, A. Noury, P. Weber, A. M. Eriksson, C. Lagoin, J. Moser, C. Eichler, A. Wallraff, A. Isacsson, and A. Bachtold. Energy-dependent path of dissipation in nanomechanical resonators. Nat. Nanotech. **12**, 631 (2017).

[185] O. Shoshani, S. W. Shaw, and M. I. Dykman. Anomalous dissipation of nanomechanical modes going through nonlinear resonance. arXiv:1702.00769 (2017).

[186] Y. Zhang and M. I. Dykman. Spectral effects of dispersive mode coupling in driven mesoscopic systems. Phys. Rev. B **92**, 165419 (2015).

[187] H. B. Meerwaldt, S. R. Johnston, H. S. J. van der Zant, and G. A. Steele. Submicrosecond-timescale readout of carbon nanotube mechanical motion. Appl. Phys. Lett. **103**, 053121 (2013).

[188] R. van Leeuwen, A. Castellanos-Gomez, G. A. Steele, H. S. J. van der Zant, and W. J. Venstra. Time-domain response of atomically thin MoS_2 nanomechanical resonators. Appl. Phys. Lett. **105**, 041911 (2014).

[189] B. H. Schneider, V. Singh, W. J. Venstra, H. B. Meerwaldt, and G. A. Steele. Observation of decoherence in a carbon nanotube mechanical resonator. Nat. Commun. **5**, 5819 (2014).

[190] O. Maillet, F. Vavrek, A. D. Fefferman, O. Bourgeois, and E. Collin. Classical decoherence in a nanomechanical resonator. New J. Phys. **18**, 073022 (2016).

[191] R. Mannella. Computer experiments in non-linear stochastic physics. In F. Moss and P. V. E. McClintock, editors, *Noise in Nonlinear Dynamical Systems*, volume 3. Cambridge University Press, Cambridge (1989).

[192] R. Mannella and V. Palleschi. Fast and precise algorithm for computer simulation of stochastic differential equations. Phys. Rev. A **40**, 3381 (1989).

[193] R. Mannella. A gentle introduction to the integration of stochastic differential equations. In J. A. Freund and T. Pöschel, editors, *Stochastic Processes in Physics, Chemistry, and Biology*. Springer, Berlin, Heidelberg (2000).

[194] M. H. Devoret. Quantum fluctuations in electrical circuits. In S. Reynaud, E. Giacobino, and F. David, editors, *Quantum Fluctuations, Volume 63 (Les Houches)*. North Holland, Amsterdam (1997).

[195] W. C. Stewart. Current-voltage characteristics of Josephson junctions. Applied Physics Letters **12**, 277 (1968).

[196] D. E. McCumber. Effect of ac impedance on dc voltage-current characteristics of superconductor weak-link junctions. Journal of Applied Physics **39**, 3113 (1968).

[197] G. B. Folland. *Fourier Analysis and its Applications*. American Mathematical Society (1992).

[198] K. F. Graff. *Wave Motion in Elastic Solids*. Dover Publications, Inc. (1975).

[199] N. Lindahl, D. Midtvedt, J. Svensson, O. A. Nerushev, N. Lindvall, A. Isacsson, and E. E. B. Campbell. Determination of the bending rigidity of graphene via electrostatic actuation of buckled membranes. Nano Lett. **12**, 3526 (2012).

[200] M. Aspelmeyer, T. J. Kippenberg, and F. Marquardt. Cavity optomechanics. Rev. Mod. Phys. **86**, 1391 (2014).

[201] D. E. Chang, C. A. Regal, S. B. Papp, D. J. Wilson, J. Ye, O. Painter, H. J. Kimble, and P. Zoller. Cavity opto-mechanics using an optically levitated nanosphere. Proc. Natl. Acad. Sci. U.S.A. **107**, 1005 (2010).

[202] A. Ashkin, J. M. Dziedzic, J. E. Bjorkholm, and S. Chu. Observation of a single-beam gradient force optical trap for dielectric particles. Opt. Lett. **11**, 288 (1986).

[203] T. Li, S. Kheifets, and M. G. Raizen. Millikelvin cooling of an optically trapped microsphere in vacuum. Nat. Phys. **7**, 527 (2011).

[204] O. Romero-Isart, M. L. Juan, R. Quidant, and J. I. Cirac. Toward quantum superposition of living organisms. New J. Phys. **12**, 033015 (2010).

[205] T. S. Monteiro, J. Millen, G. A. T. Pender, F. Marquardt, D. Chang, and P. F. Barker. Dynamics of levitated nanospheres: towards the strong coupling regime. New J. Phys. **15**, 015001 (2013).

[206] O. Romero-Isart. Levitated nanospheres in the quantum regime. Lectures given at École de Physique des Houches Session CV: Quantum Optomechanics and Nanomechanics.

[207] N. J. Rao, J. D. Borwanker, and D. Ramkrishna. Numerical solution of Ito integral equations. SIAM J. Control **12**, 124 (1974).

Populärvetenskaplig sammanfattning

De flesta av oss har vid något tillfälle hört en gitarr stämmas. När stämningsskruven vrids varierar den kraft som gitarrsträngen utsätts för, och strängens ton förändras. Det faktum att vibrationshastigheten – tonen – hos ett svängande material beror på krafter i omgivningen kan utnyttjas för att bygga *sensorer*: konstgjorda "sinnen" som känner av vad som händer i närheten. En vanlig gitarrsträng "mäter" via sin ton den elastiska kraft den utsätts för när den spänns mellan stämskruv och stall.

Nästan alla tekniska prylar vi använder behöver känna av sin omgivning på något vis, och innehåller någon sorts sensorer. De sitter i bilars säkerhetssystem och mäter hastighetsförändringar, de håller koll på vilket håll som är nedåt så att skärmen roteras i mobiltelefoner och surfplattor, och de vet hur många gånger en stegräknare har pendlat fram och tillbaka. Det är nästan så att ju nyare en pryl är, desto fler sensorer innehåller den. Tänk till exempel på VR-headsets som måste veta hur du rör ditt huvud för att kunna visa en korrekt bild, och på alla sätt som en självkörande bil måste hålla koll på vägens sträckning, mötande trafik, och lekande barn. I framtiden kanske vi kommer kunna använda kontaktlinser med inbyggda små skärmar, eller fästa en touchscreen som ett klistermärke på underarmen. Ny teknik ställer nya krav på hur sensorer utformas – de kanske måste ta mindre plats eller vara mycket känsligare än idag.

Hur små krafter en strängliknande sensor kan mäta beror bland annat på hur stor den är. En person med känslig hörsel skulle kanske kunna höra hur en gitarrsträngs ton ändras när en humla landar på den, och från tonförändringen räkna ut hur mycket humlan väger. Däremot kan ingen av oss märka om några dammkorn skulle fastna på strängen; kornen är helt enkelt alldeles för små, jämfört med strängen. En metod för att göra känsligare sensorer är därför att göra dem mindre.

Inom grundforskning försöker forskare svara på frågor bara på grund av nyfikenhet och intresse, och att veta vad praktiskt kan använda ett resultat till är mindre viktigt. En sådan grundforskningsfråga är "hur små saker kan vi mäta?",

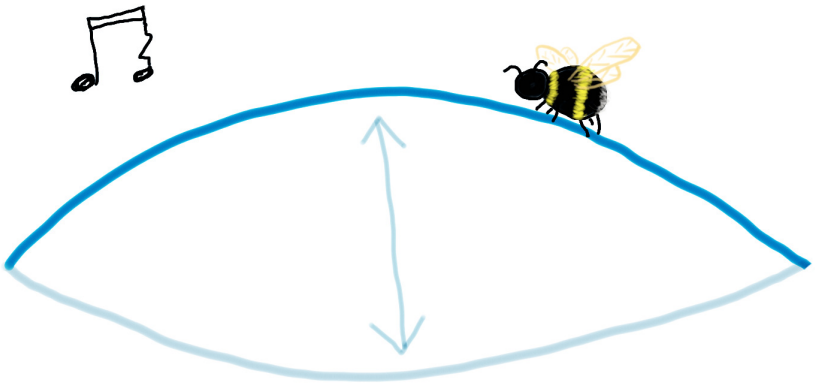

och strävan efter att svara på denna fråga ligger bakom fantastiska framsteg i hur känsliga sensorer vi kan skapa. Forskare har skapat strängar som är så små att hundratals av dem får plats på ett enda hårstrå och som vibrerar en miljon gånger snabbare än en vanlig gitarrsträng. Med hjälp av dessa "nanosträngar" har forskare lyckats mäta nästan ofattbart små saker, till exempel hur mycket (eller kanske hur lite) en enstaka atom väger.

En så känslig sensor kan ha svårt att mäta rätt sak – dammkornen som gitarrsträngen inte alls märker av är enorma jämfört med nanosträngen! För att kunna mäta väldigt små saker måste nanosträngen därför isoleras från alla sorters störningar i väldigt hög grad. Detta uppnås genom att pumpa bort all luft som omger strängen, så att den hamnar i vakuum, samtidigt som man kyler ner den till nära den absoluta nollpunkten. Det är nästan som om man skulle ha skickat ut nanosträngen i rymden. Som du säkert förstår går det dock inte att skapa rymdliknande förhållanden kring en nanosträng som ska sitta i en pryl vi använder i vardagen. För att kunna använda nanosträngs-sensorer i sammanhang utanför laboratorium så måste sensorn fungera trots att den utsätts för störningar.

För att kunna lösa ett problem måste man först förstå hur problemet fungerar. Min forskning handlar om att matematiskt beskriva och undersöka nanosträngar som utsätts för störningar i form av pytteskräp, tungt som ett par hundra atomer, som fastnar på strängen och studsar runt. Jag har upptäckt att det studsande skräpet dramatiskt förändrar på vilket sätt strängen beter sig. I början av strängens vibration fastnar allt skräp i mitten av den, precis som när pärlor på ett snöre dras till mitten av det ifall snöret snurras runt som ett hopprep. Att hålla skräpet fångat på detta sätt kräver dock energi, som tas från nanosträngens vibration. Precis som hur en gitarrsträng tappar energi och gradvis låter tystare och tystare för att till sist stanna av helt, så kommer nanosträngen *ringa ned* på grund av skräpet. Efter

ett tag rör sig inte strängen nog för att hålla skräpet fångat i mitten, utan det rymmer och börjar studsa runt över hela strängen. Den takt i vilken strängen tappar energi på grund av skräpet är väldigt speciell. Dels så är det inte samma takt som energi försvinner från en vanlig sträng, dels så förändras takten när skräpet rymmer.

Att jag har undersökt effekten av skräp på nanosträngar gör att det nu finns ett "facit". Om andra forskare i framtiden ser oväntade saker i sina nanosträngsexperiment så kan de ta en titt i min forskning. Ifall det beteende de ser är samma sorts konstigheter som jag har upptäckt, så vet de att det sannolikt har fastnat skräp på deras nanosträng. På detta sätt bidrar denna avhandling till forskningen i stort. Även om jag främst har sysslat med grundforskning, som sannolikt inte kommer att kunna användas i vardagen de närmaste åren, så kan mitt arbete komma att bli en liten pusselbit i utvecklingen av nya sorters sensorer som sitter i nya, häftiga prylar. Den som lever får se!